Atmospheric Superrotation in Warm Earth Climates

(Article begins on next page)

Atmospheric Superrotation in Warm Earth Climates

A dissertation presented

by

Nathan Patrick Arnold

to

The Department of Earth and Planetary Sciences

in partial fulfillment of the requirements

for the degree of

Doctor of Philosophy

in the subject of

Earth and Planetary Sciences

Harvard University

Cambridge, Massachusetts

October 2013

Dissertation Advisor: Professor Eli Tziperman   Nathan Patrick Arnold

Atmospheric Superrotation in Warm Earth Climates

Abstract

This thesis considers atmospheric superrotation, a state of westerly equatorial winds which must be maintained by up-gradient eddy momentum fluxes. Superrotation has appeared in simulations of warm climates that generate enhanced Madden-Julian Oscillation (MJO)-like variability. This led to hypotheses that the warmer atmospheres of the early Pliocene and Eocene may have been superrotating, and that the phenomenon may be relevant to future climate projections.

To understand the MJO response to increases in temperature, I conduct aquaplanet simulations with a super-parameterized general circulation model. Between $29°C$ and $35°C$, enhanced MJO variability causes a three-fold increase in equatorward eddy momentum fluxes and increasingly westerly equatorial winds. A composite moist static energy (MSE) budget shows that the MJO amplification is due to vertical advection over an MSE profile which steepens with increased SST. This steepening is a direct consequence of maintaining a moist adiabat over a warmer surface and suggests MJO amplification is fundamental to warming.

This effect is then studied in a more realistic configuration using a coupled ocean-atmosphere model with continents and a seasonal cycle. Simulations are run with $1 \times CO_2$ and $4 \times CO_2$, and MJO activity is found to intensify in the warmer climate. Consistent with the aquaplanet results, the MSE budget identifies vertical advection over a steeper MSE profile as the primary cause.

A positive feedback is then proposed, capable of driving abrupt transitions from a conventional circulation to a strongly superrotating one. Shallow water theory is used to show that as a mean westerly wind approaches the phase speed of free equatorial Rossby waves, the amplitude of a Rossby wave forced by fixed eddy heating will undergo a resonant amplification, along with its equatorward momentum flux. Idealized simulations with a numerical model demonstrate that the resonance and abrupt transitions can occur in the fully 3D primitive equations.

Finally, I consider an explanation for large warm anomalies at mid-latitude coastal upwelling sites during the Pliocene. Simulations run with two reconstructions of Pliocene SST show reductions in upwelling-favorable winds around all four mid-latitude sites, suggesting that the coastal anomalies could result from reductions in upwelling forced by the large-scale SST pattern.

Contents

Author List

The following authors contributed to Chapter 1: Eli Tziperman.

The following authors contributed to Chapter 2: Zhiming Kuang, Eli Tziperman.

The following authors contributed to Chapter 3: Mark Branson, Zhiming Kuang, David Randall, Eli Tziperman.

The following authors contributed to Chapter 4: Eli Tziperman, Brian Farrell.

The following authors contributed to Chapter 5: Eli Tziperman.

The following authors contributed to Chapter 6: Eli Tziperman.

Listing of figures

THIS WORK IS DEDICATED TO MY PARENTS.

Acknowledgments

Why are things as they are and not otherwise?

Johannes Kepler

1

Introduction

1.1 Preliminaries

THE GENERAL CIRCULATION OF THE ATMOSPHERE encompasses the large-scale overturning of the Hadley cell, the rapid eastward flow of the mid-latitude jets, and the synoptic-scale eddies which influence them. Although in principle the governing equations are known, the system is nonlinear and intimately bound to radiative and moist processes operating on much smaller scales. We have no comprehensible theory for the system as a whole; our analytical solutions are piecewise, describing the Hadley circulation, or the jets, in isolation. To understand

the interaction of these subsystems we may turn to numerical models, but these necessarily involve approximations and often give conflicting results (e.g., Stevens and Bony, 2013). There is thus no way to conclusively assess the stable states of the atmosphere, as one might for a simpler system.

This situation leaves open many basic questions, and fascinating possibilities. Is the observed circulation stable to large perturbations? Can small changes in boundary conditions or forcing lead to qualitatively different regimes? Lorenz (1968) speculated that climate variability in the past could be explained by an intransitive atmosphere, capable of shifting between regimes which are otherwise stable for finite time.

More specifically, Held (1999a) and Pierrehumbert (2000) have raised the possibility of atmospheric superrotation. Superrotation refers to a persistent state of zonal-mean westerly winds, with angular momentum greater than that of a planet's equatorial surface. Many planetary and lunar atmospheres in our solar system are superrotating, including Venus, Jupiter, Saturn and Titan. This contrasts with the present-day Earth, where equatorial winds are primarily easterly, and strong westerlies are largely confined to the mid-latitude jets. Earth's atmosphere does superrotate, but only in the stratosphere during the westerly phase of the quasi-biennial oscillation (QBO).

This thesis considers the possibility of persistent superrotation in Earth's troposphere. One may imagine that in other periods of Earth's history, operating under different boundary conditions, the atmosphere may have organized itself quite differently from present, potentially in a superrotating state.

Even if Earth's atmosphere has never hosted a strongly superrotating jet such as that seen on Jupiter, the same dynamics which would maintain such a jet could serve in lesser amounts to simply weaken the equatorial easterlies. This scenario has been proposed as an explanation for the "permanent El Niño" of the Pliocene warm period, 2-5Ma (Tziperman and Farrell, 2009). Figure 1.1.1 shows proxies for sea surface temperature (SST) which indicate that the area of the modern
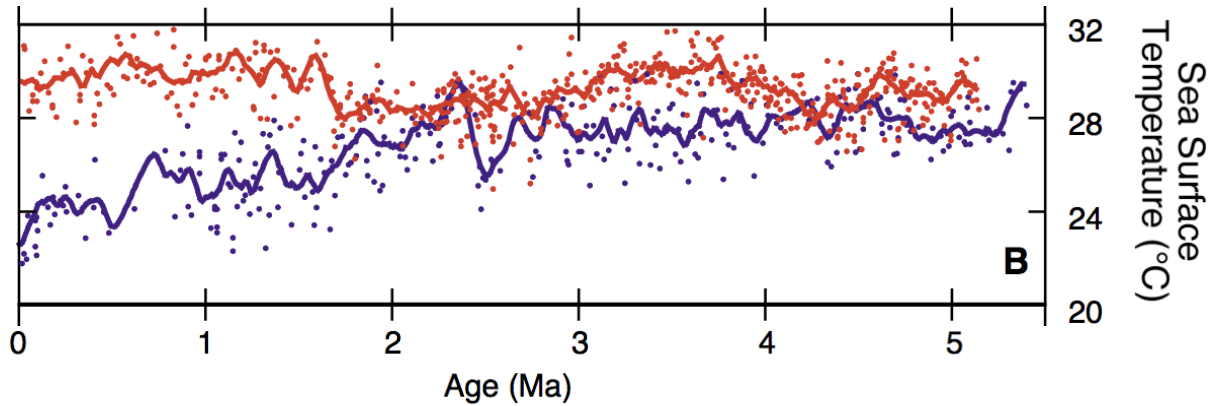
Figure 1.1.1: Sea surface temperatures in the west (red) and east (blue) equatorial Pacific, derived from Mg/Ca data, showing a gradual increase in the east-west gradient over the last 3My. From Wara et al. (2005).

equatorial cold tongue was significantly warmer in the Pliocene, with the east-west SST gradient nearly eliminated, similar to an El Niño event (Ravelo et al., 2006, Wara et al., 2005). The modern cold tongue is maintained by the upwelling of cold deep water, forced by easterly surface winds. A state approaching superrotation would imply weaker easterlies, reduced upwelling and a disappearance of the cold tongue, thereby explaining the Pliocene data.

Superrotation has also been seen in numerical simulations of the Eocene, a particularly warm period from 34-54Ma (Caballero and Huber, 2010). The superrotation in these simulations increased steadily with planetary temperature and was attributed to the emergence of a very strong tropical wave resembling the observed Madden-Julian Oscillation (MJO). The onset of superrotation was also associated with a reduction in the Hadley circulation. In turn, the weakened subtropical subsidence reduced the prevalence of low clouds and enhanced shortwave absorption at the surface, which sharply increased the simulated climate sensitivity (Caballero and Huber, 2013).

Finally, it has been suggested that superrotation could develop in the future as a result of global warming (Held, 1999a, Pierrehumbert, 2000). Atmospheric CO_2 concentrations over the next few centuries are likely to reach levels somewhere between those of the Pliocene (400ppm; Seki

et al., 2010) and the Eocene (1000-4000ppm; Pagani et al., 2005, Pearson and Palmer, 2000), with comparable warming (Meehl et al., 2007). Suggestions of superrotation in past warm periods therefore seem relevant to our own future.

The remainder of this chapter will introduce the fluid dynamics of superrotation, and present a summary of the observed tropical zonal momentum budget.

1.2 THE DYNAMICS OF SUPERROTATION

If the equatorial surface has angular momentum per unit mass $M_0 = \Omega a^2$, with Ω the angular velocity of planetary rotation and a the planet's radius, then the zonal angular momentum per unit mass of an air parcel at latitude ϕ is given by $M(\phi) = M_0 \cos^2 \phi + u_r a \cos \phi$, where u_r is the zonal velocity relative to the local surface, and we ignore the small effect of deviations from the planet's average radius. A superrotating state requires $M(\phi) > M_0$ averaged over a latitude band, or

$$\overline{u}_r(\phi) > \frac{\Omega a \sin^2 \phi}{\cos \phi}.$$

This condition is obviously easiest to satisfy at the equator, where any zonal-mean westerly wind qualifies.

The novelty of superrotation may be better appreciated by naively imagining that atmospheric eddy motions — deviations from the zonal-mean flow — tend to mix fluid properties at random, with a combined effect that may be modelled as diffusion. This diffusive approximation is actually quite reasonable for many scalar properties, e.g. heat (Held, 1999b), producing a net flux from high to low concentration. However, Hide (1969) showed that in an atmosphere where eddy momentum transport is diffusive, superrotation becomes impossible. This result has become known as Hide's Theorem, which states that a diffusive two-dimensional (latitude and height) atmosphere - that is, an atmosphere with a zonal-mean circulation and eddy processes that combine to produce diffusion - cannot support a maximum of angular momentum over the

equator. This is briefly demonstrated as follows.

The zonal-mean angular momentum is governed by

$$\rho \partial_t M + \rho \boldsymbol{u} \cdot \nabla M = \nabla \cdot (\nu \rho \nabla M)$$

which may be re-written

$$\partial_t(\rho M) = -\nabla \cdot (F_{adv} + F_{fric}).$$

Suppose that an extremum of angular momentum exists away the surface, enclosed by a contour C denoting $\bar{u} = 0$, such that the zonal wind within the contour is westerly. Integrating the steady state continuity equation over the extremum yields

$$\iint_A \nabla \cdot \rho \boldsymbol{u} dA = \oint_C \rho \boldsymbol{u} \cdot \hat{n} dl = 0.$$

Meanwhile, the net advective flux of M across C is given by

$$\oint_C \boldsymbol{F}_{adv} \cdot \hat{n} dl = \tilde{M} \oint_C \rho \boldsymbol{u} \cdot \hat{n} dl = 0$$

where $\tilde{M}$ is the (constant) angular momentum on C. Due to mass conservation, the net mass flux across the contour must cancel, which implies that the net advective flux across the contour is exactly zero; the zonal-mean circulation has no effect on the extremum. However, the diffusive frictional flux is given by

$$\oint_C \boldsymbol{F}_{fric} \cdot \hat{n} dl = -\oint_C \rho \nu \hat{n} \cdot \nabla M dl > 0,$$

which would tend to reduce the extremum. This indicates that, for a two-dimensional circulation, *any* down-gradient diffusion will prohibit extrema in M away from the surface.

If all atmospheric eddy processes acted diffusively on zonal momentum then superrotation

would be impossible and there would be little else to say on the subject. Fortunately for this thesis, many eddy motions are organized so as to provide up-gradient momentum transport. Meridional transport of angular momentum in Earth's atmosphere is primarily accomplished by Rossby waves with an equivalent barotropic vertical structure. Key properties of these waves are derived below, following Hoskins and Karoly (1981).

The external mode Rossby waves are governed by the nondivergent barotropic vorticity equation linearized about a zonal mean flow $\bar{u}$

$$\left(\partial_t + \overline{u}\partial_x\right)\nabla^2\psi' + \beta_M\partial_x\psi' = S + F$$

where $\nabla^2 = \partial_x^2 + \partial_y^2$, ψ' is the perturbation streamfunction, S' is the Rossby wave "source" and F' represents frictional damping. We have used the Mercator projection with $x = a\lambda$, $y = a\log[(1 + \sin\phi)/\cos\phi]$, and β_M represents the gradient in absolute vorticity on a sphere, scaled by $\cos\phi$. For now we consider free waves with $S' = F' = 0$, and return to the source term in greater detail below.

Substituting a wave-like solution of the form $\psi' = Re(\tilde{\psi}e^{i(kx+ly-\omega t)})$, we arrive at the dispersion relation

$$\omega = \bar{u}k - \frac{\beta_M k}{k^2 + l^2},$$

from which we may derive a meridional group velocity

$$c_g^y = \frac{\partial \omega}{\partial l} = \frac{2\beta_M kl}{(k^2 + l^2)^2}.$$

The meridional flux of zonal momentum accomplished by these waves, $u'v' = -\partial_x\psi'\partial_y\psi' = -kl\tilde{\psi}^2$, is thus directed opposite to their group velocity. This demonstrates two important points. First, that Rossby wave momentum transport is not constrained to be down-gradient, implying that superrotation is possible without violating Hide's

theorem. Second, the direction of momentum transport implies that Rossby waves accelerate the latitude at which they are excited, and decelerate latitudes where they break or dissipate. Rossby wave-driven superrotation thus requires a wave source on the equator.

Let us examine in more detail the problem of exciting Rossby waves over the equator. Returning to the barotropic vorticity equation

$$\left(\partial_t + \overline{u}\partial_x\right)\nabla^2\psi + \beta_M\partial_x\psi = S + F,$$

we consider the Rossby wave source defined by Sardeshmukh and Hoskins (1988):

$$S' = -\nabla \cdot (\boldsymbol{v_X}'\overline{\zeta}) - \nabla \cdot (\overline{\boldsymbol{v_X}}\zeta')$$

where v_X is the divergent component of horizontal velocity, and ζ is the absolute vorticity. This formulation suggests two sources of Rossby wave activity: advection of the mean vorticity by anomalous divergence, and a second source due to mean advection of the anomalous vorticity.

Anomalous divergence is generally associated with heating delivered by deep convection organized on a large scale, either by gradients in surface temperature (as over the Pacific Warm Pool) or spontaneously by somewhat mysterious processes (as in the MJO). Superrotation will reliably develop in numerical models with sufficiently strong prescribed equatorial heating (e.g., Kraucunas and Hartmann, 2005, Showman and Polvani, 2010), or in cases with strong MJO activity (e.g., Caballero and Huber, 2010, Grabowski, 2004, Lee, 1999). The effectiveness of a given heating J' is seen in the steady thermodynamic equation with the weak-temperature gradient approximation ($\nabla_H T \approx 0$),

$$\omega'\sigma \approx -\frac{J'}{c_p}$$

where $\sigma = -\frac{T}{\theta}\frac{\partial\theta}{\partial p}$ is the dry static stability. If we take the vertical derivative and substitute from

the continuity equation, we find deviations from the spatial-mean will follow

$$\nabla \cdot \boldsymbol{v_H}' \approx -\frac{\partial}{\partial p}\left(\frac{J'}{\sigma c_p}\right).$$

The upper-level divergence is thus proportional to the anomalous heating J', and inversely proportional to the static stability.

The vertical structure of J' can also be important. In general, the dynamical response to tropical heating can be broken into two components (Salby and Garcia, 1987). The first is the external or barotropic mode, with a vertical wavelength greater than the depth of the heating. The barotropic mode is trapped within the troposphere, but in conditions of suitable shear can propagate meridionally and escape the tropics. Propagating out of the tropics, the barotropic waves flux momentum into the tropics following the Rossby wave dynamics outlined above.

The second component has a baroclinic structure, with vertical wavelength equal to or less than the depth of the heating. The dynamics of this component are described by the equatorial beta-plane solutions of Matsuno (1966) and Gill (1980). This mode can propagate upward into the stratosphere but is meridionally trapped within the tropics, and is thus limited to transporting momentum from the subtropics. Each component of the wave response can contribute to meridional momentum convergence, and both have been cited in studies of superrotation.

To summarize, most meridional momentum transport is accomplished by equivalent barotropic Rossby waves, which can propagate globally and transport momentum opposite their group velocity. Momentum convergence and westerly acceleration over the equator therefore requires an equatorial Rossby wave source, which is usually provided by organized moist convection. Organized convection also excites a baroclinic response which is equatorially trapped, but can still play an important role by transporting momentum from the subtropics into the deep tropics.
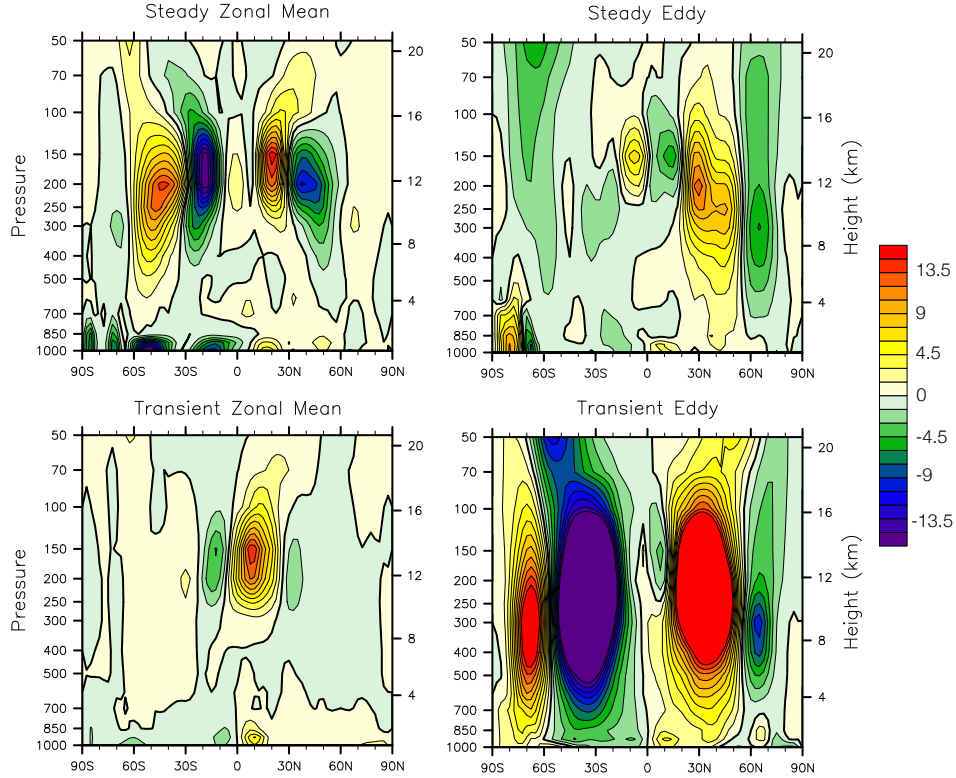
Figure 1.2.1: Zonal-mean meridional fluxes of zonal momentum, broken into eddy and mean components. Positive values indicate northward fluxes of westerly momentum. Derived from NCEP Reanalysis (2000-2009).

1.3 THE OBSERVED TROPICAL MOMENTUM BUDGET

Before considering potential changes in the equatorial winds, it is useful to examine the observed meridional momentum fluxes, which can highlight important processes. We will follow the methodology of Lee (1999), using NCEP Reanalysis for the period 2000-2008 (Kalnay and Coauthors, 1996). The total time- and zonal-mean flux of zonal momentum may be decomposed into eddy and mean components,

$$[\overline{uv}] = [\bar{u}][\bar{v}] + [\bar{u}^*\bar{v}^*] + [\overline{u'^*v'^*}] + \overline{[u]'[v]'}$$

9

where brackets and overbars represent averages of space and time respectively, and asterisks and primes represent the corresponding anomalies. Thus, meridional fluxes by transient eddies are contained in $\overline{[u'^*v'^*]}$, stationary eddies in $[\bar{u}^*\bar{v}^*]$, the fixed zonal-mean circulation in $[\bar{u}][\bar{v}]$, and the transient zonal-mean circulation $\overline{[u]'[v]'}$.

The zonal-mean of each term is shown in Fig. 1.2.1, from which we may draw several important conclusions:

- Stationary eddies provide most of the meridional momentum convergence in the deep tropics. The largest part of this is due to the standing wave pattern forced by convection over the West Pacific Warm Pool.

- The acceleration from stationary eddies is largely balanced by deceleration from the transient zonal-mean circulation: the cross-equatorial flow of the winter hemisphere Hadley cell.

- Equatorial transient eddies also provide momentum convergence in the deep tropics, but their net effect is smaller than the stationary component.

- Mid-latitude transient eddies are the 800lb gorilla of the momentum budget, but their influence is small within the deep tropics due to wave-breaking in the subtropics (see Fig. 1.3.2). This occurs at critical lines where the wave phase speed is equal to the background zonal wind, causing $c_g^y \to 0$ and a pile-up of wave energy.

The transient eddy momentum flux is driven by several different wave sources, operating on distinct time and spatial scales. Fig. 1.3.2 shows a momentum flux co-spectrum, teasing apart distinct sources by separating fluxes by zonal wavenumber and frequency. Strong poleward fluxes in the subtropics are associated with mid-latitude waves propagating equatorward, while
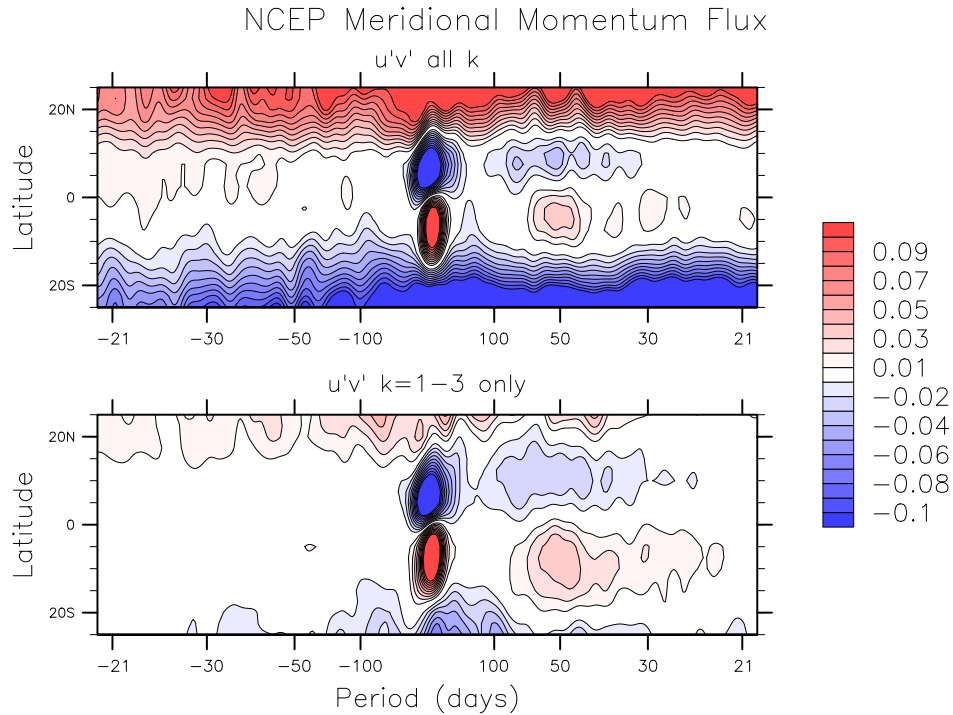
Figure 1.3.1: The co-spectrum of 200hPa transient eddy momentum fluxes, integrated over all zonal wavenumbers (top) and over wavenumbers 1-3 (bottom). Poleward fluxes due to subtropical wave breaking are visible over all frequencies at higher wavenumbers, while low wavenumbers are dominated by interannual (ENSO) and intraseasonal (MJO) variability.

equatorward momentum fluxes in the deep tropics are due to ENSO and the MJO, operating at low wavenumbers, and interannual and intraseasonal timescales, respectively.

This overview suggests a variety of ways to shift the atmosphere toward superrotation:

- Increase the tropical stationary wave source. This could be accomplished by increasing zonal asymmetries within the tropics, e.g. by increasing the SST gradient across the Pacific to further concentrate convection over the warm pool, or by shifting continents to similarly concentrate convection.

- Increase the tropical transient wave source, most likely by increasing MJO activity.

- Weaken the transient Hadley circulation. This might be accomplished by reducing the
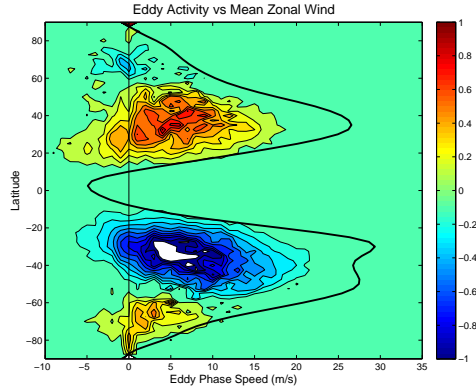
Figure 1.3.2: The 200hPa eddy momentum flux cospectrum mapped onto eddy phase speed ω/k (contours), and 200hPa zonal-mean zonal wind (solid line). The coincidence of the contour edge and zonal wind suggests wave-breaking at critical lines where the wave phase speeds equal the background zonal wind.

relative amplitude or poleward extent of the summer SST maximum. Superrotation reliably develops in numerical simulations where the specified SST is hemispherically symmetric.

- Decrease mid-latitude wave activity. There are many factors which could affect the magnitude or position of the eddy-driven jets, including pole-to-equator temperature gradients and continental topography.

This thesis will examine only one of these factors in detail: an increase in momentum convergence driven by enhanced MJO activity. This has been the most common cause of superrotation in models, but the underlying physics has been poorly understood. A mechanism for MJO intensification with warming is identified in Chapter 2, using an aquaplanet model with exceptional MJO simulation skill. This mechanism is studied in a more realistic model configuration in Chapter 3. In Chapter 4 we propose a positive feedback which can produce abrupt transitions to strong superrotation. Chapter 5 considers the possibility of superrotation in a specific period of Earth history: the Pliocene. Our conclusions are laid out in Chapter 6.

2

Enhanced MJO-like Variability at High SST in the Aquaplanet SP-CAM

2.1 INTRODUCTION

ORGANIZED CONVECTION PLAYS AN IMPORTANT ROLE as a tropical wave source, and understanding its dependence on the background climate is a central part of the superrotation problem. Surface temperatures in the tropical belt have varied significantly over geologic time

(e.g., Dowsett and Robinson, 2009a, Pearson et al., 2007), and are projected to increase by 2-3°C over the 21st century (Meehl et al., 2007). Considerable work has been done establishing global constraints on the precipitation response to warming (e.g., Held and Soden, 2006), and quantifying changes in extreme events (e.g., Muller et al., 2011). However, with the notable exception of tropical cyclones, less attention has been paid to the response of organized convective variability, and in particular the wave-like modes seen in equatorial spectra.

Here we study the dependence of organized tropical convection on mean sea surface temperature (SST) in an aquaplanet general circulation model (GCM) which generates an intraseasonal disturbance strongly resembling the observed Madden-Julian Oscillation (MJO). First identified by Madden and Julian (1971), the MJO may be regarded as a multiscale structure, with a broad (10,000km) envelope of enhanced deep convection coupled to neighboring regions of suppressed convection through a large-scale overturning circulation. The convectively active phase typically originates over the Indian or West Pacific ocean and propagates eastward at roughly 5m/s before dissipating over the cooler waters of the East Pacific. A convectively uncoupled signal in surface pressure and zonal wind may continue eastward at higher speed. This basic description omits seasonality, meridional propagation, and other details; we refer the reader to Zhang (2005) for a more complete review.

Observational evidence for a dependence of intraseasonal variability (ISV) on SST is limited, and complicated by spatially inhomogeneous patterns of warming and cooling. Changes in the Tropical SST distribution can alter the large-scale circulation and result in dynamic forcing of convection, regardless of mean SST. Nevertheless, weak positive trends in ISV are seen in NCEP-NCAR Reanalysis (Jones and Carvalho, 2006) and the 20th Century Reanalysis (Oliver and Thompson, 2012) over the last four decades, during which time Tropical SSTs have increased by roughly 0.5°C. Similarly, interannual variability in MJO activity shows a weak correlation with SST over the Indian and West Pacific oceans (Hendon et al., 1999). It is clear that processes other than local SST dominate MJO variability at the interannual timescale, but this should not be

surprising given that interannual SST anomalies in these regions are typically $0.5°$C or less. It is unclear what effect a more substantial and sustained change in mean SST would have on ISV.

The quest for a complete theoretical description of the MJO is ongoing, despite improved observational constraints (e.g., Benedict and Randall, 2007, Grodsky et al., 2009, Kiladis et al., 2005, Kiranmayi and Maloney, 2011), guidance from numerical models (e.g., Benedict and Randall, 2009, Kim et al., 2011, Maloney, 2009), and recent theoretical developments (e.g., Fuchs and Raymond, 2002, Kuang, 2011, Raymond and Fuchs, 2009). There are currently a number of viable approaches, not all mutually exclusive. Some emphasize the role of scale interaction (e.g., Majda and Biello, 2004, Majda and Stechmann, 2009), while others focus on small-scale physical processes and thermodynamic feedbacks (e.g., Raymond, 2001, Sobel et al., 2008a). Many of the prevailing ideas are summarized and evaluated by Sobel and Maloney (2012).

The importance of environmental humidity was recognized early on. Entrainment of environmental air into a convecting plume results in evaporative cooling and loss of buoyancy, such that the vigor of deep convective activity is tied directly to the environmental relative humidity; deep convection is suppressed in dry environments, and encouraged in moist ones. Blade and Hartmann (1993) proposed a "discharge-recharge" hypothesis in which the timescale of the MJO is set by the build-up (recharge) of column moisture by shallow, non-precipitating convection, which pre-conditions the atmosphere for strong deep convection. Deep convection results in moisture discharge and drying of the column, and a return to the "recharge" phase of the oscillation.

We interpret our results within the "moisture mode" paradigm, which has appeared under various guises in previous work (e.g., Fuchs and Raymond, 2002, Raymond and Fuchs, 2009, Sobel et al., 2001). In this context, the MJO is viewed as an essentially linear instability resulting from the covariation of column moist static energy anomalies with sources or sinks thereof. In other words, a moisture mode instability will occur when the effective gross moist stability (Neelin and Held, 1987, Raymond, David J. and Sessions, Sharon L. and Sobel, Adam H. and

Fuchs, Zeljka, 2009), including sources and sinks of MSE due to surface fluxes and radiative heating, is negative.

A moisture mode is distinct from the classical spectrum of shallow water waves, whose underlying dynamics may operate in a dry atmosphere and are merely modulated by interaction with moist convection, rather than fundamentally dependent on it (Kiladis et al., 2009). The classification of the MJO as a moisture mode is suggested by wavenumber-frequency spectra of MSE, which typically retain an MJO signal but show reduced power around the shallow water wave dispersion curves (e.g., Andersen and Kuang, 2012, Roundy and Frank, 2004). However, a fundamental distinction between the MJO and other convectively coupled waves is not universally accepted (Roundy, 2012). Some also argue that nonlinearities may be important to MJO dynamics (Sobel and Maloney, 2012).

Simulation of the MJO in GCMs has been notoriously poor, with few exceptions (Lin et al., 2006), and recent work suggests that an insensitivity of parameterized convection to environmental humidity is a major contributing factor (Thayer-Calder and Randall, 2009). Despite this lack of model realism, we note two studies which found a dependence of ISV on SST in comprehensive GCMs: Lee (1999) reported increased ISV after a uniform 2°C SST perturbation in a GFDL AGCM, and Caballero and Huber (2010) found an increase in ISV in several configurations of NCAR's Community Atmosphere Model (CAM3.1) over a wide range of SST. These studies did not identify a mechanism for the increased variability.

Here we have elected to use a super-parameterized (SP) version of the NCAR Community Atmosphere Model (CAM3.5), run in a zonally symmetric aquaplanet configuration. The decision to use SP-CAM was based on two factors. First, the track record of SP-CAM in simulating a realistic MJO is better than most other GCMs to date (Kim et al., 2009). Second, because super-parameterization is a fundamentally different method of representing convection, it offers an independent test of the model results noted above, which relied on conventional convection parameterizations.

There is a long history of numerical studies of the MJO which treat the earth as an aquaplanet (e.g., Grabowski, 2003, Hayashi and Sumi, 1986, Lee et al., 2003, Maloney et al., 2010, Numaguti and Hayashi, 1991, Swinbank et al., 1988). This approach has the advantage of simplifying the analysis and highlighting any changes in dynamics. On the other hand, it immediately sacrifices certain features like seasonality and the influence of topography, which may be relevant to some studies (e.g., Wu and Hsu, 2009). More subtle aspects of the MJO may also be affected. For example, Lin et al. (2005) note that the mean winds in a zonally symmetric basic state may result in biases by altering the phasing of temperature and heating anomalies, thereby reducing the efficiency of eddy available potential energy generation. Similarly, the presence of mean surface westerlies over the Indian ocean is thought to be important in controlling the phasing of surface fluxes during MJO events (e.g., Maloney et al., 2010), and the easterly surface winds in a zonally symmetric state may affect MJO growth and propagation. Nevertheless, the ability of many numerical models to simulate MJO-like disturbances both with and without zonal asymmetries and topography suggests that the phenomenon may be profitably studied with an idealized setup.

In this study, we present a set of simulations forced with globally uniform increases in SST, in which SP-CAM produces a monotonic and significant increase in MJO-like variability, documented in Section 2.3. In Section 2.4, we present a composite MSE budget of the model MJO, and attempt to provide an explanation for the increase in variability. Due to the lack of a general theory for the MJO, this attempt is necessarily incomplete, but we believe it provides a compelling direction for future work. Section 2.5 contains a general discussion of these findings, and we summarize our conclusions in Section 2.6.

2.2 Model description and experimental setup

2.2.1 Model Description

In a super-parameterized GCM, the conventional boundary layer and convection parameterizations are replaced with a two-dimensional cloud system resolving model (CSRM) embedded within each GCM grid cell (Grabowski, 2001, Randall et al., 2003). Thus, grid-scale cloud statistics and thermodynamic tendencies are generated through explicit simulation, with the exception of the cloud microphysics, which remain parameterized. A brief history of the super-parameterization technique is provided by Khairoutdinov et al. (2005). A super-parameterized scheme was implemented in the National Center for Atmospheric Research (NCAR) Community Atmosphere Model (CAM) by Khairoutdinov and Randall (2001). The host GCM for the present study is CAM version 3.5, using a semi-lagrangian dynamical core with $2.8°$ x $2.8°$ horizontal resolution, 30 vertical levels, and a timestep of 15 minutes. The CSRM is based on the three dimensional System for Atmospheric Modeling (SAM), described in detail by Khairoutdinov and Randall (2003). In this study, each CSRM domain is an East-West strip of 32 columns with 4km horizontal resolution, a 20 second timestep, and a vertical grid matching the lower 28 levels of the GCM. The boundary conditions are periodic, which precludes any movement of cloud systems between GCM grid cells; convective propagation can occur only through its influence on large scales.

The CSRM influences the GCM grid-scale fields through addition of the CSRM domain-averaged moisture and temperature tendencies, while the CSRM is relaxed toward the GCM fields to prevent drift from the large-scale climate. The 2D CSRM domain does not allow realistic transport of both components of horizontal momentum by convection (i.e., "cumulus friction"), so momentum tendencies are not returned to the GCM.

The super-parameterization results in a number of improvements over the conventional model,

including a realistic diurnal cycle of precipitation and less tendency to "drizzle" (Khairoutdinov et al., 2005). Most significant for this study, SP-CAM simulates much stronger intraseasonal variability (ISV) than the conventional CAM. The stronger ISV in SP-CAM has been attributed to a greater sensitivity of precipitation to the total column moisture; at higher relative humidities, convective entrainment of environmental air results in less evaporative cooling, greater net convective heating, and a stronger large-scale circulation (Thayer-Calder and Randall, 2009). If anything, SP-CAM produces a column that is overly moist, and generates ISV somewhat stronger than observed. The MJO in SP-CAM has a generally realistic temporal evolution, with pre-conditioning of the middle troposphere by anomalous meridional convergence of moisture, and a rapid moisture discharge following deep convection (Benedict and Randall, 2009).

Previous super-parameterization studies have shown some sensitivity to the details of the CSRM configuration. For example, use of a 3D CSRM domain and the addition of momentum coupling were shown to reduce a bias in mean precipitation over the west Pacific warm pool (Khairoutdinov et al., 2005). To test the sensitivity of the results presented here, we run a pair of two-year simulations with equatorial SST of $35°$C. In the first, we increase the CSRM resolution from 4km to 1km and change the orientation from East-West to North-South. In the second, we use a 3D domain of 32km by 32km with 4km grid spacing (and no momentum coupling). Statistics from the last 21 months of each simulation are compared with the $35°$C case discussed below. We find no significant differences in either the mean state or intraseasonal variability, and conclude that our basic results are relatively insensitive to the CSRM geometry and resolution. Khairoutdinov and Randall (2003) also report some sensitivity to microphysics parameters, but these are not examined here.

2.2.2 Experimental Setup and Mean State

We use an aquaplanet configuration in which SP-CAM was previously shown to generate MJO-like variability, and the base state MJO (with $T_0 = 29°$C) was thoroughly characterized by
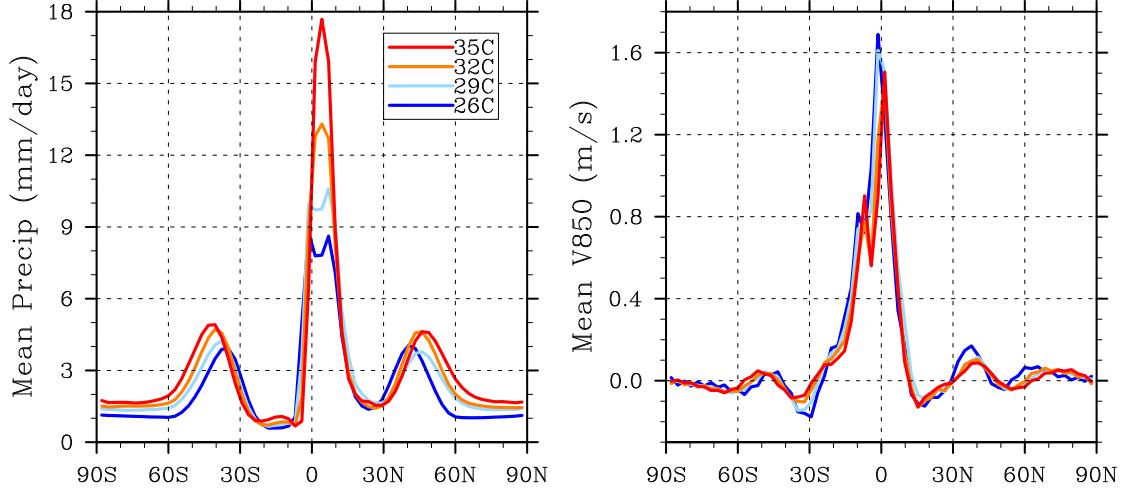
Figure 2.2.1: Time- and zonal-mean 850hPa meridional wind (a) and precipitation (b).

Andersen and Kuang (2012). The prescribed sea surface temperatures are given as a function of latitude ϕ by

$$T(\phi) = T_0 - \Delta T(\zeta + \zeta^2)$$

where

$$\zeta = \begin{cases} \sin^2(\pi \frac{\phi-5}{110}) & 5 < \phi \leq 60 \\ \sin^2(\pi \frac{\phi-5}{130}) & -60 \leq \phi \leq 5 \\ 1 & |\phi| > 60 \end{cases}$$

such that the peak SST is offset from the equator to 5°N and ΔT is fixed at 13.5°C. Insolation is set to a perpetual equinox, though the diurnal cycle is retained.

The prescribed SST pattern results in a mean state reminiscent of boreal summer over the central Pacific, although the lack of zonal asymmetry precludes a Walker circulation. The meridional circulation is dominated by a southern hemisphere Hadley cell, with strong low level convergence and precipitation centered on the SST maximum (Fig. 2.2.1). Midlatitude eddy activity is comparable to observations.

To study the dependence of MJO activity on mean SST, we run a set of simulations in which T_0 is varied from 26°C to 35°C, in increments of 3°C, with a fixed meridional gradient. Our focus here is not on the mean state, but we note that the mean lower tropospheric mass convergence remains roughly constant, as suggested by the zonal mean 850hPa meridional velocity (Fig. 2.2.1a), while precipitation along the model's "ITCZ" increases significantly (Fig. 2.2.1b). Importantly, but not surprisingly, the relative humidity field remains roughly constant (not shown).

A uniform surface warming is an obviously imperfect representation of the response to greenhouse gas forcing or the anomalies of past warm climates, which can vary spatially and result in large-scale circulation changes, in turn forcing dynamic changes in convection (Bony et al., 2004). Like the idealized aquaplanet geometry, a uniform warming is meant to capture the first order thermodynamic response and allow us to identify simple physical principles. More realistic simulations, including continents, a seasonal cycle, and a spatially-varying warming, are examined in Chapter 3.

2.3   Intraseasonal variability increases with SST

Hovmöller plots of outgoing longwave radiation (OLR) along the equator are shown in Fig. 2.3.1 for each simulation. As SST is increased, high clouds become increasingly organized into eastward propagating bands. The organized variability also transitions from an essentially episodic phenomenon to one with a semi-regular period of about 25 days, where events tend to circumnavigate the globe two or three times before dissipating, followed by rapid organization of a subsequent event. Hovmöller plots of other variables associated with organized convection (precipitation, column moisture, zonal wind) show a similarly striking dependence on SST.

Wavenumber-frequency power spectra offer quantitative support for these changes. These are calculated as in Wheeler and Kiladis (1999), using OLR averaged between 5°S and 5°N, with the
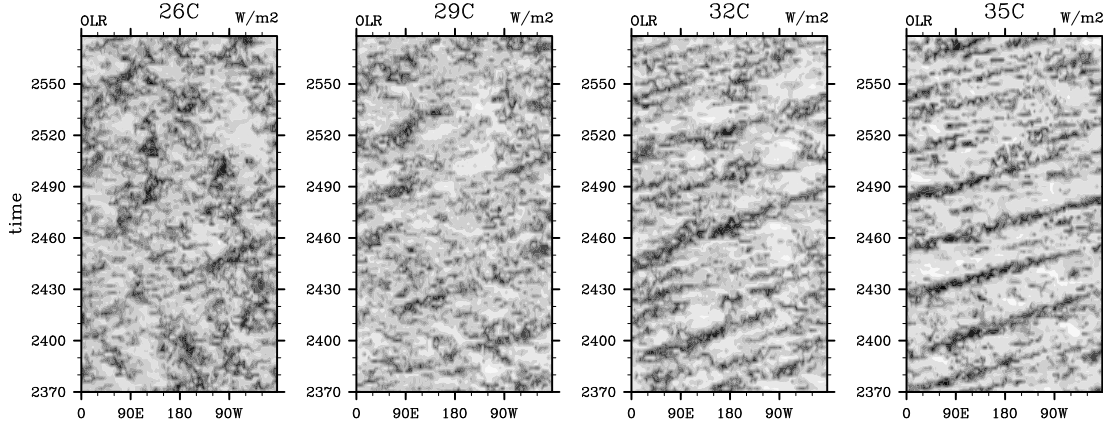
Figure 2.3.1: Hovmöller plots of equatorial OLR from year six of each simulation. A significant increase in cloud organization is visible moving from low (left) to high (right) SST.

exception that we do not divide by a smoothed background spectrum and do not take the logarithm of the power. For the 26°C SST case (Fig. 2.3.2a), an MJO-like signal is seen around zonal wavenumber two and a period of 40 days. The model also produces enhanced energy around the Kelvin and Rossby wave bands predicted by linear shallow water theory (e.g., Matsuno, 1966) and modified through coupling with moist convection (e.g., Kuang, 2008, Mapes, 2000), with phase speeds and peak space-time scales generally consistent with observed OLR spectra (Wheeler and Kiladis, 1999).

The difference in the 35°C case (Fig. 2.3.2b) is dramatic. While the total OLR variance remains roughly constant, the intraseasonal variance contained in wavenumbers 1-3 and periods of 20-100 days more than triples, and the ratio of eastward to westward variance rises from 1.95 to 6.27. There is a somewhat smaller increase in variance along the Kelvin wave band, as well as an increase in phase speed, from roughly 12m/s at 26°C to 19m/s at 35°C. We also see a steady increase in the MJO frequency, such that in the 35°C case (Fig. 2.3.2b) the "MJO" signal is overlapping with the Kelvin wave band, though it is still visible as a distinct peak. The movement of the peak in spectral space is continuous across the four simulations, which reassures us that it
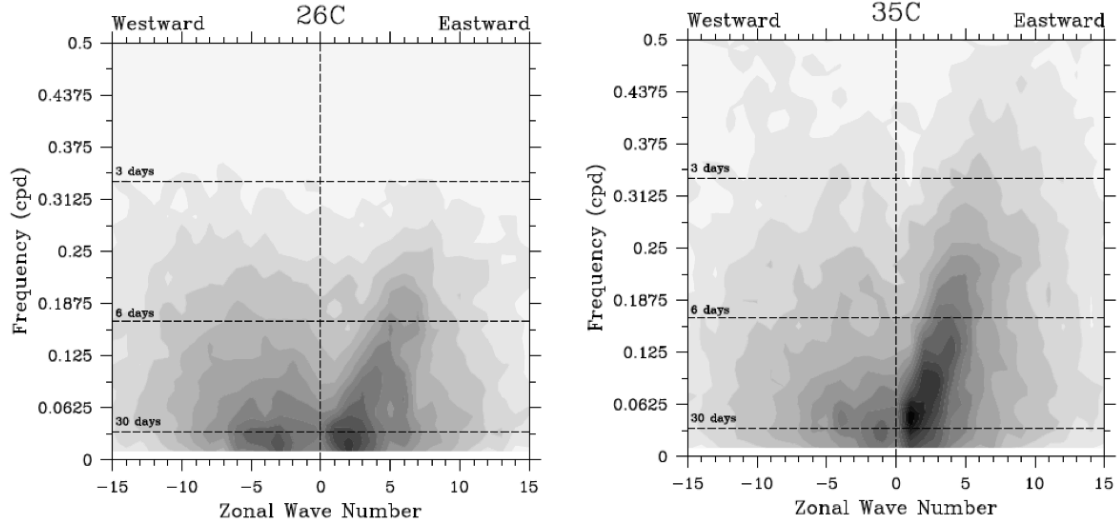
Figure 2.3.2: Wavenumber-frequency power spectra of OLR for the 26°C (left) and 35°C (right) simulations. Contour intervals are $1W^2/m^4$, and the $9W^2/m^4$ contour is bold in both panels.

corresponds to the same underlying phenomenon. Though the increase in both Kelvin wave and MJO variance is intriguing given their different dynamical bases, for now we focus on the MJO-like disturbance, which shows the greatest change in variance.

2.4   MOMENTUM CONVERGENCE AND SUPERROTATION

Increases in intraseasonal variability have led to superrotation in previous studies (Arnold et al., 2012, Caballero and Huber, 2010, Lee, 1999), and we observe a similar trend toward equatorial westerlies as the SST is increased (Fig. 2.4.1). Superrotation remains weak (< 10m/s) in these simulations due to the strong easterly torque provided by the perpetual "winter" Hadley cell, through its advection of low-angular-momentum air across the equator (Kraucunas and Hartmann, 2005). Even so, the mean zonal winds increase by roughly 4m/s throughout the troposphere across these simulations, and likely account for a substantial fraction of the increased propagation speed of the MJO and Kelvin waves. In related SP-CAM simulations with an SST maximum of 35°C centered on the equator, we find a westerly mean equatorial wind in excess of

23
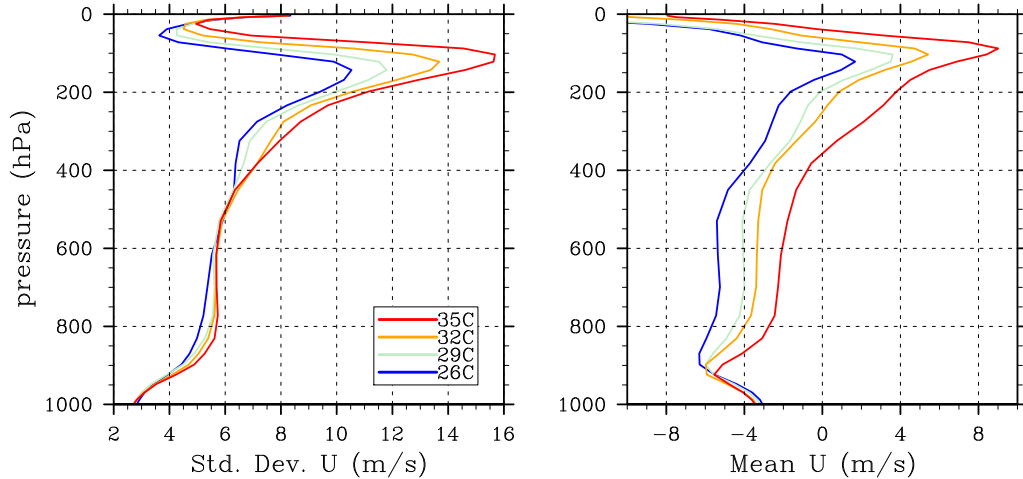
Figure 2.4.1: The daily standard deviation (left) and time- and zonal-mean (right) of equatorial zonal wind between 5°S and 5°N.

20m/s above 200hPa.

To confirm that the MJO is responsible for the westerly trend with SST, we examine the equatorial eddy momentum flux cospectrum, which shows a significant increase in momentum convergence within the MJO band. The zonal-mean meridional fluxes, integrated over the MJO band, is shown in Fig. 2.4.2.

2.5   MOIST STATIC ENERGY BUDGET AND INTENSIFICATION MECHANISM

Comprehensive moist static energy (MSE) budgets have been used in several recent modeling (Andersen and Kuang, 2012, Maloney, 2009) and observational (Kiranmayi and Maloney, 2011) studies to shed light on MJO dynamics. While the datasets and compositing techniques differ, these studies suggest certain common features. In each case, anomalous advective tendencies lead to a buildup of MSE to the east of an existing MSE anomaly, and thus to eastward propagation. The modeling studies (Andersen and Kuang, 2012, Maloney, 2009) find that this advection is dominated by the horizontal component, associated with modulation of synoptic eddies by the

24
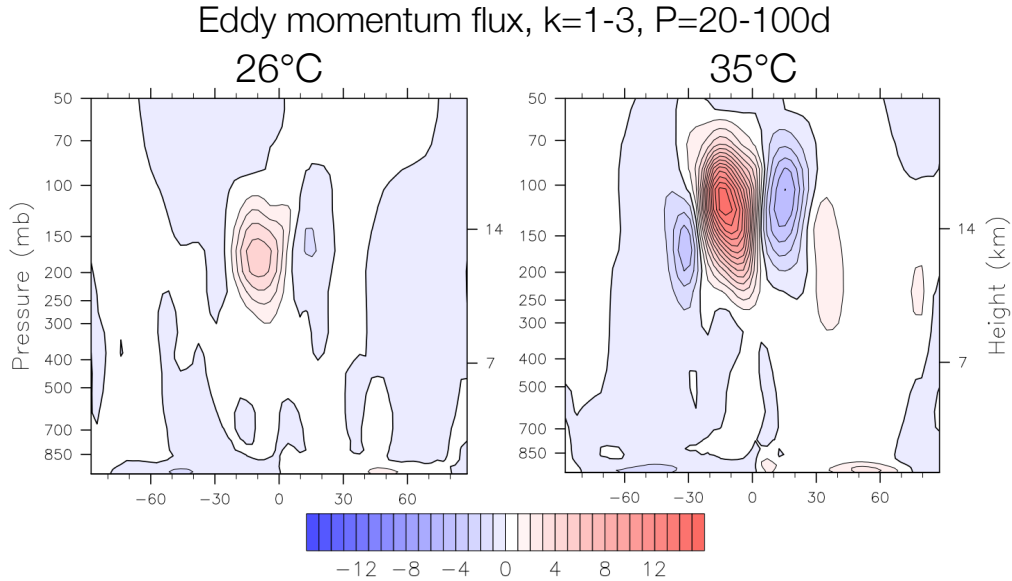
Figure 2.4.2: The zonal- and time-mean meridional flux of zonal momentum by transient eddies with zonal wavenumbers 1-3 and periods 20-100 days. The significant increase in equatorial momentum convergence at high SST is attributable to the stronger MJO.

anomalous large-scale flow, while in reanalysis products (Kiranmayi and Maloney, 2011) the vertical advection plays a larger role. In each case, anomalous radiative heating tends to covary with the MSE, slowing the rate of MSE discharge by convection. The surface fluxes are less consistent, in some cases playing an essential role, and in other cases negligible.

The temporal evolution in all of these composites is consistent with the Recharge-Discharge paradigm of Blade and Hartmann (1993), in which the MJO is described by a buildup of column moisture (MSE) which pre-conditions the atmosphere for deep convection, followed by discharge of MSE during the deep convective phase.

To identify the reason for increasing ISV with SST, we calculate the vertically integrated MSE budgets for composite MJO events, following the methodology of Andersen and Kuang (2012). The vertical integral allows us to avoid dealing explicitly with convective processes, which vertically redistribute, but approximately conserve, MSE. Due to the predominance of high clouds in our region of interest, we use the frozen moist static energy,

$h = gZ + c_pT + L_vq - L_fq_i$, where q is the specific humidity, q_i water ice, Z geopotential height, T temperature, g gravity, c_p the heat capacity of dry air at constant pressure, and L_v and L_f are the latent heats of vaporization and fusion, respectively. This form of MSE is conserved under phase changes including ice formation and melting.

The composites shown here are based on a common linear regression technique (e.g., Andersen and Kuang, 2012, Wheeler and Kiladis, 1999), with the model OLR serving as a reference time-series. The OLR is filtered by computing for each latitude the two-dimensional Fast Fourier Transform (FFT) in longitude and time, retaining only periods of 20-100 days and wavenumbers 1-3, and then taking the inverse FFT. We identify the latitude of maximum filtered OLR variance, and the time-series from all longitudinal points at that latitude are concatenated to extend the series. A similar concatenation is performed with the unfiltered fields of interest (e.g., q, T or $u\frac{\partial h}{\partial x}$), and the fields are regressed (with zero lag) against the filtered OLR. This produces a spatial field of regression coefficients indicating the covariance of a given variable with intraseasonal OLR at the base point. A final composite is created by scaling the regression coefficients by twice the standard deviation of the filtered OLR series for each simulation.

Statistical significance is determined against a null hypothesis of no relationship between the OLR and the composite variable, and coefficients with p-values greater than 0.05 are rejected. In most cases, these constitute a small fraction of the total, and are not indicated on the composite plots for the sake of clarity. In the 26°C case, intraseasonal variability was weak enough that a 10-year simulation only allowed a noisy composite; hence, we will use the 29°C case as the low SST end member in comparisons of composite fields.

We have also tested the robustness of the 35°C composite using an alternate methodology. Following Wheeler and Hendon (2004), we calculated a multivariate EOF-based index using OLR, and 200hPa and 850hPa zonal wind. The two leading EOFs together account for 44% of the intraseasonal variance between 10°S and 10°N, and are well separated from the third mode
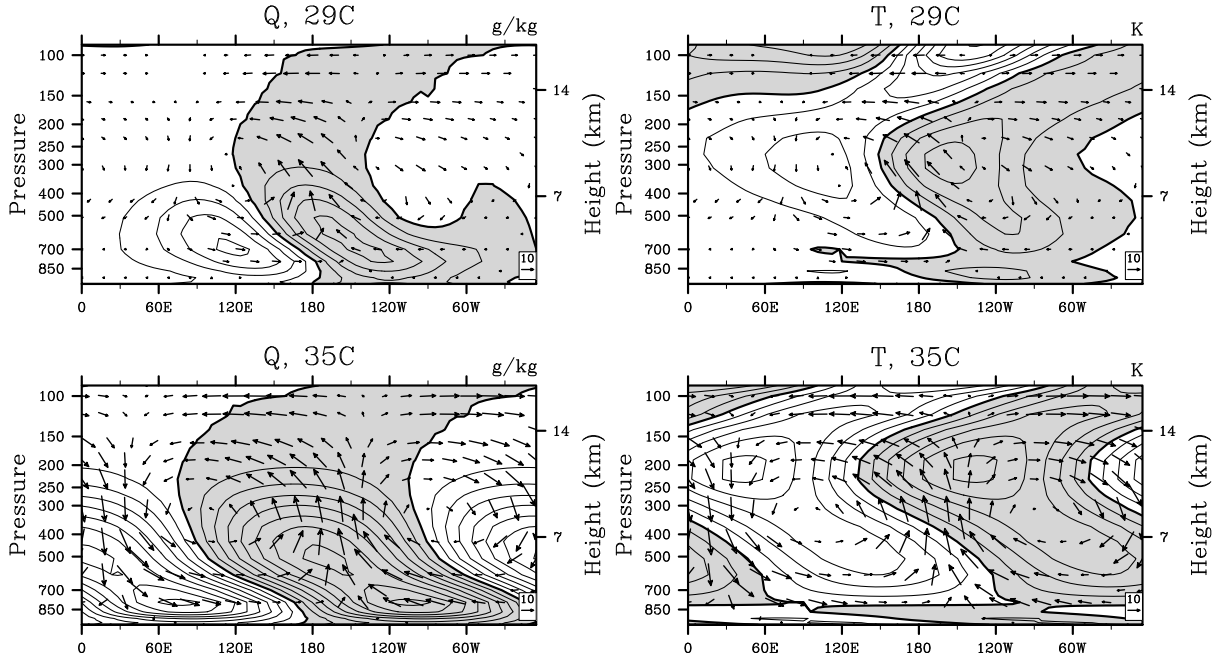
Figure 2.5.1: Equatorial longitude-height profiles of composite specific humidity (left) and temperature (right) for the MJO in the 29°C (top) and 35°C (bot) simulations. Humidity contours are 0.2g/kg, temperature contours are 0.2K, and positive values are shaded. Vertical pressure velocities were multiplied by 300 for plotting purposes, and a 10m/s, 0.03Pa/s reference vector is shown.

(4%). The first two modes have a zonal wavenumber one structure, with a 90 degree relative phase shift, and their PCs are highly correlated (r=0.87) at a 6 day lag, indicating a single propagating mode with a 24 day return time, consistent with the peak in Fig. 2.3.2b. Composites created by linear regression against the first PC are virtually identical to the filtered OLR composites shown in this paper. Due to the higher wavenumber of the MJO at low SST (roughly k=2), an EOF analysis does not neatly capture the MJO variability as two modes in quadrature. We therefore elected not to use this method in constructing our MSE budgets. However, the good agreement seen in the 35°C case reassures us that the filtered OLR composites are also dominated by a single MJO-like mode.

Vertical cross sections of the composite specific humidity, temperature, and wind vectors along the equator are shown in Fig. 2.5.1 for the 29°C and 35°C cases. Again, the greater magnitude

from the high SST run is evident. We also note a significant westward tilt with height in each field. This tilt is seen in observations (e.g., Benedict and Randall, 2007), and is generally attributed to shallow convection in advance of the precipitation maximum, leading to a moistening of the lower troposphere and pre-conditioning the atmosphere for deep convection. The importance of the tilt is unclear, and its appearance with the MJO is irregular in models (Hannah and Maloney, 2011). Hannah and Maloney found that the tilt decreases as a function of convective entrainment rate and rainfall re-evaporation, and note that it does not appear in an aquaplanet version of the conventional CAM. The westward tilt appears less pronounced in SP-CAM simulations with continents and modern boundary conditions (Benedict and Randall, 2009), although this may depend on the compositing method.

The composite 200hPa geopotential height and circulation anomalies for the 35°C case show the familiar double gyre pattern associated with the MJO (Fig. 2.5.2). This pattern is typically interpreted as a Gill-like response (Gill, 1980) to a pair of heating and cooling anomalies on the equator, associated with enhanced and suppressed convection, respectively (e.g., Seo and Son, 2012). Precipitation (shading) is enhanced around 150°W, a region of anomalous ascent and upper level divergence, while anomalous descent, convergence, and suppressed precipitation are centered at 30°E.

We repeat this compositing process for each term in the column-integrated MSE budget,

$$\left\langle \frac{\partial h}{\partial t} \right\rangle = -\langle \mathbf{u} \cdot \nabla h \rangle - \langle \omega \partial_p h \rangle + \langle LW \rangle + \langle SW \rangle + \langle LH \rangle + \langle SH \rangle \qquad (2.1)$$

consisting of horizontal (HA) and vertical advection (VA), longwave (LW) and shortwave (SW) radiative heating, and surface latent (LH) and sensible (SH) heat fluxes, and where

$$\langle \Phi \rangle = \frac{1}{g} \int_{ps}^{ptop} \Phi \, dp$$

28
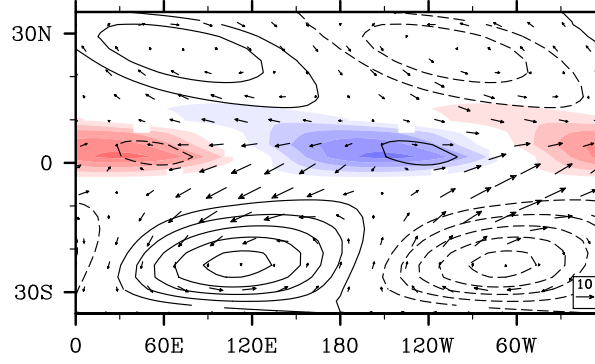
Figure 2.5.2: Precipitation (shading) and 200hPa geopotential height (solid contours) and wind anomalies in the 35°C case. Contour intervals are 2mm/day for precipitation and 12m for geopotential height. A 10m/s wind vector is shown for reference.

is a pressure integral from the surface to the model top.

The spatial structures of the composite budget terms for the 35°C case are shown in Fig. 2.5.3. The column integrated MSE anomaly has a zonal wavenumber one structure with a westward phase tilt toward the poles, while the MSE tendency shows a similar pattern shifted 90 degrees to the east. The largest budget terms involve the advective and radiative tendencies, while latent and sensible surface fluxes are relatively small. Spatial structures in the 29°C and 32°C cases are qualitatively similar, though with a reduced magnitude and zonal extant. A detailed analysis of the 29°C case can be found in Andersen and Kuang (2012).

To estimate the importance of each term in maintaining the composite MSE anomaly, we calculate an area-weighted projection of each term onto the anomaly $\langle h \rangle$. The projection F of a budget term Φ is given by the area integral of the product of $\langle \Phi \rangle$ and $\langle h \rangle$, taken over all longitudes and between 15°S and 15°N, and normalized by $\langle h \rangle$ to give an effective forcing per unit MSE,

$$F_\Phi = \frac{\iint \langle h \rangle \langle \Phi \rangle \ dA}{\iint \langle h \rangle \langle h \rangle \ dA} \tag{2.2}$$

Thus, the fractional change (i.e, the growth rate) of the average squared MSE anomaly $\langle h \rangle^2$ is
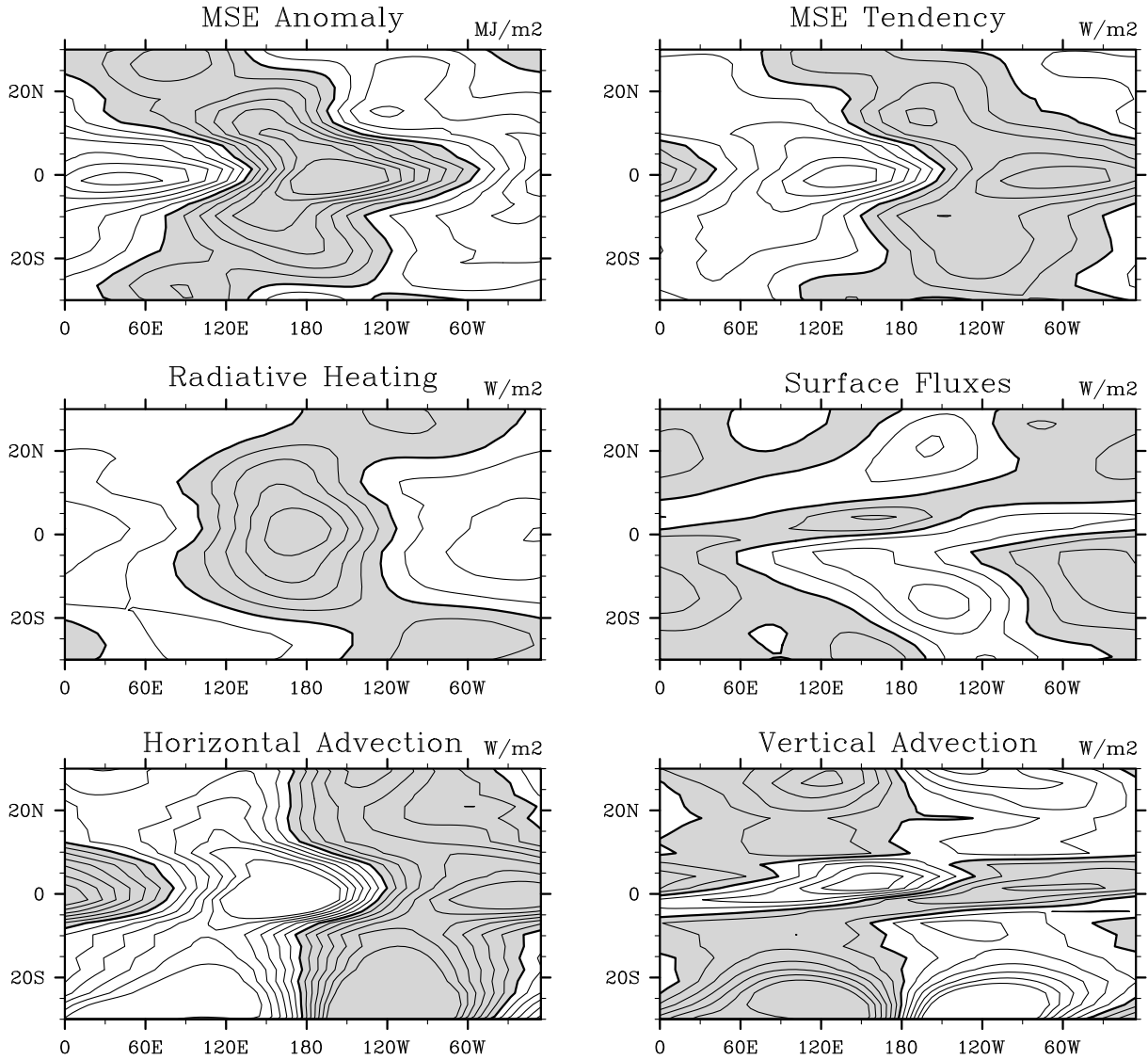
Figure 2.5.3: Terms in the vertically integrated MSE budget for the 35°C case. Contour intervals for the MSE and MSE tendencies (including individual terms) are 2MJ/m^2 and 8W/m^2, respectively. The zero contour is in bold, positive values are shaded.

equal to the sum of the projections of each term in the budget,

$$\frac{\iint \langle h \rangle \langle \partial_t h \rangle dA}{\iint \langle h \rangle^2 dA} = F_{HA} + F_{VA} + F_{LW} + F_{SW} + F_{LH} + F_{SH}$$

Our working assumption is that the increase in intraseasonal variability with SST is related to
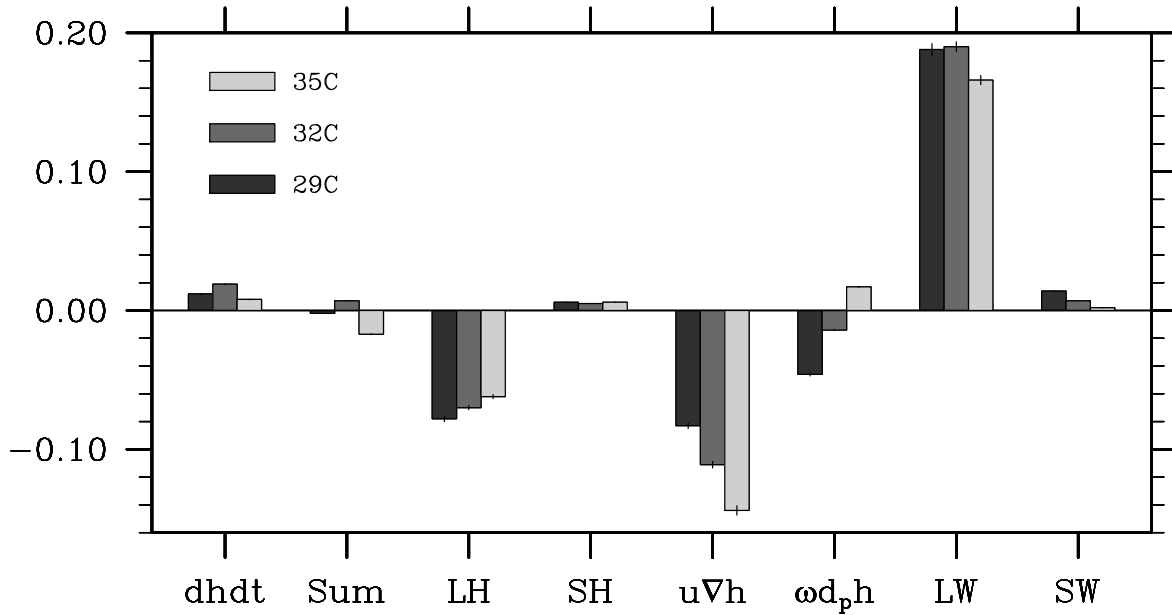
Figure 2.5.4: Projections of each MSE budget term onto the MSE anomaly. A positive trend is seen in vertical advection. The sum of individual terms is shown next to the actual tendency for comparison. Error bars indicate the 95% confidence intervals associated with the regression coefficient at each point in space, propagated through the projection calculations.

changes in one of the normalized terms: either a term providing a positive forcing becomes more efficient (more positive forcing per unit MSE) or a damping term becomes less efficient (less negative forcing per unit MSE). In either case, the projection of the responsible term should increase with SST. In principle, the normalized forcing of every term could remain constant even as MJO activity scales with SST, implying no change in the physical balance maintaining the MJO. Though possible, such a scenario seems unlikely given the strong nonlinearities present in certain terms but not others.

This procedure leads to composite MSE budgets which are qualitatively similar to that of Andersen and Kuang (2012). For all SSTs, the MSE anomaly is almost entirely maintained by longwave heating, which provides the strongest positive forcing (Fig. 2.5.4). These longwave anomalies are largely due to the reduction in OLR by high clouds, with a smaller component

associated with clear sky water vapor (not shown).

The absolute, un-normalized longwave forcing increases with SST as one would expect, but the forcing per unit MSE, F_{LW}, decreases. In particular, we find that the water vapor component of F_{LW} increases slightly, while the cloud-related component decreases by a greater amount. The level of maximum high cloud fraction remains at a constant temperature, consistent with the Fixed Anvil Temperature (FAT) hypothesis of Hartmann and Larson (2002), which predicts that clouds will preferentially detrain near the level of maximum radiatively driven divergence. Since radiative cooling in the troposphere is largely determined by the vertical profile of water vapor, the high cloud fraction becomes closely tied to temperature through the Clausius-Clapeyron relationship. All else being equal, an increase in cloud height with SST implies a positive radiative feedback. However, because the additional water vapor at low levels reduces the upwelling longwave flux, the normalized cloud radiative forcing (i.e., the energetic impact) actually decreases. The combined water vapor and cloud effects lead to the observed decrease in longwave contribution to MSE maintenance (F_{LW}) with SST seen in Fig. 2.5.4.

This decrease indicates that although longwave heating is consistently the largest positive term, it is likely not the cause of the strengthening MJO with increased SST. A more likely candidate is the vertical advection, which provides a negative feedback ($F_{VA} < 0$) at low SST, but becomes increasingly positive as the SST rises. To better understand the source of this change, we decompose the vertical term according to

$$\omega = \overline{\omega} + \omega_{mjo} + \omega_r$$

and

$$\frac{\partial h}{\partial p} = \overline{\frac{\partial h}{\partial p}} + \left(\frac{\partial h}{\partial p}\right)_{mjo} + \left(\frac{\partial h}{\partial p}\right)_r$$

where overbars indicate a time average, the "mjo" subscript indicates a component correlated
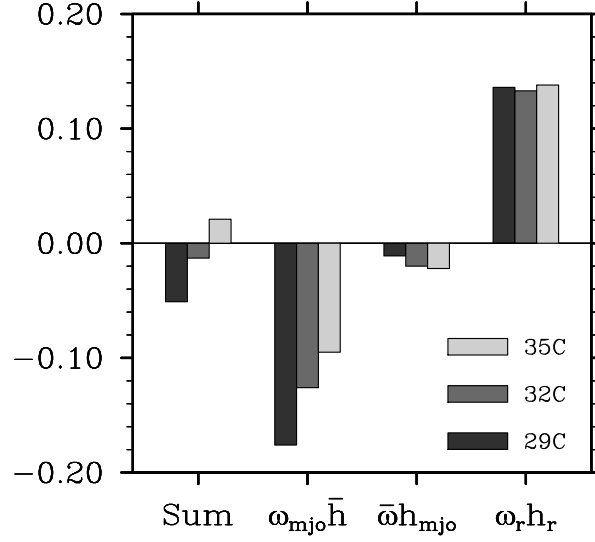
Figure 2.5.5: Projections of each component of vertical advection onto the MSE anomaly, indicating that the positive trend with SST is associated with the MJO vertical velocity acting on the mean MSE gradient.

with the filtered OLR, and "r" indicates the residual. With this decomposition, the product of ω and $\frac{\partial h}{\partial p}$ yields nine terms, six of which have projections on the composite MSE which are nearly or identically zero. The remaining three, $\omega_{mjo}\overline{\frac{\partial h}{\partial p}}$, $\overline{\omega}\left(\frac{\partial h}{\partial p}\right)_{mjo}$, and $\omega_r\left(\frac{\partial h}{\partial p}\right)_r$, are interpreted as the MJO advection of the mean MSE, the mean advection of the MJO perturbation MSE, and MJO modulation of vertical eddy transport. The projection of each component onto the MSE anomaly gives a sense of their relative contributions (Fig. 2.5.5), and indicates that the trend in vertical advection with SST is due to the MJO-related vertical velocity acting on the mean MSE gradient.

The mean vertical gradient, $\overline{\frac{\partial h}{\partial p}}$, is seen to become more positive below 400hPa throughout the model deep tropics (Fig. 2.5.6), and we suggest this may be the fundamental cause of the MJO amplification with SST. This shift is a thermodynamic consequence of maintaining a moist adiabat with little change in relative humidity while the SST is increased, and is effectively determined by the lower boundary condition. One consequence of the shift is to increase $-\omega_{mjo}\overline{\frac{\partial h}{\partial p}}$ in regions of ascent ($\omega_{mjo} < 0$), resulting in slower loss, or greater gain, of column MSE. If regions of anomalous ascent are correlated with regions of high column MSE ($\langle h \rangle > 0$), and descent with
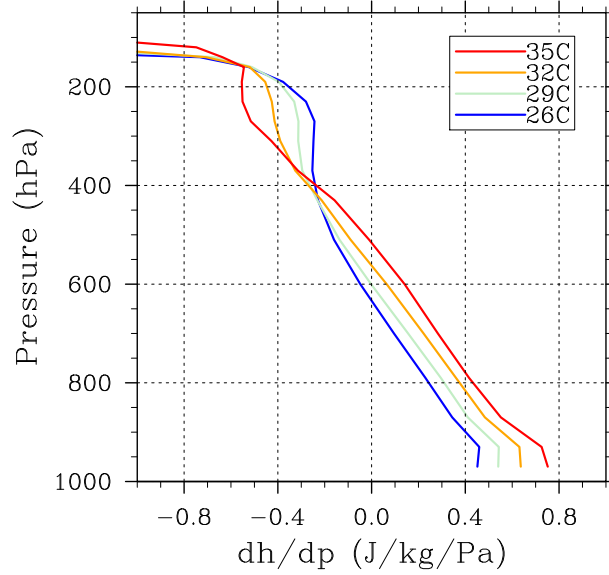
Figure 2.5.6: The mean vertical gradient of MSE, $\partial h/\partial p$, averaged zonally and between 0 and 10°N, is increasingly positive below 400hPa as SST is increased.

low MSE, then all else being equal, the change in MSE profile will make the normalized forcing by the vertical advection term, F_{VA}, more positive (Eq. 2). This can be demonstrated by calculating F_{VA} using MJO vertical velocities and column MSE anomalies for the 29°C case, but substituting the mean MSE gradient, $\overline{\frac{\partial h}{\partial p}}$, from the 35°C case. This results in a change in F_{VA} from -0.18 to -0.06. However, when all fields are taken from the 35°C case, F_{VA} is reduced to -0.09 (Fig. 2.5.5). Thus, the change in $\overline{\frac{\partial h}{\partial p}}$ alone can account for a greater effect than is actually seen in the model. This suggests that shifts in vertical velocity may be partially compensating for the change in $\overline{\frac{\partial h}{\partial p}}$.

In fact, some compensation is expected. The vertical advection term considered here is closely related to the gross moist stability M (Neelin and Held 1987), often defined (e.g., Yu et al 1998) as

$$M = - \int \omega \frac{\partial h}{\partial p} dp$$

It has been pointed out (e.g., Chou and Neelin, 2004) that changes in M with SST involve the near-cancellation of two effects. First, a warmer surface allows greater low-level moisture, which

34

tends to reduce M through its effect on $\frac{\partial h}{\partial p}$. Second, this moisture also tends to increase the depth of convection, altering the profile of ω and causing M to increase. The observed gross moist stability is nearly constant throughout the tropics as a result of this balance (Yu et al., 1998). In our simulations, the first effect appears to exceed the second, allowing a decrease in M and an increase in F_{VA}.

2.6 DISCUSSION

In addition to the generic issues of an aquaplanet configuration, there are other differences in physics and boundary conditions which may affect the relevance of our results to MJO behavior in warm climates. Our simulations use fixed ocean surface temperatures, with the same meridional gradient specified independent of the mean temperature. Interactive SST has been shown to improve MJO simulation and enhance intraseasonal variance, although it does not appear to be critical to the generation of an MJO (e.g., Kemball-Cook et al., 2002, Maloney and Sobel, 2004). We note that although the SST is held fixed in our runs, surface fluxes may still vary as a function of the atmospheric state, and do contribute to the MJO energy budget. Benedict and Randall (2009) suggest that use of interactive SST may reduce intraseasonal variance in SP-CAM.

The meridional SST gradient may also affect MJO behavior, and a multitude of modeling and observational evidence suggests that the gradient tends to weaken in warmer climates. The dependence of organized convection on the meridional gradient was not systematically studied here, and results from existing studies are ambiguous. Grabowski (2004) found robust MJO-like variability in a model with globally uniform SST, suggesting that gradients are at least not fundamental to the MJO, while Maloney et al. (2010) found that intraseasonal variability increased in an aquaplanet version of CAM3 when the prescribed meridional SST gradient was reduced. The MJO scaling does appear to depend on the pattern of warming(Maloney and Xie, 2013).

Despite the idealizations listed above, the MJO simulated here maintains a structure in humidity, temperature and wind that qualitatively resembles observations, and varies principally only in magnitude across the simulations presented here. As in many previous studies, it appears to be consistent with the Rechange-Discharge paradigm (Blade and Hartmann, 1993), in which the MJO timescale is determined by the buildup and discharge of environmental humidity, as well as the idea that the MJO is a "moisture mode" (Raymond and Fuchs, 2009), which requires an effectively negative gross moist stability for its existence.

The present work differs from some previous composite MSE budgets. While many models suggest a dominant or essential role for latent heat fluxes (Maloney et al., 2010, Sobel et al., 2008b), the MJO simulated here and in Andersen and Kuang (2012) is principally supported by longwave heating. This term is usually secondary in other models, serving as a positive feedback rather than a pre-requisite for instability. Grabowski (2004), for example, found that interactive radiation was unnecessary to produce an MJO. It is not entirely surprising that both radiative heating and surface fluxes can play a dominant role in intraseasonal variability, depending on the model. Both processes have similar energetic effects, resulting in a net transfer of heat from ocean to atmosphere, and are somewhat interchangable as far as the column MSE is concerned (Sobel et al., 2008a). These terms were combined by Kiranmayi and Maloney (2011) in their composite MSE budget of observed MJO events, and it is unclear whether a single process is dominant in the real world.

Determining the mechanism behind the MJO increase with SST based on trends in composite MSE budget terms (Eq. 2.1) relies on a number of assumptions. The composite budgets presented here represent not only an estimate of some "average" MJO event, but an average over the full lifecycle of that event; they do not account for differences between growth, decay, or steady-state phases. For example, longwave heating per unit MSE could be greater than average during the period of initial MSE anomaly growth, and less than average during decay. Note that growth/decay here refers to the amplitude of the global pattern of MSE anomaly, rather than the

trend at a single point in space, which would vary throughout an MJO event due to pattern propagation even if the pattern amplitude remained constant. We have explored limiting the composite to periods of pattern growth or decay, and found qualitatively similar results; for example, the trend in vertical advection appears to be robust. However, due to the shorter effective timeseries, these growth/decay period composites tend to be noisy, and are not shown.

A single budget term may also reflect several distinct physical processes, e.g., longwave heating is associated with both cloud and water vapor anomalies, horizontal advection can be related to the mean flow and transient eddies, etc. Suppose that two physical processes, A and B, are contained within the same budget term Φ, so the projection is given by $F_\Phi = F_A + F_B$. An increase in SST may produce a positive change in F_A, which leads to a larger MSE anomaly. Since the anomaly does not grow indefinitely, the positive change in F_A is ultimately balanced by negative changes elsewhere (i.e., nonlinear damping). If these negative changes were confined to F_B, then F_Φ would show no net change, and we may conclude that a different term was responsible for the larger MSE anomaly. One defense against this possibility is to decompose each budget term into component physical processes where possible. It also seems unlikely that the additional damping would be contained entirely in the same term as the additional forcing; in Fig. 2.5.4, every significant term but one (longwave heating) is acting to dissipate the MSE anomaly, and every term but two - latent heat fluxes and vertical advection - show a negative trend with SST.

2.7 SUMMARY

We have found that tropical intraseasonal variability in a super-parameterized version of the NCAR Community Atmosphere Model is strongly dependent on the prescribed value of mean sea surface temperature. In aquaplanet simulations with equatorial SST near 26°C, 29°C, 32°C and 35°C, the intraseasonal (wavenumbers 1-3, periods 20-100 days) variance increases

dramatically and monotonically with SST. The intraseasonal variance of outgoing longwave radiation, for example, triples between the 26°C and 35°C cases, and the ratio of eastward to westward propagating variance increases from 1.95 to 6.27. The intraseasonal variance in all simulations is dominated by a global-scale, eastward-propagating convective disturbance which resembles the observed Madden Julian Oscillation (MJO).

A similar increase in MJO-like variability was previously reported in the conventional version of CAM (Caballero and Huber, 2010), although no mechanism was proposed, and the model's lack of MJO simulation skill under modern conditions makes interpretation problematic. These models are similar, but those aspects in which they differ most - their representations of convection and radiative transfer - lie at the heart of MJO physics, suggesting that this behavior may be fairly robust.

We explored the reasons for the intraseasonal variance increase in SP-CAM by calculating a column-integrated moist static energy (MSE) budget for a composite MJO event. The contribution of each term to the steady-state maintenance of the MJO-related MSE anomaly was estimated from the spatial projection of each budget term onto the anomaly. Consistent with previous work by Andersen and Kuang (2012), this analysis indicated that the MSE anomaly is primarily supported by the radiative effects of high clouds, while anomalous horizontal advection drives eastward propagation. However, as SST is increased, both of these terms show increasingly negative projections on the anomaly, and thus cannot be responsible for the observed amplification. In contrast, the projection of vertical advection shows a positive trend: at low SST it provides a strong damping, but it becomes an energy source at high SST. This leads us to conclude that changes in vertical MSE advection are likely responsible for the increase in MJO variability with SST.

A decomposition of the vertical advection term indicates that its positive trend with SST is associated with the intraseasonal vertical velocity acting on the mean MSE gradient. We suggest that an increase in the mean MSE vertical gradient in the model's tropical lower troposphere may

be a contributing factor. This would serve to increase the MSE buildup associated with a given vertical mass flux, and effectively reduce the gross moist stability. This change in the MSE profile is a direct consequence of increasing SST while maintaining a moist adiabat and fixed relative humidity, and should be a robust feature of warm climates.

This behavior warrants further investigation with independent models, in particular those outside the NCAR family of models. Unfortunately such studies are few, and generally do not examine the physical mechanisms for changes in MJO behavior. Lee (1999) noted an increase in intraseasonal variance in a GFDL AGCM after a uniform $2°$C SST increase, and Huang and Weickmann (2001) reported a trend in equatorial zonal winds in a transient global warming simulation with the Canadian Climate Centre Model, which the authors speculate was driven by changes in equatorial variability.

This work has implications for past warm climates, as well as future scenarios in which greenhouse gas emissions remain unchecked. Previous work has linked the MJO to a number of climate phenomena, including the Asian and Australian monsoons (e.g., Wheeler and Hendon, 2004), ENSO (e.g., McPhaden, 1999), tropical cyclogenesis (e.g., Frank and Roundy, 2006), and dynamic warming of the Arctic (Lee et al., 2011). Changes in any one of these could have significant impacts on human society. We also note that the MJO has a non-negligible impact on the equatorial momentum budget (Lee, 1999); this is due to the tilted upper-tropospheric gyre circulations associated with organized convection, which produce equatorward fluxes of westerly momentum.

Increases in MJO activity could lead to reduced equatorial easterlies, which might be sufficient to explain the Pliocene "Permanent El Niño" seen in proxy SST data, through their impact on upwelling (Tziperman and Farrell, 2009). Sufficiently large increases in MJO activity could lead to outright westerly winds or superrotation (Held, 1999a, Pierrehumbert, 2000), though if the sensitivity to SST seen in SP-CAM is an accurate reflection of the real world, strong superrotation would require surface temperatures last seen during the Eocene (Pearson et al., 2007).

3

The MJO Response to Warming in SP-CESM

3.1   INTRODUCTION

In this chapter, we extend the aquaplanet analysis of Chapter 2 to a more realistic case. A fully coupled atmosphere-ocean model is run with pre-industrial and quadrupled CO_2 to simulate the Madden-Julian Oscillation (MJO) in relatively warm and cold climates.

To briefly review, the MJO consists of a broad envelope of enhanced convection that forms episodically over the Indian Ocean, propagates slowly eastward at around 5m/s, and dissipates over the central Pacific (Madden and Julian, 1971, Zhang, 2005). The convective signal is coupled

to a large scale overturning circulation which suppresses deep convection in neighboring longitudes, and closely resembles a forced Rossby-Kelvin response (Gill, 1980, Matthews et al., 2004). In addition to its direct impact on tropical rainfall, the MJO is known to modulate the Asian, Australian and West African monsoons (Lavender and Matthews, 2009, Pai et al., 2011), tropical cyclogenesis (Hall et al., 2001, Maloney and Hartmann, 2000), and affects the timing of El Niño onset and decay (McPhaden, 1999). Anticipating future changes in the MJO is therefore of great interest to human society.

The MJO may also help explain notable features of past climates. As noted in previous chapters, the MJO is known to excite Rossby waves which, in propagating to higher latitudes, flux westerly momentum into the tropics and drive the atmosphere toward a superrotating state (Caballero and Huber, 2010, Grabowski, 2004, Lee, 1999). This has been proposed as an explanation for the Pliocene "permanent El Niño", an apparent disappearance of the equatorial cold tongue from 2-5Ma. If MJO activity were enhanced in the (2-3K) warmer Pliocene climate (Dowsett et al., 2011), this would lead to more tropical momentum convergence, weakening the equatorial easterlies and allowing the east-west Pacific thermocline slope to relax, and thereby explaining the observed warm anomalies in the Pliocene east Pacific (Tziperman and Farrell, 2009).

Our understanding of MJO dynamics remains incomplete, and any future change in MJO behavior is likely to depend on the future tropical mean state, itself an uncertain quantity. This combination makes projecting MJO behavior a particularly challenging endeavor. Nevertheless, a number of studies have addressed this question with varying degrees of directness through analysis of historical trends and numerical experiments.

Slingo et al. (1999) examined interannual variation in MJO activity in NCEP/NCAR Reanalysis and the Hadley Centre climate model (HadAM2a) and found that while year-to-year variability appears to be chaotic, decadal-scale changes suggest a dependence on surface temperature. MJO activity was consistently weaker prior to the mid-1970s, when SSTs were cooler. This led Slingo et al. to suggest that the MJO may become more active with global

41

warming. These findings were echoed by Hendon et al. (1999) using a different methodology. Both studies found a weak relationship with ENSO, with reduced MJO activity during warm phases. To the extent that a future pattern of warming is more or less "El Niño"-like (Yamaguchi and Noda, 2006), this may also contribute to MJO changes.

More recently, Jones and Carvalho (2006) and Oliver and Thompson (2012) have studied trends in MJO indices calculated from reanalysis products over the last 50 and 100 years, respectively. Both found weakly positive linear trends. Jones and Carvalho (2011) used a statistical model trained to observations to make projections of significantly enhanced future MJO activity, based on late 21st Century mean states from CMIP3 model projections.

Enhanced MJO activity with warming has also been seen in some numerical simulations. Lee (1999) found much stronger MJO activity after a prescribed increase in SST in an aquaplanet GCM. Caballero and Huber (2010) found that the NCAR CAM3 becomes dominated by an MJO-like mode at very high SST, and a high resolution (40km) version of ECHAM5 run with an A1B warming scenario simulates an increase in MJO variance (Liu et al., 2012). On the other hand, an analysis of 12 CMIP3 models by Takahashi et al. (2011) found little agreement even on the sign of MJO change. However, this set of models is known to have low MJO simulation skill (Lin et al., 2006), so their lack of agreement is not surprising. Maloney and Xie (2013) found that MJO activity in a modified version of CAM3 is sensitive to the spatial pattern of warming, which may also contribute to the inter-model spread in MJO behavior.

There is theoretical reason to suspect the MJO will intensify in warmer climates. One leading paradigm describes the MJO as a moisture mode, arising from feedbacks between convection and environmental moisture. Since the scaling of atmospheric moisture with temperature is controlled by the Clausius-Clapeyron relationship, one might suppose that at least the moist aspects of the MJO could scale at a similar exponential rate. However, the relationship between moisture mode theory and the observed MJO is still poorly understood, and a specific amplification mechanism is not obvious.

In the previous chapter we proposed a physical mechanism for MJO intensification based on a set of aquaplanet simulations with increasing SST. Analysis of the moist static energy budget linked the MJO increase to changes in vertical advection, which were due in turn to a steeper mean MSE profile at high SST. This steepening is based on fundamental thermodynamics and quite robust, but it can be offset by changes in the vertical velocity profile, which is less well constrained. It may be that the aquaplanet configuration is unrealistically favorable to MJO intensification.

This chapter aims to reinforce the aquaplanet results using simulations with more realistic boundary conditions, including a seasonal cycle, continents and a dynamic ocean. The model and experimental setup are described in detail in Section 3.2. In Section 3.3, we compare the simulated mean state and MJO with observations. Section 3.4 presents changes in the mean state and in MJO activity resulting from increased CO_2. In Section 3.5 we present a composite moist static energy budget and examine the physical processes sustaining the MJO and leading to intensification. Our conclusions are summarized in Section 3.6.

3.2   Model Description and Experimental Setup

The MJO has a reputation for being difficult to simulate, and most GCMs produce intraseasonal disturbances that are both too weak and too rapidly propagating (Lin et al., 2006). Our understanding of these deficiencies has improved over the last decade (e.g., Thayer-Calder and Randall, 2009), with commensurate improvement in model MJO skill (e.g., Neale et al., 2008), though often at the expense of the tropical mean climate (Kim et al., 2011). Here we use a super-parameterized model, in which sub-grid convective tendencies are explicitly generated by Cloud System Resolving Models (CSRMs) embedded within each GCM column (Grabowski, 2001, Randall et al., 2003). Super-parameterizations (or Multi-scale Modeling Frameworks; Grabowski (2001)) have been implemented in several GCMs, and show promising

improvements to many aspects of convection (e.g., Pritchard and Somerville, 2009). In the context of the historical challenge noted above, they are particularly noteworthy for their realistic simulation of the MJO (Andersen and Kuang, 2012, Benedict and Randall, 2009, Grabowski, 2004), although its representation does appear to depend on the particular SP implementation. More attention may have been given to tuning in early versions, yielding better results (Pritchard and Bretherton, 2013).

In this study, the host GCM is the NCAR Community Atmosphere Model, with the finite volume dynamical core and CAM4 physics on a $1.9° \times 2.5°$ horizontal grid with 30 levels in the vertical. This is run as the atmospheric component of the Community Earth System Model (CESM1.0.4), coupled to dynamic ocean (POP2) and sea ice (CICE) models on a roughly $1.125° \times 0.63°$ grid, with a displaced pole. The embedded CSRM is the System for Atmospheric Modeling (SAM6; Khairoutdinov and Randall (2003)), run with a two-dimensional domain consisting of 32 columns of 4km width, oriented in the east-west direction, with 28 vertical levels co-located with the 28 lowest levels of CAM. The CSRM uses a five-species bulk microphysical parameterization.

To spin-up the model, we first ran two simulations with the conventional (non-SP) version of CESM. The first was run for 50 years with pre-industrial (280ppm) CO_2, and the second with CO_2 concentrations increasing at 1% per year until they quadrupled (1120ppm), at which point they were held steady for 50 years. Two super-parameterized runs, denoted $1 \times CO_2$ and $4 \times CO_2$, were initialized from the end of these conventional simulations and run for an additional 10 years. The first two years were discarded to allow for re-equilibration, and the remaining eight years were used for all analysis presented in this chapter.

At a given level of CO_2, SP-CESM has a slightly cooler tropics than CESM; the tropical-mean temperatures in the last eight years of the SP-CESM $1 \times CO_2$ and $4 \times CO_2$ scenarios are 1.2K and 0.6K cooler, respectively, than the corresponding equilibria in CESM. The last eight years show small linear cooling trends of less than 0.09K/yr and 0.03K/yr, relative to detrended interannual
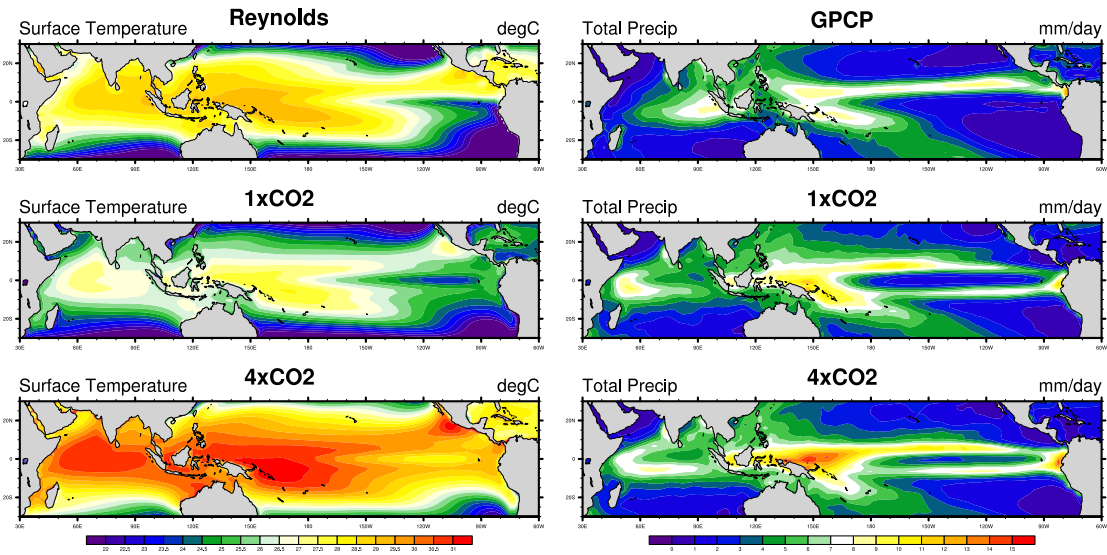
Figure 3.2.1: Annual-mean SST (left) and total precipitation (right) from observations, and $1\times CO_2$ and $4\times CO_2$ simulations. The $1\times CO_2$ fields generally agree with observations, despite a pervasive 1K cool bias and notable discrepancies in the west Indian and east Pacific oceans. The $4\times CO_2$ case shows widespread warming and stronger rainfall along the ITCZ.

standard deviations of 0.2K/yr and 0.15K/yr. We therefore expect any remaining energy imbalance to have minimal effect on MJO behavior.

3.3   Mean state and MJO at $1\times CO_2$

The annual-mean sea surface temperature and surface precipitation from the pre-industrial simulation are compared with two observational datasets in Fig. 3.2.1 . We use the Reynolds SST climatology from 1971-2000 (Reynolds et al., 2002) and the GPCP precipitation climatology from 1979-2000 (Adler et al., 2003).

   The model exhibits a widespread cold bias of roughly 1K across the Indian Ocean and West Pacific, and particularly around central America. A strong warm bias in the east Pacific is seen around the Humboldt and California currents. This bias pattern is roughly constant across seasons, although the cold bias is stronger in the subtropics in the summer hemisphere. A bias in

the spatial pattern is potentially more problematic than one in the tropical-mean, as it can distort the surface wind field and the patterns of mean precipitation and precipitation variance. Figure 3.2.1b shows the annual mean precipitation has a pronounced double ITCZ, likely associated with the east Pacific warm bias. The eastern subtropical dry zones are also too small, and precipitation over the Indian ocean is shifted too far west.

Anomalous surface enthapy fluxes induced by windspeed variation played a central role in early MJO theories (Emanuel 1987; Neelin 1987), and although these theories were found to be inconsistent with observations, surface fluxes are still thought to be important to the MJO (Sobel et al 2010). In nature they are positively correlated with intraseasonal precipitation (Araligidad and Maloney 2008), but their role in models is somewhat less consistent, in some cases playing a destabilizing role (Bellon and Sobel, 2008, Grabowski, 2003, Maloney and Sobel, 2004) and weakening intraseasonal variance in others (Andersen and Kuang, 2012, Kim et al., 2011, Maloney, 2002). Areas of low-level westerlies over the Indian ocean are thought to be important in maintaining the correct phasing between surface fluxes and precipitation in the MJO (Inness and Slingo, 2003), and errors in the simulated mean state can therefore influence MJO instability and propagation (Zhang et al., 2006). In the SP-CESM $1 \times CO_2$ case, the Indian ocean surface winds are predominantly easterly, likely due to the shifted Indian ocean precipitation noted above, and this may result in an unrealistic role for surface fluxes.

To assess the model MJO, we first compare the simulated tropical variability in outgoing longwave radiation (OLR) to the NOAA NCEP Climate Prediction Center (CPC) product of interpolated satellite observations from 1981-2000 (Liebmann and Smith, 1996). Equatorial wavenumber-frequency spectra in Fig. 3.3.1 suggest that the model underestimates tropical variability at all scales relative to the CPC dataset. However, the Kelvin, Rossby, and Inertia-Gravity wave bands do show realistically elevated power relative to the weak background, and simulated phase speeds agree with those observed, consistent with an equivalent depth of
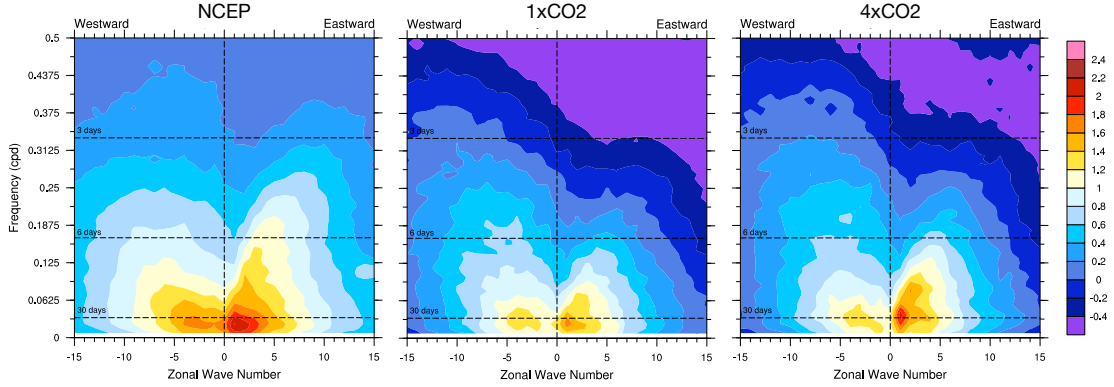
Figure 3.3.1: Wavenumber-frequency equatorial power spectra of outgoing longwave radiation (OLR) from NCEP Reanalysis (a), and $1\times CO_2$ (b) and $4\times CO_2$ (c) simulations. SP-CESM generally underestimates tropical OLR variability, but shows realistically elevated power in the shallow-water wavebands. A peak associated with the MJO is seen in $1\times CO_2$, which increases in magnitude and frequency at $4\times CO_2$.

25-50m (Wheeler and Kiladis, 1999). Within the MJO band (defined in this chapter as zonal wavenumbers 1-3 and periods of 20-100 days), the OLR variance is weaker than observed, and the ratio of eastward to westward (negative wavenumbers) power is 1.6, compared with 2.4 in the CPC dataset. The eastward/westward power ratio in precipitation is 2.8, which compares better to the GPCP-derived value of 2.5.

To evaluate the MJO's detailed spatial structure, we create composites of MJO anomalies using the method of Wheeler and Hendon (2004). Deviations from a daily climatology of 200hPa and 850hPa zonal wind, and OLR are averaged in latitude between $15°$S and $15°$N, band-pass-filtered between 20 and 100 days, then normalized by their respective zonal-mean temporal standard deviations. The two leading principal components (PCs) from a combined EOF analysis define an MJO index, with amplitude $\sqrt{PC1^2 + PC2^2}$ and phase angle determined from the PCs. In the $1\times CO_2$ run, the first two modes explain 41% of the combined-field intraseasonal variance and are maximally correlated (r=0.78) at a lag of 9 days, indicating a 36 day period. The EOFs are shown in Fig. 3.3.2a. Their spatial structure resembles observations (Wheeler and Hendon,
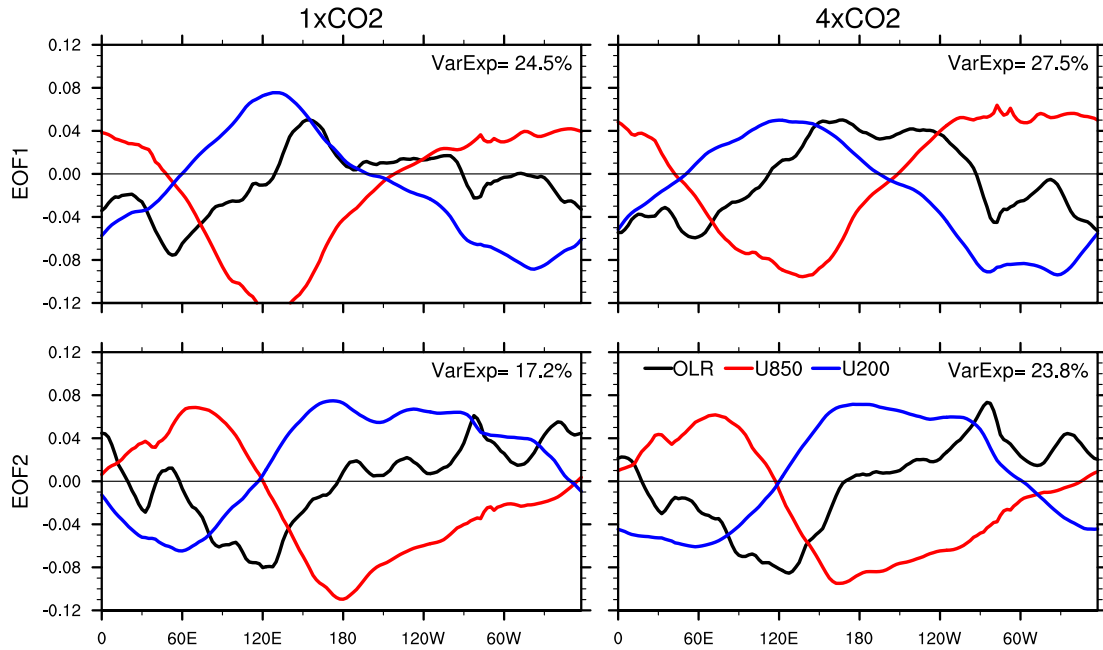
Figure 3.3.2: The two leading combined EOFs of meridionally-averaged OLR (black), U850 (red) and U200 (blue). The percentage of combined variance explained by each mode is indicated in the top right. The spatial structures are qualitatively similar in both cases, but the EOFs explain a larger fraction of the (increased) intraseasonal variance with $4\times CO_2$.

2004), and changes little in the $4\times CO_2$ case.

Composites are created by band-pass filtering anomalies and then averaging within each phase during periods when the index amplitude exceeds 1. A composite of OLR, precipitation and 850hPa winds in boreal winter (November-April) is shown in Fig. 3.3.3. The structure closely resembles composites of observations, with similar amplitude, primarily eastward propagation, and southward migration within the Pacific sector. Composites for boreal summer (May-October, not shown) show similar fidelity to observations. The pattern of intraseasonal variance is seen to migrate between hemispheres following the seasonal cycle, with peak variability in boreal winter and a secondary peak in boreal summer, in agreement with observations (Zhang and Dong, 2004).

We conclude that, despite some differences between the modeled and observed mean states,
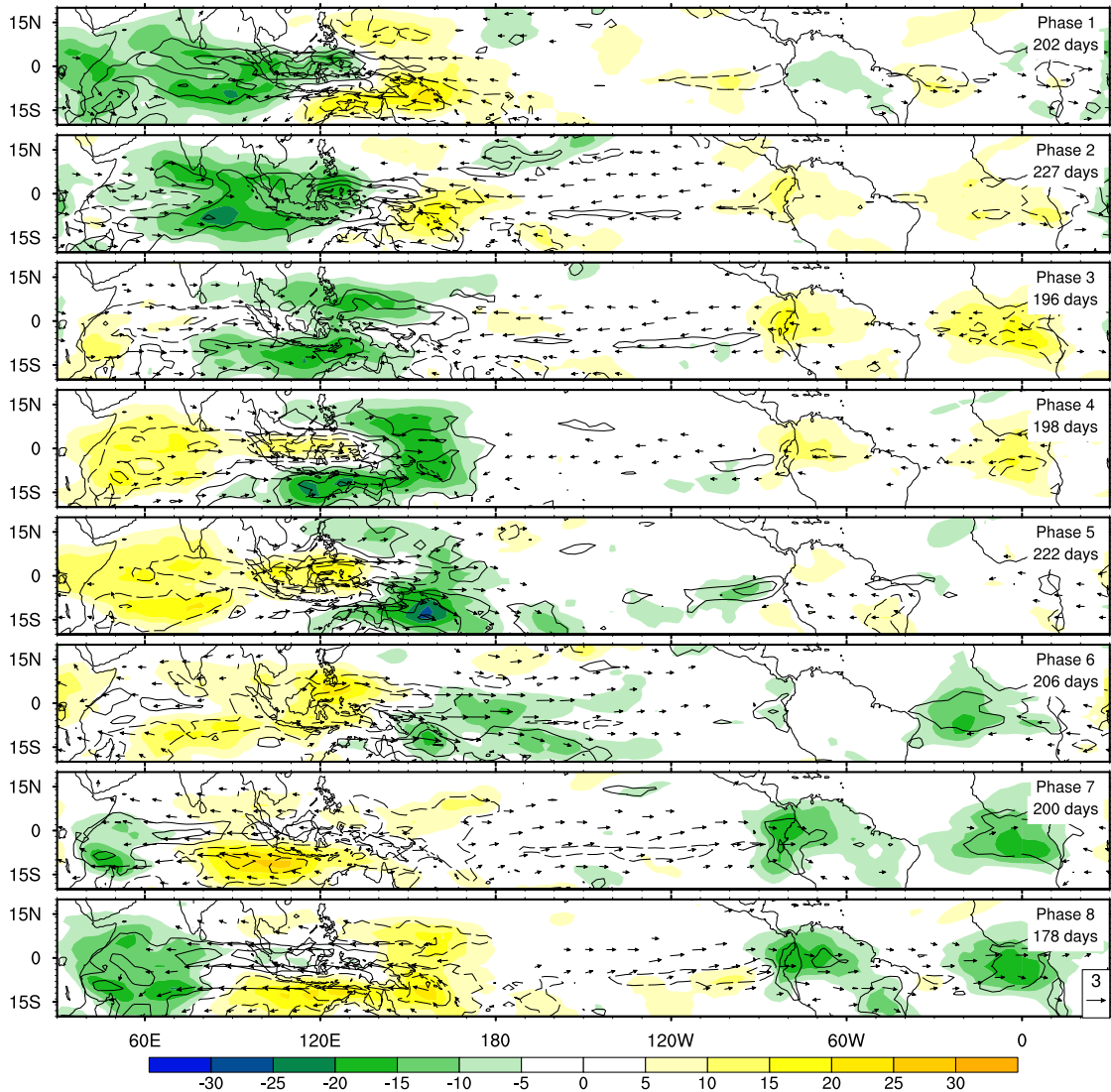
Figure 3.3.3: Composite OLR (colors), precipitation (contours) and 850hPa wind anomalies averaged within each MJO phase for $1 \times CO_2$ simulation. Precipitation contour interval is 2mm/day. The MJO phase and number of days included in each average is indicated in the upper right. A 3m/s reference vector is shown in the lower right.

SP-CESM simulates a robust MJO, with generally realistic variance, spatial structure, propagation, and seasonality.

Table 3.4.1: Metrics of tropical variability based on daily precipitation (mm/day), OLR (W/m^2) and U850 (m/s). Shown are the total (Tot) and MJO-band (MJO; k=1-3,P=20-100d) longitudinal-temporal standard deviations, and the ratio of eastward to westward MJO-band variance (E/W). Precipitation and OLR show increases in total variability, with larger fractional increases within the MJO band. Total zonal wind variability decreases, but a small increase is seen within the MJO band. The number of events per year identified from the Wheeler-Hendon index increases from 4.4 to 5.6.

	Precip			OLR			U850			
	Tot	MJO	E/W	Tot	MJO	E/W	Tot	MJO	E/W	Ev/Yr
$1\times CO_2$	4.46	0.81	1.67	28.7	6.52	1.35	3.34	1.25	1.65	4.4
$4\times CO_2$	6.28	1.27	2.20	32.2	8.65	1.80	3.36	1.27	1.81	5.6

3.4 MEAN STATE CHANGES AND MJO INTENSIFICATION WITH WARMING

The tropical-mean surface temperature is 4.2K warmer in the $4\times CO_2$ simulation, with enhanced warming in the east Pacific cold tongue along the coasts of South and Central America, as well as in the subtropics of the summer hemisphere (Fig. 3.2.1). Annual-mean precipitation increases primarily along the ITCZ.

The magnitude of MJO activity is typically estimated from the intraseasonal variance in fields associated with moist convection (e.g., OLR, precipitation). Because these variables scale differently with warming, we list several metrics for each field in Table 3.4.1 in order to provide a more comprehensive picture. The total longitudinal-temporal standard deviation (Tot) of each field, averaged between 10°S and 10°N, is listed to provide a measure of the background variability, while the standard deviation within the MJO-band (MJO; wavenumbers 1-3, periods 20-100 days) and the ratio of eastward to westward MJO-band variance (E/W) provide a measure of MJO-related variability. These numbers were calculated by averaging each field in latitude, calculating the wavenumber frequency power spectrum, integrating over the desired waveband and then taking the square root.

The standard deviation of total precipitation scales at roughly 7% per degree of warming, while

within the MJO band the scaling is somewhat larger, at 9.5%/K. We note that the tropical-mean (20°S-20°N) precipitation, being subject to energetic constraints (Held and Soden, 2006), scales at a more modest 2%. The total OLR standard deviation increases at roughly 3%, with a larger increase of 8% in the MJO band. By contrast, the total zonal wind variability decreases, though the intraseasonal band still shows a small increase. This insensitivity of wind variability to warming was also noted by Maloney and Xie (2013), who attributed it to increases in static stability which make anomalous convective heating less efficient at inducing wind anomalies.

It is apparent that the convective aspects of the MJO intensify, but these are also embedded within a more variable background state. At $4\times CO_2$, the two leading modes explain 51% of the intraseasonal variance; not only does this variance increase, it also appears to be more structured.

The increases in MJO convective variance come in the form of both a greater number of events, and a larger amplitude per event. The $4\times CO_2$ composite of anomalous OLR and precipitation is shown in Fig. 3.4.1, and comparison with Fig. 3.3.3 makes evident the increase in amplitude. To count individual MJO events, we use a metric based on the MJO index defined above. Events are defined for each active period in which the index amplitude remains above one, and during which the MJO phase progresses eastward through at least 180 degrees. For cases of multiple events in sequence, with the index amplitude remaining above one, we round the total phase progression to the nearest multiple of 360 degrees. That is, one event is indicated by $180° < \Delta\phi < 539°$, two events by $540° < \Delta\phi < 899°$, and so on.

The criteria above yield 4.4 events per year at $1\times CO_2$, and 5.6 events per year at $4\times CO_2$. Although the absolute numbers change somewhat depending on the choice of minimum amplitude and phase progression, the 20-30% increase in event number between $1\times CO_2$ and $4\times CO_2$ is insensitive to parameter choice. We also find that the length of a full 360° oscillation decreases from 42 to 33 days. This is associated with an increase in eastward propagation speed, clearly visible in lag-correlation plots (Fig. 3.4.2).
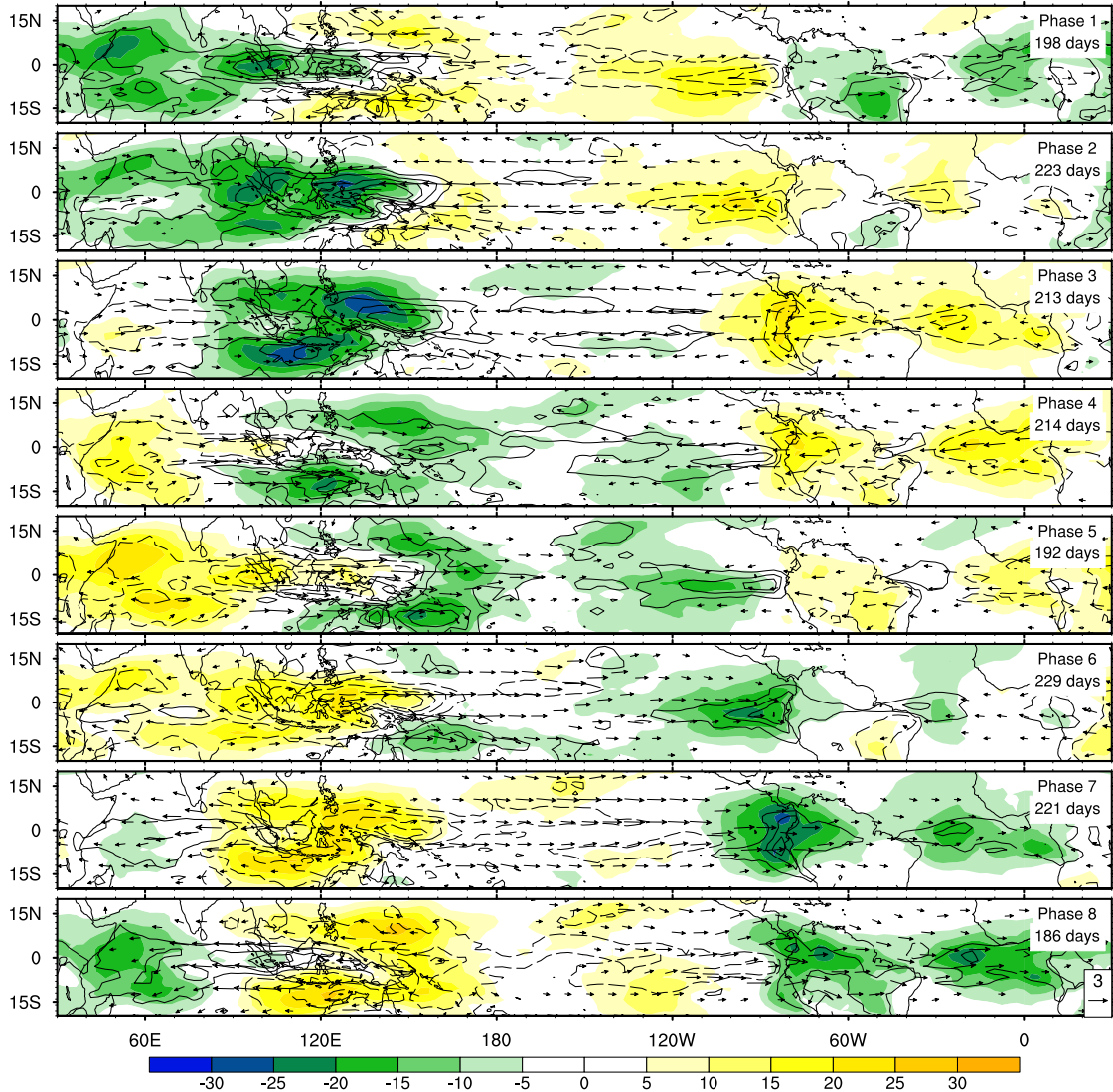
Figure 3.4.1: Composite OLR, precipitation and 850hPa winds for $4\times CO_2$, as in Fig. 3.3.3. The amplitude of OLR and precipitation anomalies in most phases is visibly larger than the $1\times CO_2$ case, and convective anomalies in the Pacific are more robust.

3.5 Moist Static Energy Budget and Intensification Mechanism

Our confidence in the simulated changes to the MJO can be enhanced by identifying physical connections between changes in MJO characteristics and robust changes in the mean state. To this end, we calculate the moist static energy (MSE) budget of a composite MJO event. This

52
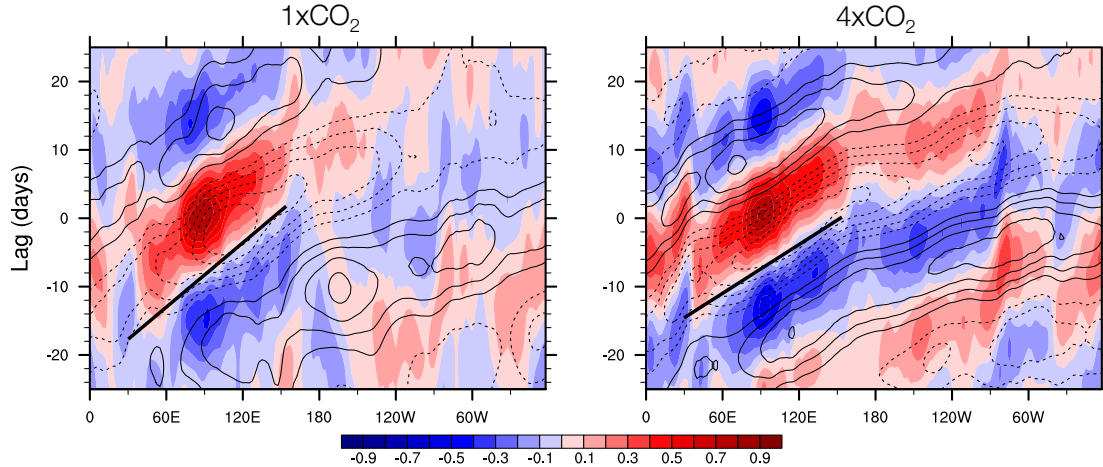
Figure 3.4.2: Correlation of intraseasonal 10°S-10°N precipitation (colors) and U850 (contours) with precipitation over base region (5°S-10°N; 80°E-100°E) for various lags. At $4\times CO_2$ the intraseasonal anomlies show greater coherency and faster eastward propagation. Black solid lines indicate speeds of 8.3m/s and 11m/s. Precipitation contour interval is 0.1, negative contours are dashed.

analysis is based on the idea that the MJO is a moisture mode, depending fundamentally on variations in atmospheric water vapor (Blade and Hartmann, 1993, Sobel and Maloney, 2012); unlike the spectrum of equatorial shallow water waves (Matsuno, 1966), a moisture mode has no equivalent in a dry atmosphere.

An important factor in moisture mode instability is the sensitivity of deep convection and precipitation to environmental humidity. In a dry environment, turbulent mixing will rapidly deplete the buoyancy of a convecting plume and inhibit precipitation (Derbyshire et al., 2004). By contrast, an anomalously moist environment will allow strong precipitation and convective heating. This dynamic likely explains the strong relationship between precipitation and column moisture seen in observations (Bretherton et al., 2004). Under the weak temperature gradient (WTG) conditions prevailing in the tropics (e.g., Sobel et al., 2001), any anomalous heating is rapidly balanced by adiabatic ascent and cooling. Advection by the induced circulation will affect the column MSE, with a net effect depending on the gross moist stability (GMS; Neelin and Held, 1987, Raymond and Fuchs, 2009), a measure of the efficiency of column MSE export. The

GMS is the small residual of dry static energy export at upper levels and moisture convergence at low levels. An effective GMS, including radiative and surface flux feedbacks, can also be defined. A moisture mode instability can occur if this effective GMS is negative; in this case, a moisture anomaly will be amplified by the combined feedbacks, setting up a self-sustaining anomaly of convection and circulation.

These ideas have led many authors to examine composite MSE budgets generated from reanalysis products (Kiranmayi and Maloney, 2011) and model output (Andersen and Kuang, 2012, Arnold et al., 2013, Maloney, 2009). Such studies have provided a general account of the flow of MSE within the MJO, although with some disagreement owing to differences in methodology and data. Points of agreement include eastward propagation driven by a combination of horizontal and vertical advection, with greater weight given to the vertical component in reanalysis products (Kiranmayi and Maloney, 2011). The horizontal component is associated with suppression (enhancement) of synoptic eddies east (west) of the MSE maximum, which otherwise constitute an MSE sink by mixing with the relatively dry subtropics (Andersen and Kuang, 2012, Maloney, 2009). In both models and observations, MSE anomalies tend to covary with longwave radiative heating anomalies due to OLR suppression by high clouds.

As in Chapter 2, we use the frozen MSE, defined as

$$h = c_p T + gz + L_v q - L_i q_i,$$

where c_p is the specific heat at constant pressure, T is temperature, g gravity, z geopotential height, L_v the latent heat of vaporization, q the water vapor mixing ratio, L_i the latent heat of freezing, and q_i the ice mixing ratio. This quantity is nearly conserved for parcels undergoing phase changes between vapor, liquid and ice; the effect of small-scale convection is simply to
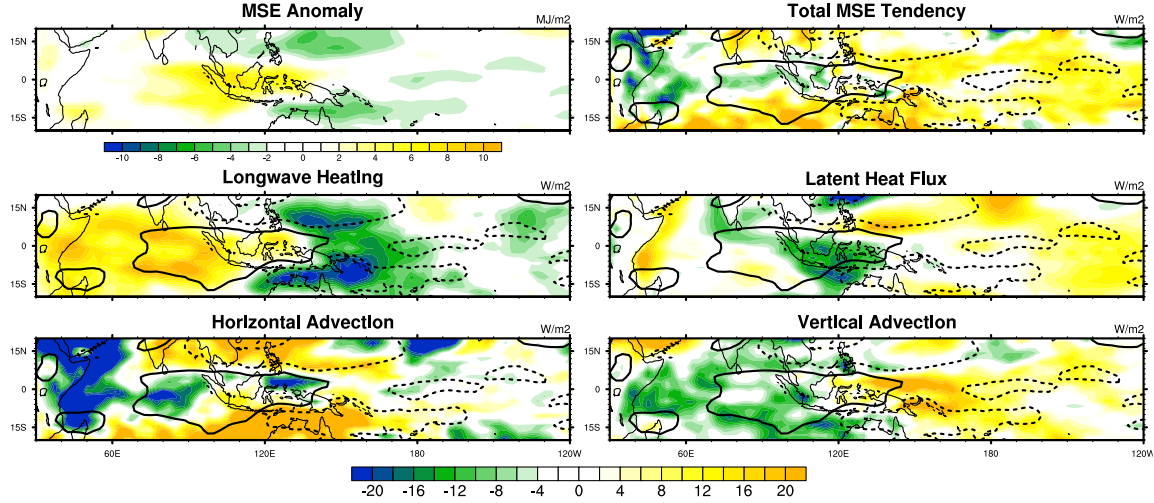
Figure 3.5.1: Composite MSE budget terms averaged over MJO phase 2 for Boreal winter at $1\times CO_2$. A positive MSE anomaly is centered over Indonesia. Contours of $\pm 2MJ/m^2$ MSE are overlaid on the tendency plots to aid interpretation. Negative contour is dashed. The phasing between MSE and tendency terms suggests the importance of longwave anomalies for maintaining the MJO, and of advection anomalies for eastward and poleward propagation.

redistribute it within a column. We use the pressure-weighted vertical integral of MSE,

$$\langle h \rangle = \frac{1}{g} \int_{p(bot)}^{p(top)} h\, dp,$$

for which the net effect of convection is nearly zero, simplifying the analysis. The vertically integrated MSE tendency,

$$\langle \partial_t h \rangle = \langle \vec{u} \cdot \nabla h \rangle + \langle \omega \cdot \partial_p h \rangle + \langle LW \rangle + \langle SW \rangle + LH + SH$$

is controlled by horizontal and vertical advection, longwave (LW) and shortwave (SW) radiative heating, and latent (LH) and sensible (SH) surface heat fluxes.

To give a sense of their spatial structure, Fig. 3.5.1 presents each composite budget term averaged over Phase 2 of MJO events during Boreal winter (Nov-Apr), when the MSE maximum

is around 110°E. A positive MSE tendency is seen over a broad region to the east and southward, with a negative tendency to the west. The MSE anomaly is noticeably in phase with the longwave heating pattern and out of phase with the advection and surface flux terms. Since the anomalous longwave heating appears to add to regions with anomalously high MSE, and remove MSE from low anomalies, it therefore serves as an energy source. Similarly, advection and surface fluxes would tend to decrease the MSE anomaly pattern, indicating an energy sink. The pattern of vertical advection suggests a strong contribution to eastward propagation, while the horizontal tendencies suggest propagation toward the poles.

The evolution of each term in time is illustrated in Fig. 3.5.2. Each term is meridionally averaged between 10°S and 10°N and shown as a function of MJO phase and longitude. Eastward propagation is clearly visible, as positive MSE anomalies develop over the Indian Ocean in Phase 6, intensify over the Maritime continent in Phase 2, and dissipate over the Pacific in Phase 5. As in Fig. 3.5.1, longwave anomalies appear largely in phase with MSE, and advective terms out of phase. Surface fluxes appear to be weaker than in Fig. 3.5.1, but this is an artifact of meridional averaging, which leads to a partial cancellation of positive and negative anomalies. This illustrates a limitation of the two-dimensional graphical analysis which is avoided in the quantitative method below.

To better estimate the importance of each budget term to amplifying or damping the MJO anomalies, we use an adapted form of the method of Andersen and Kuang (2012). Anomalies from daily climatologies are intraseasonally (20-100 day) filtered and linearly detrended at each spatial point. The fractional growth rate of the anomalous pattern of MSE $\langle h \rangle$ provided by a budget term $\langle \Phi \rangle$ is given by the projection

$$F_{\Phi} = \frac{\iint \langle h \rangle \langle \Phi \rangle dA}{\iint \langle h \rangle^2 dA},$$
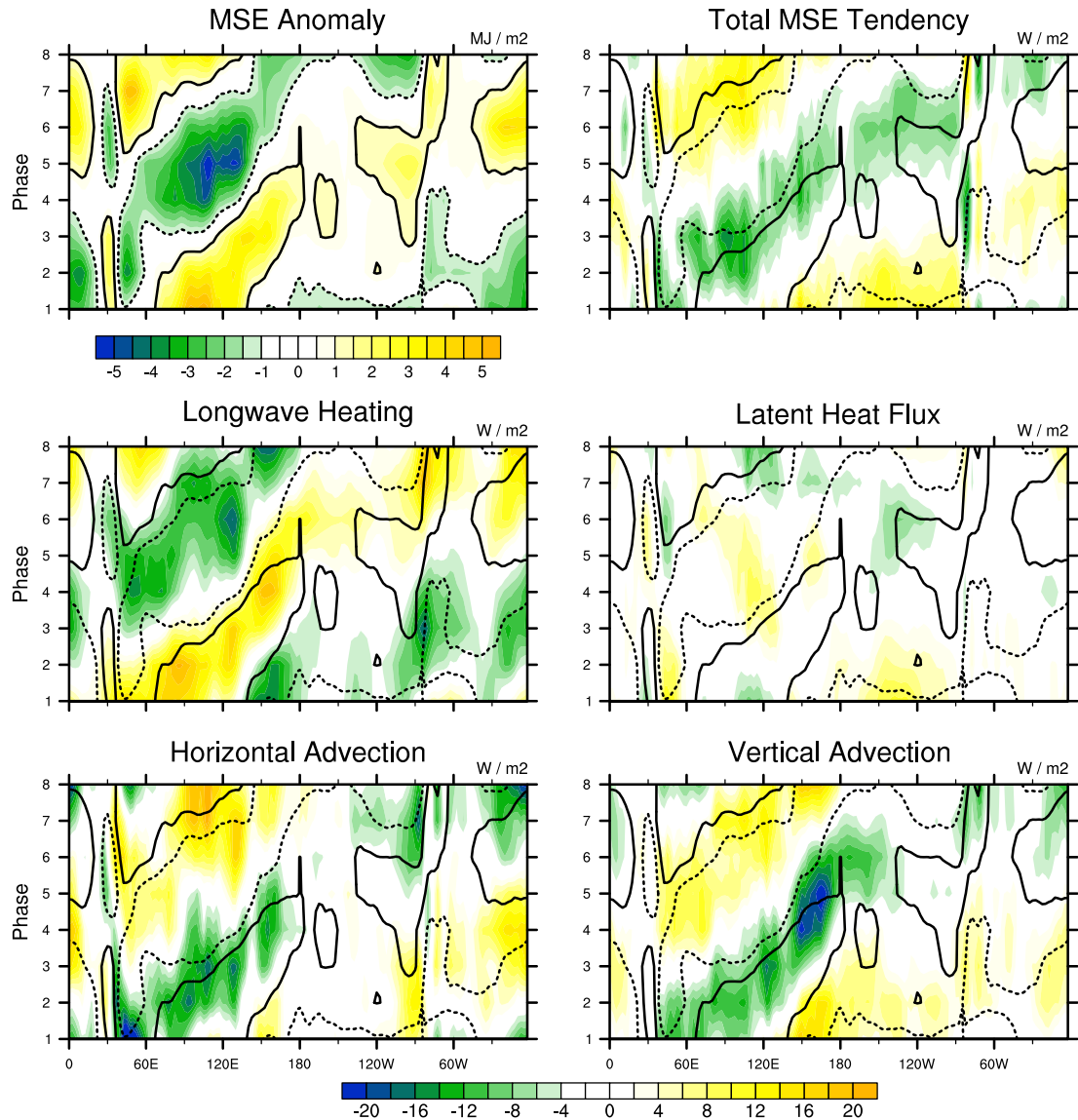
Figure 3.5.2: Composite MSE budget terms averaged 10°S-10°N for Boreal winter, plotted as a function of longitude and MJO phase. Contours of ±1MJ/m² MSE are overlaid on the tendency plots to aid interpretation. Negative contour is dashed.

where the area-weighted integral is taken over 15°S to 15°N, and 60°E to 180°E. This forcing is calculated at every six-hour interval, and an average is taken over each MJO phase during active MJO periods (index amplitude greater than one).

The result may be thought of as a budget of intraseasonal MSE variance, where the normalized
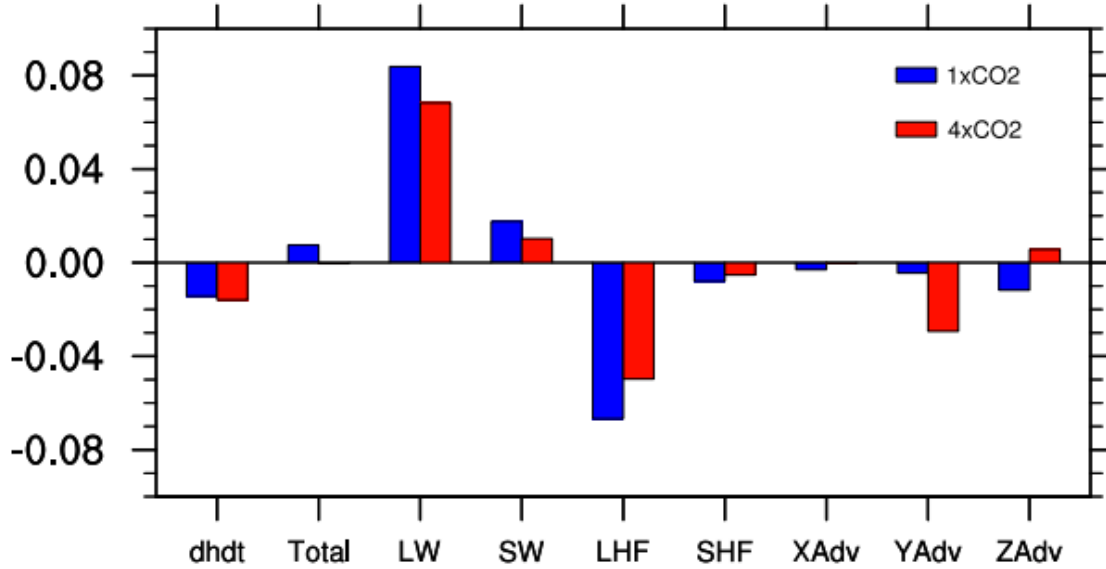
Figure 3.5.3: Estimates of the contribution F_Φ of each budget term to maintainence/dissipation of the MSE anomaly, for $1\times CO_2$ (blue) and $4\times CO_2$ (red). Visible are the dominant roles of longwave radiation (LW) and surface latent heat flux (LHF) in maintaining and dissipating the MJO, respectively. Surface fluxes (LHF) and vertical advection (ZAdv) become more positive with warming, contributing to the stronger MJO. Zonal advection (XAdv) is negligible to MJO maintainence, but meridional advection (YAdv) becomes a strong MSE sink at $4\times CO_2$.

variance tendency is equal to the sum of the forcings,

$$\frac{\frac{1}{2}\iint \partial_t \langle h\rangle^2 dA}{\iint \langle h\rangle^2 dA} = F_{Xadv} + F_{Yadv} + F_{Zadv} + F_{LW} + F_{SW} + F_{LH} + F_{SH}.$$

The budget thus quantifies the relative importance of each term, as well as changes in their importance between $1\times CO_2$ and $4\times CO_2$. If their relative sizes remained constant, this would indicate no change in the balance of processes maintaining the MJO. Given the increase in MJO activity documented in Section 3.3, we will focus our attention on terms which become more positive - more destabilizing - with warming.

The $1\times CO_2$ budget (Fig. 3.5.3) is similar to those in previous studies. The MJO in SP-CESM is principally supported by suppressed longwave cooling associated with high clouds around the MSE maximum, and damped by suppressed surface latent heat fluxes associated with enhanced

surface humidity. The role of the advective terms depends on season, with meridional advection damping the MJO in winter but amplifying it in summer, and vertical advection playing a negligible role in winter and damping the MJO in summer. Zonal advection is negligible year round.

At high CO_2 the MJO remains principally supported by longwave anomalies and damped by surface latent heat fluxes, but the effective growth/decay rates they provide per unit MSE have decreased in magnitude. Of special interest in this study are the significant positive shifts seen in latent heat flux and vertical advection. If either change were 'forced' by the warmer tropical mean state, it could potentially explain the stronger simulated MJO. However, making such a claim requires us to identify a physical mechanism linking changes in the budget to the altered mean state. In pursuit of such a mechanism, we now examine each of these terms in greater detail.

3.5.1   Vertical advection decomposition

To gain insight into the vertical advection term, we decompose the vertical velocity and vertical MSE gradient into climatology, intraseasonal (20-100 days) and residual components as in Chapter 2, such that

$$\omega = \overline{\omega} + \omega^{IS} + \omega^{r}, \qquad \frac{\partial h}{\partial p} = \overline{\frac{\partial h}{\partial p}} + \frac{\partial h^{IS}}{\partial p} + \frac{\partial h^{r}}{\partial p}.$$

The product of ω and $\partial h/\partial p$ yields nine terms, and the projection for each, averaged over all phases and seasons, is shown in Fig. 3.5.4. This shows clearly that the change in vertical advection is associated almost entirely with the intraseasonal velocity acting on the climatological MSE. A similar trend was seen in the aquaplanet simulations of the last chapter, where it was attributed to the fact that the mean MSE profile has a deeper minimum in warmer climates. This is a simple consequence of maintaining a moist adiabat over a warmer surface, with minimal change in the relative humidity profile. The MSE in a saturated atmosphere would be constant with height, but

59
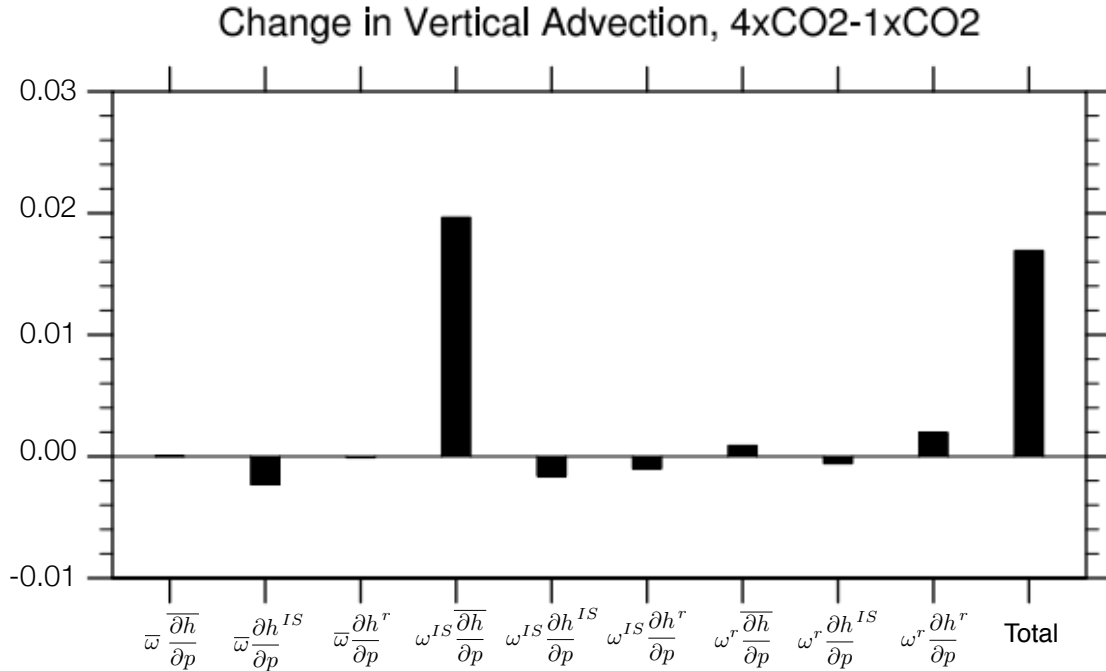
Figure 3.5.4: Change in forcing between $4\times CO_2$ and $1\times CO_2$ by different components of vertical advection. Decomposition into climatology (overbar), intraseasonal (IS) and residual (r) components indicates that change is dominated by the intraseasonal vertical velocity acting on the climatological MSE gradient.

in the real atmosphere the decrease in relative humidity away from the surface leads to a mid-tropospheric MSE deficit, and the Clausius-Clapeyron relationship implies that this deficit increases with warming. This leads to an increase in $\partial h/\partial p$ in the lower troposphere, which promotes MSE accumulation in regions of anomalous ascent, and MSE export in regions of descent. Since regions of ascent within the MJO are associated with high MSE, and descent with low MSE, the change in vertical advection provides a positive feedback on MJO growth.

This mechanism also appears to be at work in the current simulations. Vertical profiles of MSE averaged over the Indian ocean and west Pacific between $10°$S and $10°$N are shown in Fig. 3.5.5, and indicate a similar deepening of the mid-tropospheric minimum. We argue that this steepening effect again plays an important role in the simulated MJO intensification.
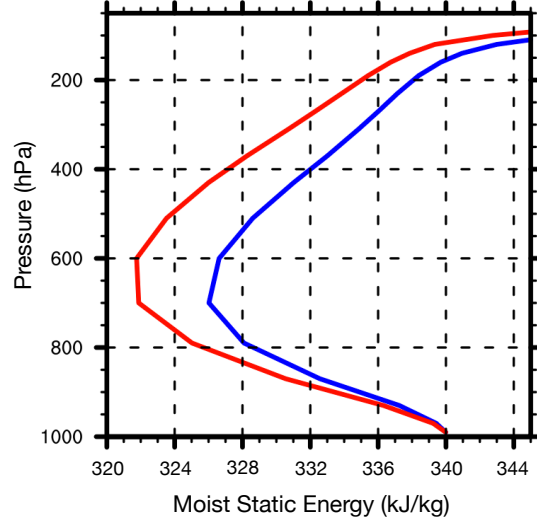
Figure 3.5.5: Vertical profiles of moist static energy (MSE) averaged over time, 10°S-10°N and 60°E to 180°E, for the $1\times CO_2$ (blue) and $4\times CO_2$ (red) simulations. The deeper minimum and larger vertical gradient of the $4\times CO_2$ profile reduces the gross moist stability. The $4\times CO_2$ profile has been shifted by 15.6kJ to match the $1\times CO_2$ profile at the surface and emphasize the difference in gradients.

3.5.2 SURFACE LATENT HEAT FLUX DECOMPOSITION

Changes in surface latent heat flux may also play a role, but it is unclear if they represent a primary cause or a positive feedback. A superficial reason for the change in F_{LH} with warming is simply that the magnitude of column MSE anomalies increases much faster than the surface flux anomalies, as explained below. This is partially offset by changes in the spatial correlation between MSE and surface flux anomalies, which decreases slightly from -0.27 to -0.3. However, this effect is not enough to overcome the significant difference in magnitude scaling.

To better understand the surface flux scaling, we perform a decomposition based on the bulk formula

$$LH = C_E \rho |v|(q_s - q) = C_E \rho |v| q_s (1 - RH).$$

The low-level stability is assumed constant, with C_E fixed at $3983\text{m}^2/\text{s}$. We define an absolute surface moisture deficit, $q_d = q_s(1 - RH)$, and then decompose the wind speed and moisture

contributions, again according to

$$q_d = \bar{q}_d + q_d^{IS} + q_d^r, \qquad |v| = |\bar{v}| + |v|^{IS} + |v|^r.$$

This analysis shows that in both the $1\times CO_2$ and $4\times CO_2$ scenarios, the latent heat flux contribution to intraseasonal MSE growth is almost entirely due to the combination of climatological surface winds and intraseasonal variation of the surface moisture deficit. A secondary decomposition of the moisture deficit term using

$$q_s = \bar{q}_s + q_s^{IS} + q_s^r \qquad 1 - RH = (1 - \overline{RH}) + RH^{IS} + RH^r$$

further indicates that the contribution from surface moisture variations is entirely associated with relative humidity, rather than changes in the saturation specific humidity. This suggests that regions of anomalously high MSE, and correspondingly high relative humidity, result in suppressed surface evaporation which damps the original anomaly.

This is in contrast with the classical WISHE mechanism for MJO growth, which relies on variations in wind speed to regulate surface evaporation (Emanuel, 1987, Neelin and Held, 1987). Instead, although we find that the fractional variations in wind speed are comparable to fractional variations in the relative humidity deficit (both roughly 10% of their mean values), the pattern of wind speed anomalies is only weakly correlated with the MJO moisture anomalies at both $1\times CO_2$ and $4\times CO_2$, and thus has little net contribution to MJO instability.

Now examining the difference between the $1\times$ and $4\times$ scenarios, we find that only two components contribute to changes in F_{LH}: $C_E\rho|v|^{IS}\bar{q}_d$ and $C_E\rho|\bar{v}|q_d^{IS}$. That is, the intraseasonal windspeed anomaly and climatological moisture deficit, and the climatological windspeed and intraseasonal moisture deficit. The former becomes slightly more negative in the $4\times CO_2$ run, while the latter is significantly more positive. The secondary decomposition again

indicates that the moisture deficit is associated with relative humidity variation.

That $C_E \rho |v|^{IS} \overline{q}_d$ is scaling faster than the column MSE anomalies seems to be mainly due to the correlation between windspeed and MSE anomalies, which drops from r=0 to r=-0.1, enough to change the term's forcing from negligible at $1\times CO_2$ to a small negative value at $4\times CO_2$. The second component, $C_E \rho |\overline{v}| q_d^{IS}$, represents the dominant contribution to total latent heat flux in both simulations, and assuming similar RH anomalies, should scale with the surface saturation specific humidity at roughly 7%/K, or roughly 30% between $1\times CO_2$ and $4\times CO_2$. This is significantly less than the roughly 60% increase in magnitude of MSE anomalies, and explains the change in forcing; the surface fluxes simply cannot "keep up" with the increasing MSE.

In summary, we find that the mechanism of MJO intensification likely works through the vertical advection term, whose forcing becomes increasingly positive with warming. This is due in part to a steepening of the mean MSE profile, which makes shallow ascent more effective at increasing the column MSE. The relative forcing provided by latent heat fluxes also becomes more positive with warming, but this appears to result from the surface fluxes being constrained to increase more slowly with SST than the column MSE anomalies. We consider this effect a positive feedback rather than a primary cause of the MJO intensification.

3.6   Discussion and Conclusions

We have examined the tropical intraseasonal variability in a pair of simulations with a super-parameterized version of the Community Earth System Model (CESM1) forced with pre-industrial ($1\times$) and quadrupled ($4\times$) CO_2. The $1\times CO_2$ simulation produces a leading mode of intraseasonal variability which closely resembles the observed Madden-Julian Oscillation (MJO). The high CO_2 simulation results in a tropical-mean warming of 4.2K, and a significant increase in the variability of moist convection on all scales.

Variance within the MJO band increases faster than the background: for example, the standard

deviation of MJO-band precipitation rises 10% per degree of warming. A simple counting method based on the Wheeler-Hendon (2004) MJO index shows this increase manifests itself through a 20-30% increase in the number of MJO events, as well as a greater magnitude of the anomalies in each event. More rapid eastward propagation is also seen.

Analysis of a composite budget of column moist static energy (MSE) indicates, similar to previous studies (Andersen and Kuang, 2012, Grodsky et al., 2009, Kiranmayi and Maloney, 2011, Lin et al., 2004, Maloney, 2009), that the MJO's principal source of MSE is the longwave radiative anomalies associated with variation in high cloud fraction. This is balanced by an energy sink from surface latent heat flux anomalies, as high surface relative humidity suppresses evaporation in regions of high MSE. Eastward propagation is primarily driven by a combination of horizontal and vertical advection, and opposed by the radiative anomalies.

Changes in the MSE budget between $1 \times CO_2$ and $4 \times CO_2$ are interpreted as changes in the MJO dynamics. We focus on vertical advection and surface latent heat fluxes, two terms whose MSE forcing becomes increasingly positive with warming, suggesting that they play some role in enhancing the MJO activity. Inferring causality from a budget analysis is complicated, but by linking changes in budget terms to robust (thermodynamic) aspects of the mean climate state we believe we have identified a plausible mechanism to explain the intensification of the MJO. A decomposition of the vertical advection term indicates that the difference between $1 \times CO_2$ and $4 \times CO_2$ is associated with the intraseasonal vertical velocity acting on the climatological mean MSE profile. This is attributed to a steepening of the MSE profile with warming, which results from maintaining a moist adiabat with minimal change in relative humidity. The increasingly destabilizing role of vertical advection is thus a robust consequence of warming, and is likely the primary cause of the enhanced MJO activity.

The change in surface flux forcing is shown to result from the more rapid scaling of column MSE anomalies. While surface flux anomalies scale with warming approximately at the rate of the saturation specific humidity (7%/K), the column MSE anomalies scale twice as fast, resulting in a

proportionately weaker negative forcing. We interpret the change in surface fluxes as a positive feedback on the MJO, following intensification by vertical advection.

This work adds to existing evidence that MJO activity may increase in response to global warming. Evidence for a weak MJO dependence on SST has been identified in observations (Hendon et al., 1999, Jones and Carvalho, 2006, Oliver and Thompson, 2012, Slingo et al., 1999), and in some numerical models (Arnold et al., 2013, Caballero and Huber, 2010, Lee, 1999). However, other models have shown negative or neutral trends with SST (Takahashi et al., 2011), or a strong dependence on the spatial pattern of warming (Maloney and Xie, 2013), so any conclusions regarding future trends should be viewed as tentative.

If MJO activity were to intensify, it could affect many other climate phenomena, including ENSO (McPhaden, 1999), tropical cyclogenesis (Hall et al., 2001, Maloney and Hartmann, 2000), monsoon systems (Lavender and Matthews, 2009, Pai et al., 2011), and global weather extremes (Jones et al., 2004). An MJO dependence on SST could also explain features from past warm climates, like the Pliocene "permanent El Nino" (Tziperman and Farrell, 2009), and may have caused superrotation during the Eocene (Caballero and Huber, 2010).

4

Abrupt Transitions to Strong Superrotation

4.1 Introduction

Persistent tropospheric superrotation has appeared in previous numerical simulations, and it is useful here to distinguish between those which develop superrotation gradually, and those with transitions which are "abrupt". In the former case, the atmosphere responds to a continuous change in external parameter (e.g., CO_2 concentration) by varying continuously from one equilibrium state to the next, while the latter case is marked by threshold behavior; a small

change in external parameter may trigger positive feedbacks and lead to a qualitatively different climatology.

In this chapter, we examine a novel positive feedback based on a resonant Rossby wave response to equatorial heating. The Rossby wave response to stationary equatorial forcing is evanescent unless the mean flow speed is equal and opposite to the free Rossby wave phase speed. This leads to a positive feedback between the waves and mean flow: as a westerly background zonal wind approaches the phase speed of the free equatorial Rossby wave, the waves will amplify. This amplification leads to stronger equatorward momentum flux, enhancing the mean westerlies and thereby further amplifying the Rossby waves. A resonance is implied, as the maximum wave amplification and mean flow acceleration occur when the westerly flow speed is exactly equal to the westward Rossby wave phase speed.

One scenario in which this feedback may be relevant is suggested by the observed annual mean pattern of geopotential height and horizontal flow at 150mb around the maritime continent, a broad region of very active convection (e.g., Fig. 4 of Dima et al. 2005). This pattern resembles the theoretical Gill (1980) solution for the upper tropospheric response to an isolated heat source, consisting of a pair of Rossby gyres to the west of the heating maximum, and a Kelvin wave response to the east. This stationary wave pattern is responsible for most of the equatorward momentum flux in the modern tropics. Both the wave pattern and its momentum transport would be expected to amplify in the presence of a westerly background wind, potentially leading to large changes in local climate, or even the establishment of superrotation on a global scale.

We demonstrate that this resonance occurs in a multi-level idealized GCM. The idealized configuration allows a straightforward comparison with shallow water theory, which confirms the physics described above. We force the idealized GCM with a zonally varying equatorial heating, and show that a superrotating jet can develop via a bifurcation as the heating rate is increased, jumping from a relatively weak to a much stronger state, with significant changes to the global circulation.

The earliest examples of abrupt transitions were seen in two-layer primitive equation models which spontaneously jumped from a conventional circulation to a superrotating one (Held and Suarez, 1978). Later studies employing equatorial eddy heating (Saravanan, 1993, Suarez and Duffy, 1992) explained this behavior in terms of a competition between extratropical and equatorial Rossby wave transport of angular momentum. In a conventional circulation, baroclinic waves generated in midlatitudes may propagate equatorward until they are absorbed near critical layers in the subtropics, where their phase speed is equal to the mean zonal flow (Randel and Held, 1991). This leads to angular momentum flux from the subtropics to midlatitudes. In these two-layer models, the conventional circulation is maintained by a negative feedback; small westerly perturbations to the equatorial winds will move critical layers equatorward, making the baroclinic wave drag more efficient and restoring the conventional easterly flow.

However, for sufficiently large westerly perturbations, the critical layers may disappear altogether, leaving the tropics effectively transparent to baroclinic waves. In this scenario, the only torque associated with baroclinic waves results from their frictional dissipation as they propagate across the tropics, and is much weaker than the torque provided by critical layer absorption. This asymmetry allows for abrupt transitions in equatorial wind strength, as the baroclinic wave feedback changes sign.

Shell and Held (2004) demonstrated that abrupt transitions and multiple equilibria are also possible in an axisymmetric framework. The positive feedback here is based on vertical advection by the Hadley cell, which brings quiescent surface air into the upper troposphere and serves as a source of drag on any superrotating flow. However, the greater angular momentum associated with a superrotating flow implies a reduced Hadley cell mass flux, which in turn implies a reduction in drag.

Williams (2003, 2006) varied the latitude of maximum baroclinity in an idealized multi-level primitive equation model, and showed that when this latitude is less than 20 degrees from the equator, a barotropic instability on the equatorward side of the eddy-driven jet leads to westerly

equatorial winds. Williams showed that the boundary between conventional and superrotating equilibria is quite narrow in parameter space, and suggests that bifurcations should be possible.

Abrupt transitions are typically not seen in "comprehensive" multi-level GCMs, which include sub-grid scale physics parameterizations, seasonal cycles, and other realistic features. However, gradual transitions to superrotation have been seen, particularly in simulations of global warming scenarios or warm paleo-climates (Caballero and Huber, 2010, Huang and Weickmann, 2001). In some cases, these are accompanied by an increase in tropical intra-seasonal variability (Caballero and Huber, 2010, Lee, 1999), which may serve as an equatorial wave source. If the superrotation in these cases is indeed driven by changes in organized convection, then it may depend on particular parameterization schemes, a poorly constrained component of atmospheric models. Note that the positive feedbacks discussed above - namely, those based on Rossby wave critical layers, the Hadley circulation, and barotropic instability - are all determined solely by the primitive equations, and should thus be present to some degree in every GCM. The scarcity of abrupt transitions in comprehensive models suggests either a lack of the sustained westerly perturbations required to activate positive feedbacks, a stronger role for negative feedbacks, or an atmosphere dominated by "stochastic" variability which prevents a sustained feedback loop.

This chapter is organized as follows: The model and forcing are described in section 4.2. In section 4.3 we present idealized simulations illustrating the feedback and bifurcation. A quantitative explanation of the feedback based on linear shallow water theory is offered in section 4.4. Section 4.5 explores the feedback in more realistic climates, and our conclusions and further discussion are in section 4.6.

4.2 Model description and experimental setup

We use the NCAR Community Atmosphere Model (CAM) in the idealized configuration based on Held and Suarez (1994). This consists of the dry primitive equations for an ideal gas on a

rotating sphere, and neglects topography, moisture, and radiative and convective processes. The effect of the omitted processes on the model climate is crudely represented by a Newtonian relaxation of temperatures toward a prescribed "radiative-convective" equilibrium profile. Surface momentum exchange in the boundary layer is represented by a linear Rayleigh friction. Numerical stability is maintained with a weak horizontal biharmonic diffusion, and vertical diffusion is neglected. This idealized configuration is advantageous in that it captures the fundamental physics of the large-scale circulation while remaining simple enough that model output may be easily compared with theory.

We modify the prescribed temperature profile to allow for a reduced - and in some cases, eliminated - meridional temperature gradient, which serves to modulate the strength of the Hadley cell and the eddies associated with midlatitude baroclinicity. This simplification reveals the feedback and bifurcation that are the focus of this paper. The modified equilibrium temperature profile is of the form

$$
T_{eq}(p, \phi) = \left[315K - \Delta T \sin^2 \phi - (\Delta\theta)_z log\left(\frac{p}{p_0}\right) \cos^2 \phi \right]
$$
$$
\cdot \left(\frac{p}{p_0}\right)^{R/c_p}
$$

where the equator-to-pole temperature difference ΔT is varied from $0K$ to $60K$, and the $\cos^2 \phi$ factor is replaced by 1 in the case $\Delta T = 0K$ in order to eliminate the temperature gradient associated with a meridionally varying lapse rate. Similar to studies in the Matsuno/Gill framework (e.g., Gill, 1980), setting $\Delta T = 0$K isolates the equatorial dynamics and simplifies the analysis, but it should be kept in mind that this also removes dominant processes from the equatorial momentum balance, in particular the momentum transport by midlatitude waves and the seasonal cross-equatorial flow of the Hadley circulation which maintains the easterlies near the present tropical tropopause (Lee, 1999). We address this issue in section 4.5.

The lack of vertical diffusion is a serious deficiency when studying an equatorial jet, as this leaves only resolved, large-scale advection to represent the small-scale convective plumes and broad subsidence which make up vertical motion in the real tropical troposphere. It has been noted by Held (1999a) that superrotation can generally be eliminated in idealized models by increasing the vertical diffusion. Although cumulus friction (convective momentum transport) is a secondary term in the present-day equatorial momentum balance, this is partly a result of weak vertical shear, and it may play a larger role in a superrotating scenario. Gravity wave drag is also known to play a small but significant role (Huang et al., 1999), but is not included in the model.

The simulations presented here are based on the CAM3.1 spectral dynamical core with T42 truncation (a horizontal resolution of roughly $2.8^o \times 2.8^o$) and 26 vertical levels. Some simulations were repeated with the same dynamical core at a higher resolution (T85, roughly $1.4^o \times 1.4^o$), or with the CAM4.0 Finite Volume dynamical core, at $1.9^o \times 2.5^o$ resolution. We found no significant differences with either higher resolution or the alternative dynamical core.

4.2.1 PRESCRIBED EDDY FORCING

The appearance of superrotation in many numerical studies has coincided with increases in organized tropical convection (Caballero and Huber, 2010, Lee, 1999), and it is generally accepted that large-scale variations in convective heating can act as a Rossby wave source and lead to equatorward momentum fluxes. To mimic the effect of latent heating in our dry model, we add a diabatic term to the model's thermodynamic tendency equation, of the form

$$Q_{CAM} = Q_0 \cos\left(\frac{k(\lambda - c_f t)}{2\pi a}\right) \exp\left(-\frac{\phi^2}{\Delta\phi^2}\right) \sin\left(\frac{p - p_t}{p_b - p_t}\right)$$

similar to that used by Kraucunas and Hartmann (2005). Here p_t is pressure at the tropopause, p_b at the top of the boundary layer, k the zonal wavenumber, and c_f a zonal translation speed. The heating is Gaussian in latitude, sinusoidal in longitude, approximates the first baroclinic mode in

71

the vertical, and is limited to the free troposphere, between $p_b = 800mb$ and $p_t = 200mb$. Here we use $\Delta\phi = 10^o$, roughly the equatorial deformation radius, and vary Q_0, k and c_f.

For reference, the zonally varying component of the time-mean tropical latent heating can be approximated by $k = 2$, $\Delta\phi = 15^o$, $c = 0$m/s and $Q_0 = 1$K/day (Schumacher et al., 2004). The Madden Julian Oscillation (MJO) might be thought of as $k = 1$, $\Delta\phi = 15^o$, $c_f = 5$m/s and $Q_0 = 2$K/day (Kiladis et al., 2005). The simulations presented here employ heating rates well within these bounds, never exceeding $Q_0 = 0.9$K/day. However, the forcing could be more effective than its magnitude suggests because it is so spatially coherent and continuous in time.

We found that the transition to superrotation could be triggered with nearly any zonally asymmetric heating. Related simulations with a prescribed momentum forcing also produced a bifurcation. The results thus appear insensitive to the form of equatorial forcing, so long as some equatorial wave source is present.

4.3 RESONANCE AND ABRUPT TRANSITION WITH NO MERIDIONAL TEMPERATURE GRADIENT

Although the resonance and bifurcation analyzed below occur for a wide range of parameters, we begin with the case in which they are most clearly illustrated, with the pole-to-equator temperature difference ΔT set to zero. The model is initialized from rest and allowed to reach equilibrium with wavenumber two heating of constant $Q_0 = 0.1$K/day. The direct response to the heating takes three forms: a first baroclinic structure in the equatorial troposphere, similar to the classical Matsuno-Gill response (Gill, 1980); a weak vertically propagating signal, confined to the tropics; and weak poleward propagating Rossby waves with an equivalent barotropic structure. This is consistent with the work of Salby and Garcia (1987), who studied the response to equatorial heating in detail.

The zonal mean climate is shown in Fig. 4.3.1. Horizontal eddy momentum fluxes associated
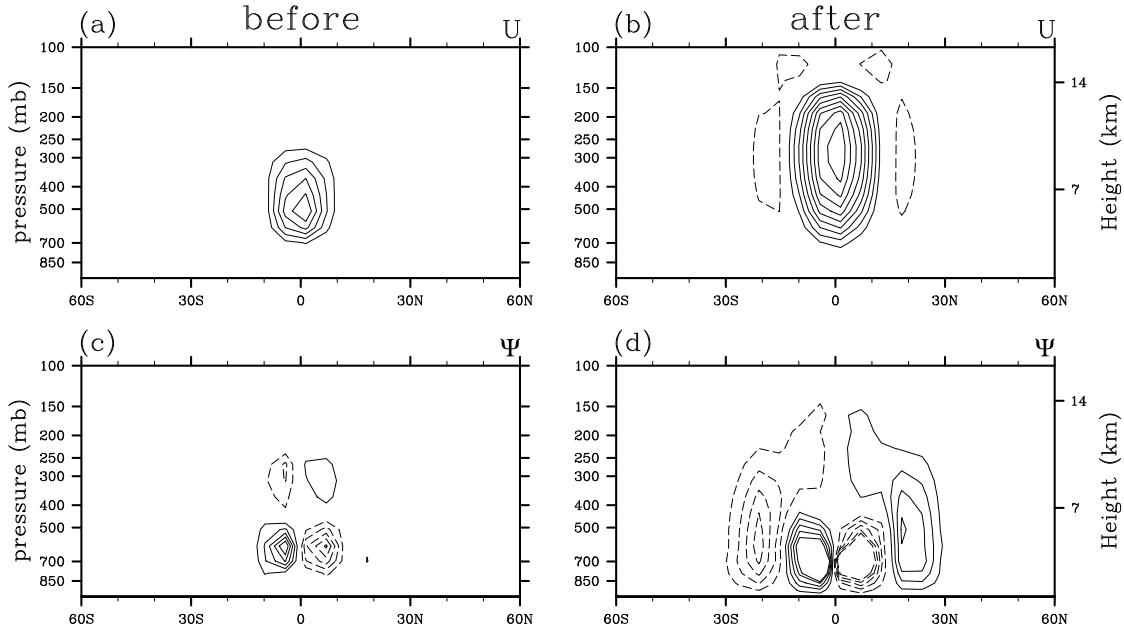
Figure 4.3.1: Zonally averaged quantities, before (a,c) and after (b,d) the bifurcation, for simulations without meridional temperature gradient, $\Delta T = 0$K. All fields are in equilibrium with $Q_0 = 0.3$K/day, demonstrating multiple equilibria for this limited case. Contour intervals are (a) 1m/s, (b) 2.5m/s, (c,d) 0.5Sv. Negative contours are dashed.

with the first baroclinic structure produce a weak westerly jet in the middle troposphere, and a small indirect circulation forms above the boundary layer in order to maintain thermal wind balance.

The heating is increased in increments of 0.1K/day, and the model allowed to equilibrate at each level, until $Q_0 = 0.4$K/day. A time series of zonal velocity and horizontal eddy momentum convergence, $-\overline{\partial_y(u'v')}$, illustrates this sequence in Fig. 4.3.2. For $Q_0 < 0.4$K/day, the eddy momentum convergence scales approximately as Q_0^2, as one might expect in a linear regime where u' and v' both scale with Q_0.

After Q_0 is increased to 0.4K/day, the eddy momentum convergence initially rises according to the Q_0^2 scaling, but then the system appears to pass a threshold; the momentum convergence increases rapidly, peaking at 0.21m/s/day before settling around 0.13m/s/day, significantly
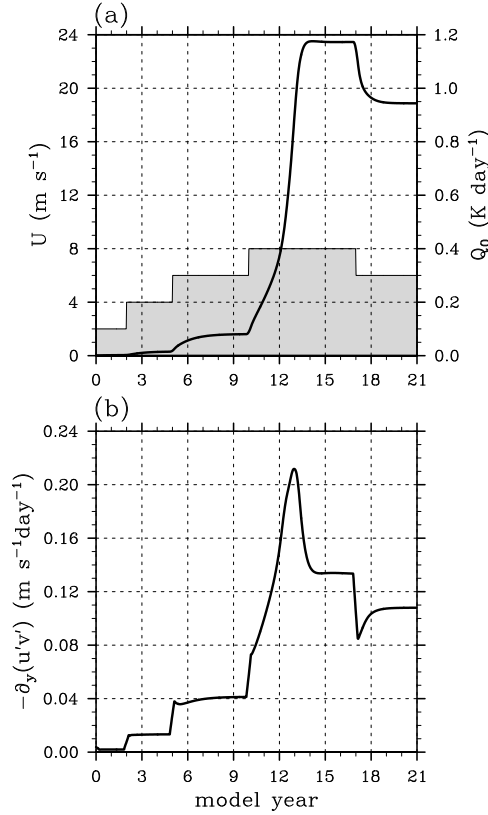
Figure 4.3.2: Bifurcation of the equatorial jet in a simulation with no meridional temperature gradient, $\Delta T = 0$K. Time series of zonal mean quantities averaged between 200mb and 400mb for the case of wavenumber $k = 2$ heating with stepwise increasing heating rate Q_0. (a) zonal velocity and heating rate Q_0, (b) equatorial eddy momentum convergence $-\partial_y(u'v')$.

higher than the 0.07m/s/day expected from the Q_0^2 scaling. This increase is not balanced by other dominant terms in the momentum equation, particularly diffusion and vertical eddy fluxes, and the result is a jump in the mean zonal velocity from 2m/s to near 24m/s. We show below that this sharp increase in eddy momentum flux and zonal velocity is due to a bifurcation in the system, driven by interaction between the mean flow and the eddy field.

The system also shows moderate hysteresis: if the heating rate is subsequently reduced to 0.3K/day, the eddy momentum convergence drops sharply to near its pre-bifurcation level, and the jet begins to decelerate. However, as the jet velocity decreases, the eddy momentum convergence begins to rise again, and the jet equilibrates at 19m/s, much higher than the

equilibrium velocity for $Q_0 = 0.3\text{K/day}$ before the bifurcation. This behavior suggests a resonance-like feedback, with a resonant velocity between the pre- and post-bifurcation velocities, 2m/s and 19m/s.

In the time series in Fig. 4.3.2, we define the jet velocity as the zonal-mean zonal wind averaged from $5°\text{S}$ to $5°\text{N}$ and between 200mb and 400mb, though the bifurcation is also evident when averaging the full vertical column. This pressure interval is chosen because it is the region of greatest eddy activity, and we show below that it is the local (upper tropospheric) winds that are most relevant to the eddy-driven feedback. Prior to the bifurcation, both eddy kinetic energy and the meridional eddy momentum flux are concentrated in two altitude ranges: above the heating between 200mb and 400mb, and below the heating between 600mb and 700mb. The post-bifurcation increase in these quantities is centered entirely in the upper troposphere. Note that this vertical shift across the bifurcation is also reflected in the vertical structure of the jet (see Fig. 4.3.1a,b).

4.4 Analysis of the wave-mean flow feedback and transition to super-rotation

We can gain some insight into the mechanism of the transition to superrotation by considering analytical solutions to the forced shallow water equations on an equatorial beta plane. Though the simulated jet has a nearly Gaussian meridional structure, explicitly taking this structure into account renders analytical solutions intractable. Instead we consider the response to forcing in the presence of a uniform background flow U, following the approach of Phlips and Gill (1987), in the hope that this approximation still captures the essential mechanism of the bifurcation. Showman and Polvani (2010) point out that the classical Matsuno-Gill system will not lead to superrotation due to an artificial cancellation between the horizontal and vertical eddy fluxes. This results from neglect of the momentum transport by the imposed mass/heat source. When

this term is accounted for, vertical fluxes become smaller than horizontal fluxes and superrotation will develop. Consistent with their corrected model, the vertical eddy fluxes in our simulations are generally of opposite sign to the horizontal fluxes and smaller in magnitude. However, the temporal evolution of the vertical fluxes during transitions to superrotation varies significantly between simulations, so for simplicity we will focus on the horizontal fluxes. We believe this is consistent with our use of the shallow water framework only to gain physical intuition into the wave-mean flow feedback.

We begin with the non-dimensional steady-state shallow water equations,

$$U\partial_x u - \beta y v = -\partial_x \phi - \kappa \nabla^4 u$$

$$U\partial_x v + \beta y u = -\partial_y \phi - \kappa \nabla^4 v$$

$$U\partial_x \phi + \partial_x u + \partial_y \phi = Q_{SW}$$

The ∇^4 hyperdiffusion term is included because of its appearance in CAM, and for a given simulation may be approximated as $-\epsilon u$, where $\epsilon = \kappa(k^2 + l^2)$, k is the heating zonal wavenumber and l is assumed to be 2π over the deformation radius. This value is very near the coefficient of Rayleigh friction used in classical Matsuno-Gill studies (e.g., Gill, 1980).

We assume a heat forcing given by

$$Q_{SW} = Q_0 \cos(kx) \exp(-y^2/L_d^2),$$

which excites only the Kelvin and $n = 1$ planetary wave modes, and allows a simple Fourier transform in longitude, greatly simplifying the problem. The meridional structure can be found in terms of Hermite polynomials, following the well-known methodology outlined by Gill and others. Details for this case can be found in the Appendix.

The gravity wave phase speed on which the solutions depend is a function of the equivalent

depth, h, which we estimate from CAM in two ways. First, by direct calculation $h = \frac{1}{g}(N/m)^2$, where N is the buoyancy frequency and m the vertical wavenumber of the imposed heating ($\pi/12$km). This method is complicated by the fact that h varies significantly over the relevant altitudes: between 50m and 100m for most of the troposphere, but from 100m to 600m in the interval 150mb to 250mb, where the eddy momentum flux is largest. The second estimate is taken from the wavenumber-frequency power spectrum of 200mb zonal wind for a simulation without equatorial forcing, which shows enhanced power in bands associated with linear Kelvin and Rossby waves. After correcting for the doppler shift by the mean zonal wind (estimated to be -3m/s), the observed Kelvin wave speeds are most consistent with an equivalent depth of 150m, while the $n = 1$ Rossby wave speeds are consistent with slightly larger depths of 150m-250m. In the comparisons discussed below, we have used an equivalent depth $h = 250$m, which produces the best agreement between CAM and the shallow water theory. We acknowledge the somewhat arbitrary nature of this choice as a weak point in our analysis, but we believe it is consistent with the facts outlined above and permits a compelling simple model of the GCM behavior.

The non-dimensional solution for the Kelvin mode is given by

$$
\begin{aligned}
u &= \frac{-Q_0\gamma}{6\epsilon(1+\gamma^2)} \left[\gamma\cos(kx) + \sin(kx)\right](y^2 - 3)\exp(-y^2/4) \\
\phi &= \frac{-Q_0\gamma}{6\epsilon(1+\gamma^2)} \left[\gamma\cos(kx) + \sin(kx)\right](y^2 - 3)\exp(-y^2/4)
\end{aligned}
$$

while the Rossby mode is given by

$$u = \frac{-Q_0\gamma}{6\epsilon(1+\gamma^2)} \left[\gamma\cos(kx) + \sin(kx)\right](y^2 - 3)\exp(-y^2/4)$$

$$v = \left[\frac{-4Q_0\gamma}{3\epsilon(1+\gamma^2)}\left((Uk + \gamma\epsilon)\cos(kx) + (\epsilon - Uk\gamma)\sin(kx)\right) + Q_0\cos(kx)\right]$$

$$\cdot\, y \cdot \exp(-y^2/4)$$

$$\phi = \frac{-Q_0\gamma}{6\epsilon(1+\gamma^2)} \left[\gamma\cos(kx) + \sin(kx)\right](y^2 + 1)\exp(-y^2/4)$$

where $\gamma = \frac{\epsilon}{k(c+U)}$, c being the appropriate wave phase speed (Kelvin or Rossby).

The significance of the solutions is best illustrated by the inviscid case ($\epsilon = 0$), in which the wave fields become proportional to $1/(c + U)$. This implies a singularity when $U = -c$, directly analogous to the theoretical singularity involving topographic Rossby waves in the presence of a mean westerly wind (c.f. Holton, 2004). As $U \to -c_R$, the free Rossby mode becomes stationary relative to the heating, and will amplify without bound in the absence of friction. In the presence of friction solutions reach a maximum amplitude when $U = -c_R$, which may be physically interpreted as a resonance.

The combined Kelvin and Rossby analytic solutions for $k = 2$ are shown in Fig. 4.4.1 for $U = 2$m/s and $U = 19$m/s, along with 200mb eddy fields from CAM, at $t = 9$yr and $t = 20$yr of the simulation shown in Fig. 4.3.2. The CAM eddy fields are defined as instantaneous departures from the zonal mean, e.g., $u' = u - \bar{u}$. The agreement between CAM and theory appears to be quite good; the theory captures qualitative shifts in phase tilt and amplitude across the bifurcation.

The analytical solutions can be used to calculate a zonal-mean eddy momentum flux convergence on the equator, $-\partial_y\overline{(u'v')}|_{eqtr}$ as a function of U. The resulting dependence is shown in Fig. 4.4.2a, along with a similar curve derived from a CAM simulation in which Q_0 was increased slowly and continuously (0.03K/day/year), to allow the zonal wind and eddy fluxes to

78
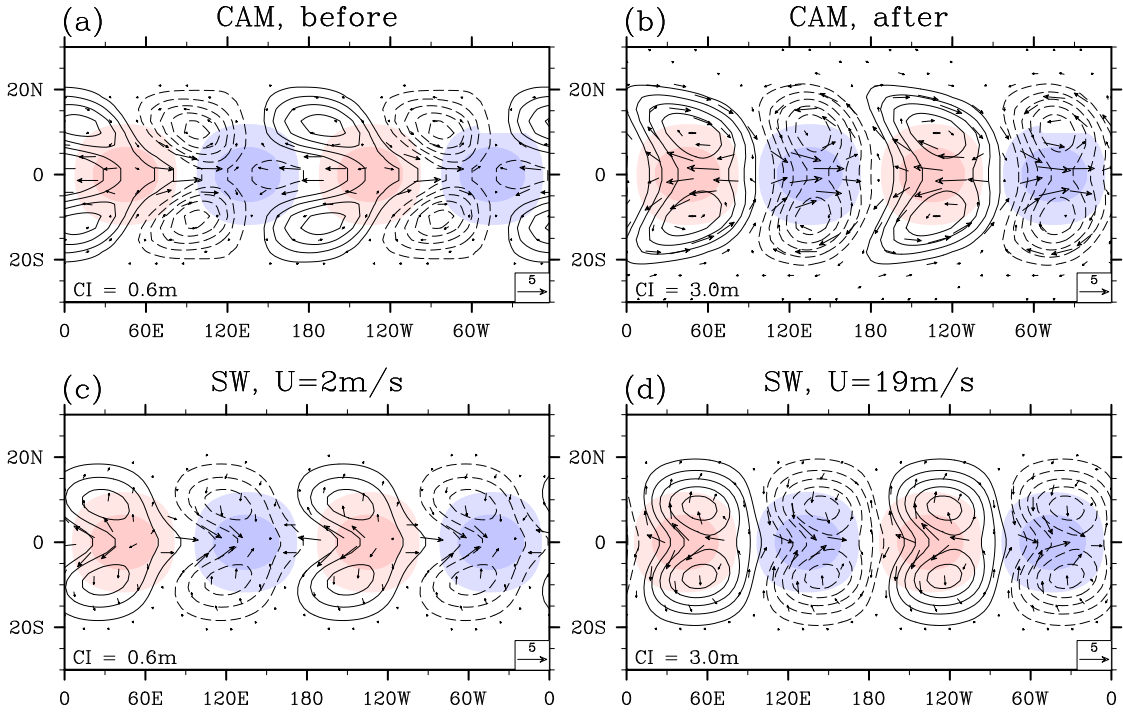
Figure 4.4.1: Equilibrium eddy response before (a,c) and after (b,d) the bifurcation, with $Q_0 = 0.3$K/day. CAM 200mb fields are shown in (a,b) and shallow water solutions in (c,d). Contours indicate geopotential height, shading indicates heating (Q_{CAM} and Q_{SW}), and vectors the wind field. Contour interval is 0.6m before transition and 3m after, showing that the wave amplitude is increased by a factor of five.

be in quasi-equilibrium with the forcing. Both curves indicate a maximum eddy flux when the mean flow nears 16m/s, the phase speed of the n=1 Rossby wave for the equivalent depth of 250m used here. Although there is a relative phase shift between u and v associated with changes in U, most of the change in momentum transport is due to the amplification of the wave fields.

To evaluate the accuracy with which this theory reproduces the behavior seen in CAM, we run a series of simulations in which we vary the zonal wavenumber k and the forcing propagation speed c_f. If the resonance is indeed determined by the zonal wind speed relative to the forcing, then we expect the velocity at which momentum convergence is maximized to be $U_e = -c_R + c_f$. Figure 4.4.2b summarizes the velocity of maximum eddy momentum convergence in this set of CAM simulations. The simulated U is plotted against the expected
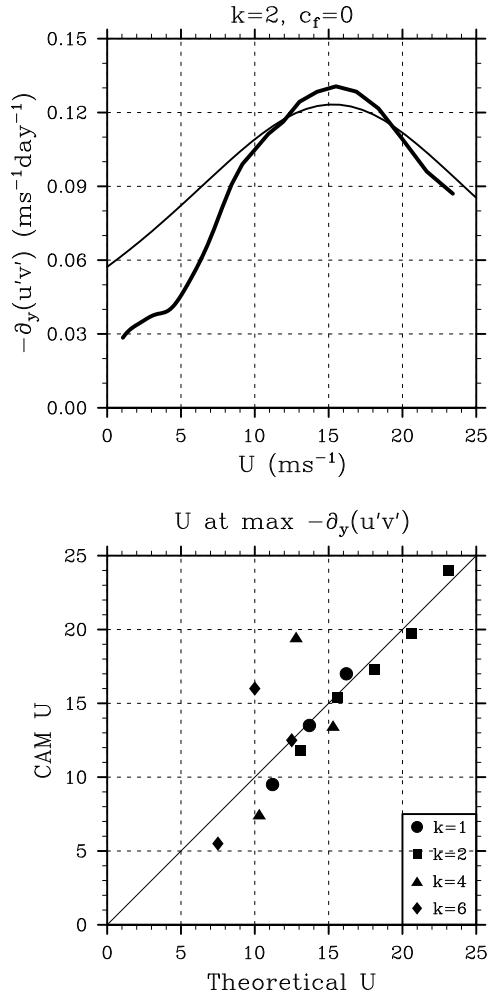
Figure 4.4.2: (top) Equatorial momentum flux convergence as a function of jet velocity, in CAM with $\Delta T = 0$K (bold line) and in shallow water theory (thin line). (bottom) Instantaneous jet velocity in CAM simulations at time of maximum eddy momentum flux, plotted against the resonant velocity predicted by shallow water theory for the appropriate k and c_f.

value of U_e, with the Rossby wave phase speed given by

$$c_R = \frac{-\beta}{k^2 + (2n+1)\beta/\sqrt{gH}}$$

where we use $n = 1$ and $H = 250$m for all cases. The agreement with theory is again quite good, leading us to conclude that the shallow water theory does indeed capture the essential mechanism

of the feedback and bifurcation. Two points, from $k = 4$, $c_f = 0$ and $k = 6$, $c_f = 0$, lie more

than two standard deviations from the theoretical curve. It is unclear why, since they are both

near the center of the model parameter space sampled here, but we take a moment to speculate

why the theoretical solution might break down. First, the jet produced in the GCM is not

uniform, but roughly Gaussian in meridional and vertical extent. The resulting shear may distort

the wave field, and also modify the background vorticity gradient on which the waves propagate.

This, in turn, leads to a change in the free wave velocity and shifts the resonance location. Second,

the Phlips and Gill solution assumes small U and k, but the dropped terms are not strictly

negligible in all cases shown here. Finally, the eddy velocities can exceed $5m/s$, suggesting that

nonlinearities may be significant.

4.5 THE RESONANCE IN MORE REALISTIC BACKGROUND STATES

Having demonstrated that the resonance occurs in the idealized configuration with $\Delta T = 0$K,

we now turn to more Earth-like simulations with the pole-to-equator temperature difference set

to $\Delta T = 40$K. While this meridional temperature gradient is still less than on the modern earth,

these simulations now include an equinoctal Hadley circulation and significant baroclinic eddy

activity. Our goal is to demonstrate that the wave resonance and bifurcation are possible in a fully

three dimensional atmosphere with a vigorous basic state circulation. The zonal-mean zonal wind

and meridional mass streamfunction from a run without asymmetric heating are shown in

Fig. 4.5.1, along with climatological fields from the National Center for Environmental Prediction

(NCEP) Reanalysis product (Kalnay and Coauthors, 1996). The strength of the midlatitude jets

is comparable between our idealized CAM simulation and the Reanalysis, although the jets in our

idealized CAM simulation extend to unrealistic altitudes. This is an artifact of the prescribed

restoring temperature being uniform in the stratosphere. The Hadley cells are also significantly

weaker in CAM, due to the lack of off-equatorial peak heating associated with a seasonal cycle,
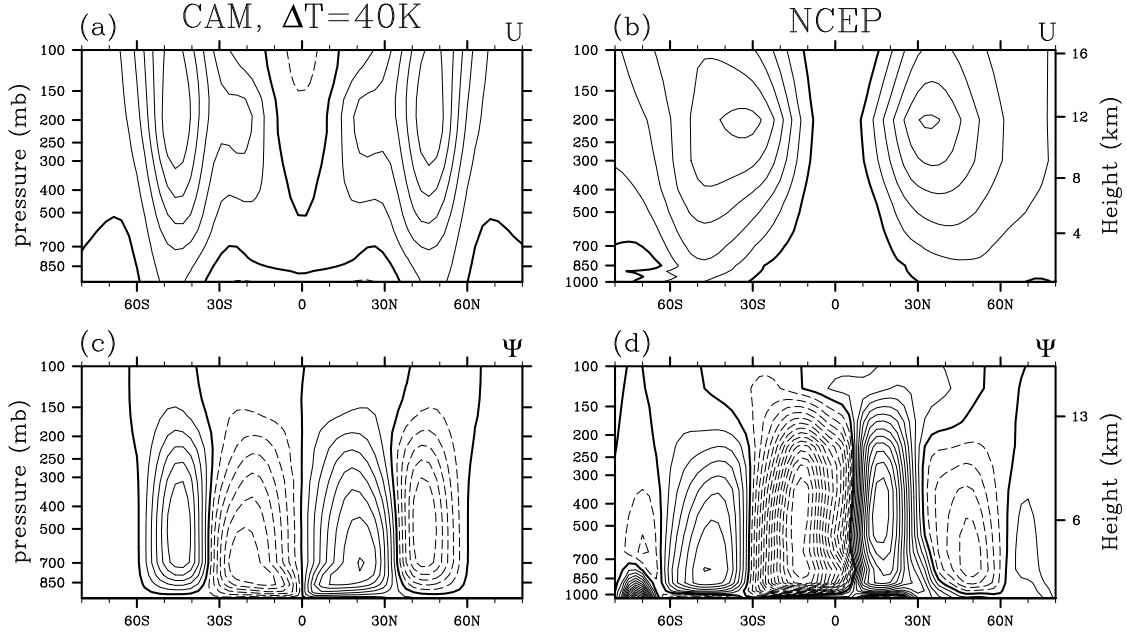
Figure 4.5.1: Zonal- and time-mean fields from CAM $\Delta T = 40$K unforced simulation (a,c) and NCEP Reanalysis (b,d). Contour intervals are 5m/s for zonal wind (a,b), and $10\mathrm{e}9$ kg/s for the meridional overturning streamfunction (c,d).

which is known to strengthen the Winter hemisphere cell (e.g., Lindzen and Hou, 1988). Despite these deficiencies, we believe this basic state is sufficiently realistic to make our point.

On top of this basic state we prescribe an equatorial heating crudely based on the MJO, with $k = 1$ and $c_f = 5$m/s. The results are qualitatively similar if we use the stationary heating with $k = 2$ from Section 3, but a lower wavenumber proves to be advantageous, as we show in the next section.

We increase the heating rate in the stepwise manner described in Section 4.3, generating the time-series shown in Fig. 4.5.2. For $Q_0 < 0.5$K/day there is little change in the upper tropospheric winds, which remain easterly, even at values of Q_0 which triggered strong superrotation when ΔT was set to 0K. The eddy momentum convergence rises according to the Q_0^2 scaling, but is weaker than in the $\Delta T = 0$K case, presumably because the equatorial eddy
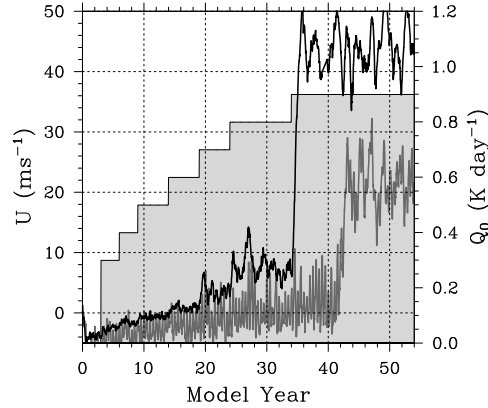
Figure 4.5.2: Forcing amplitude Q_0 (piecewise-constant grey shading) and equatorial jet velocity (black line) for a CAM simulation with a more realistic pole-to-equator temperature difference of Δ T = 40K. Jet velocity for a simulation including a seasonal cycle (grey line) with the same forcing Q_0.

field is modified by baroclinic wave propagation in a way which reduces the velocity covariance.

At $Q_0 = 0.6$K/day the mean wind become weakly westerly, which in theory allows the existence of non-evanescent free wave modes. This prediction is consistent with the observed eddy momentum convergence, which begins to rise faster than Q_0^2. Increases in the eddy momentum convergence are still relatively small, however, and are quickly offset by a negative feedback involving momentum advection by the mean circulation, $-\overline{\omega}\partial_p\overline{u}$, which prevents a runaway acceleration. This trend continues until $Q_0 = 0.9$K/day (compared with $Q_0 = 0.4$K/day for $\Delta T = 0$K), at which point the jet jumps from roughly 8m/s to 50m/s, and eventually settles to a statistical equilibrium of 45m/s (compared with 24m/s for $\Delta T = 0$K).

This transition differs from the $\Delta T = 0$K case in two respects. The equatorial jet is more than twice as strong here, arguably due to the larger heating rate at the point of bifurcation. That the transition occurs at a higher value of Q_0 (0.9K instead of 0.4K) would suggest a factor of five ($0.9^2/0.4^2$) difference in momentum convergence. Of course, the resonant behavior renders this scaling inadequate across the bifurcation, and other terms in the momentum equation may compensate the equatorial eddy flux, but it is obvious that a larger Q_0 can account for much of the difference in post-bifurcation jet velocity.
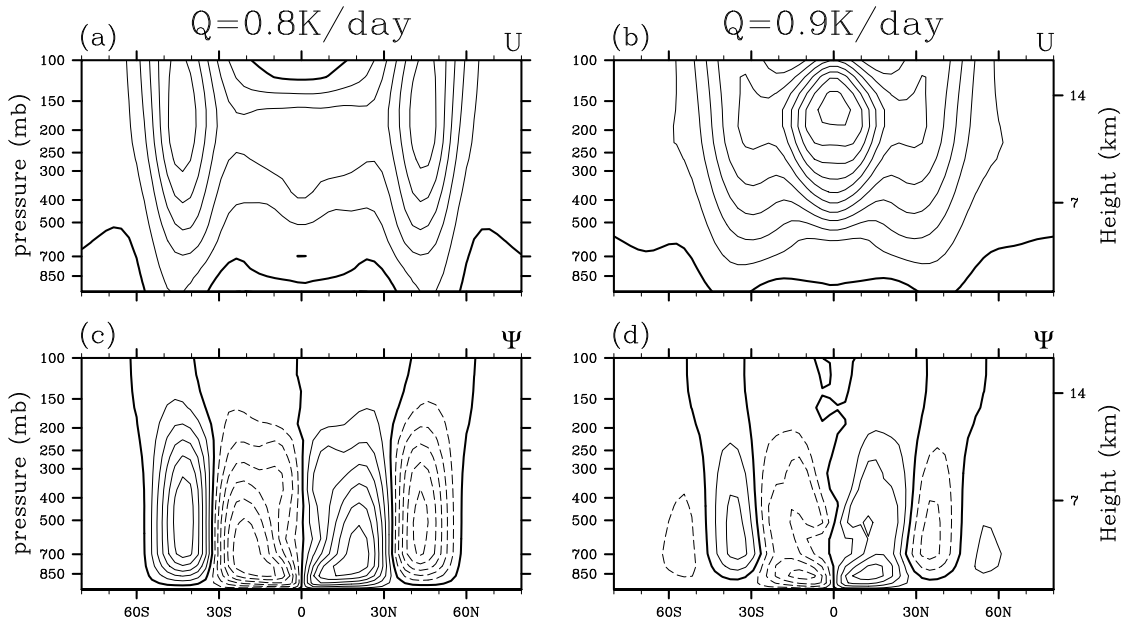
Figure 4.5.3: Zonal- and time-mean fields for CAM simulations with equatorial heat forcing. Contours as in Fig. 4.5.1.

The transition here also differs qualitatively from the $\Delta T = 0$K case. The post-bifurcation circulation with $\Delta T = 0$K looked like an approximately Gaussian jet superimposed on the basic state, but we find here that the background flow is significantly modified. The Hadley cell largely collapses after the transition (Fig. 4.5.3d), consistent with changes seen with $\Delta T = 0$K. More interesting is the equatorward shift of the midlatitude jets, such that they merge with the equatorial jet and produce an atmosphere with only westerly winds above 600mb. This behavior was also noted by Held (1999a) in a similar model with equatorial forcing.

4.5.1 Comparing feedbacks

Although the results presented above are reminiscent of the bifurcation in Section 4.3, it would be premature to conclude that the $\Delta T = 40$K bifurcation is driven by the same wave resonance. The presence of a Hadley circulation and midlatitude jets brings into play the additional feedbacks identified in previous studies. In this section we hope to evaluate their relative

contributions, if any, to the transition to superrotation.

We first consider the feedback involving midlatitude wave propagation identified by Saravanan (1993). Because the forced equatorial eddies have a wavenumber $k = 1$, while midlatitude baroclinic eddy energy peaks at $k = 5$ and is largely negligible for $k < 3$, we expect the momentum fluxes attributable to each source to be separable in wavenumber space. To this end, we calculate the momentum flux co-spectrum,

$$\Phi = \frac{1}{N_x} \hat{u}'^* \hat{v}'$$

where $\hat{A}$ designates the Fourier transform of A in longitude, $\hat{A}^*$ is the complex conjugate of $\hat{A}$, and A' is the instantaneous zonal anomaly, $A' = A - \overline{A}$. The 200mb zonal-mean co-spectrum averaged over the final two years of the $Q_0 = 0.8$K/day segment, just prior to the bifurcation, is shown in Fig. 4.5.4. The equatorial eddy $(k = 1)$ and midlatitude eddy $(k > 3)$ momentum fluxes are clearly separable, and play very different roles in the momentum balance; the former is associated with strong momentum convergence on the equator, and the latter with a weak divergence, as expected.

Having established their separability, we now evaluate their relative fluxes during three segments of the simulation, with $Q_0 = 0$K/day, $Q_0 = 0.8$K/day, and $Q_0 = 0.9$K/day, corresponding to the unforced state, and just before and just after the bifurcation, respectively. The zonal-mean eddy momentum flux associated with $k = 1$ is shown in the left panels of Fig. 4.5.5, as a function of latitude and pressure. The flux is negligible without forcing, but with $Q_0 = 0.8$K/day a strong convergence is evident over the equator. In the right panels we show the total flux associated with higher wavenumbers, i.e. the summation of the co-spectrum over $k > 1$, $\sum_{k=2}^{N_k} \Phi$. The basic state shows a weak divergence over the tropics, and very little change when asymmetric heating is applied, indicating an absence of the wave feedbacks hypothesized by
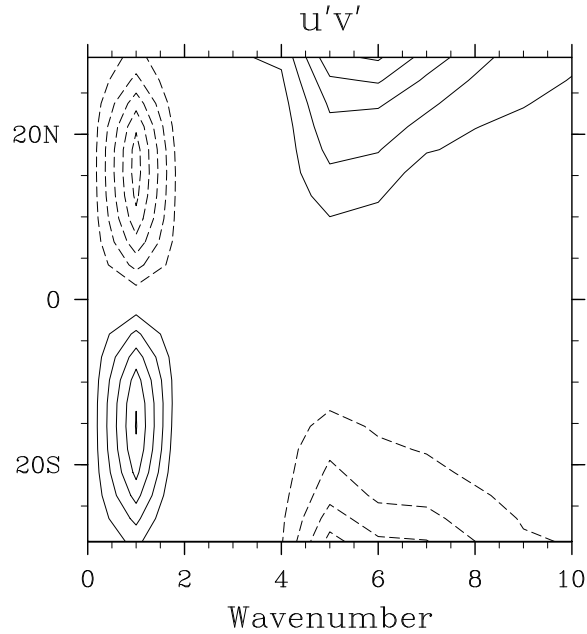
Figure 4.5.4: Zonal- and time-mean eddy momentum flux co-spectrum, integrated 100mb to 400mb. The separation of equatorial eddies ($k = 1$, with flux toward equator) and midlatitude eddies ($k > 3$, with flux away from equator) is clearly visible.

Saravanan (1993). Note from Fig. 4.5.3 that the upper tropospheric equatorial zonal wind is already above 10m/s when $Q_0 = 0.8$K/day, and the critical latitudes predicted by linear barotropic wave theory should have moved equatorward or disappeared for many wavenumbers. That the midlatitude momentum fluxes do not respond to changes in the background zonal wind suggests a failure of the linear theory.

After the bifurcation, there is an obvious amplification of the $k = 1$ momentum flux convergence, while the $k > 1$ fluxes become less spatially coherent (Fig. 4.5.5f), with equatorial convergence on some levels and divergence on others. We note that after the bifurcation, the Rayleigh criterion for barotropic instability (that the absolute vorticity $\beta - U_{yy}$ change sign in the domain) is satisfied on the poleward flanks of the equatorial jet, around 15N/S and between 200 and 400mb. This suggests that the disorganized character of the $k > 1$ momentum flux may be due to waves generated locally by barotropic instability interacting with the baroclinic waves
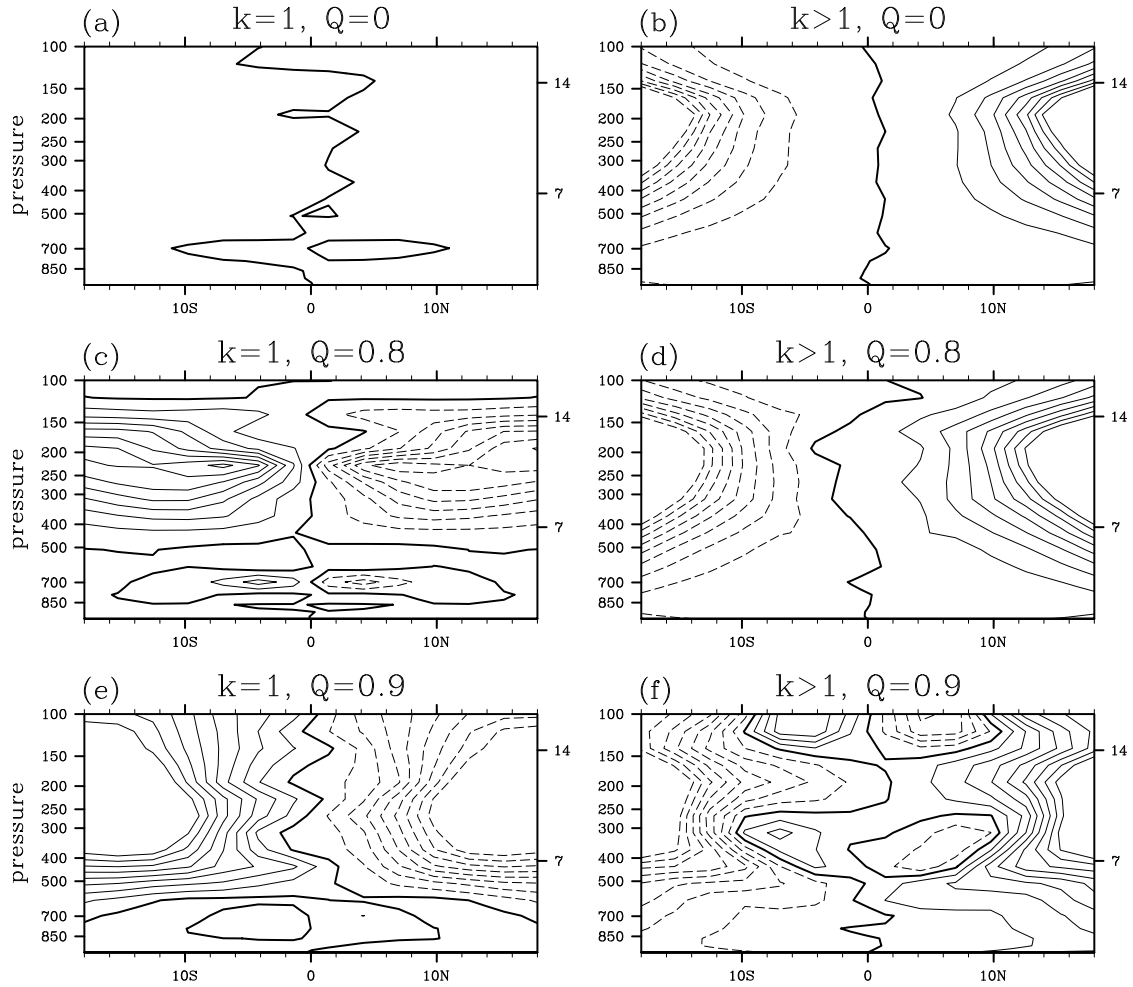
Figure 4.5.5: Zonal-mean eddy momentum flux separated by zonal wavenumber, with $k = 1$ in the left panels and integrations over $k > 1$ in the right panels. The heating rate Q_0 is indicated for each time period.

propagating from midlatitudes.

We also consider the axisymmetric feedback proposed by Shell and Held (2004), which requires a reduction in vertical advection of quiescent surface air into the jet by the Hadley cell, as the equatorial winds accelerate. We use the vertical convergence of momentum, $-\overline{\omega}\partial_p\overline{u}$, integrated over the jet, for comparison with their term R, which represents mass exchange between the the upper and lower layers. The mean vertical convergence in this simulation is significantly smaller than the eddy flux convergences, and almost certainly plays a minor role in

the bifurcation.

4.5.2 Including a seasonal cycle

The largest source of easterly acceleration in the equatorial upper troposphere comes from the cross-equatorial flow associated with the solstitial Hadley circulation (Lee, 1999), and we would be remiss not to address it here. To understand its effect on the bifurcation, we add a simple seasonal cycle to the thermodynamic tendency, of the form

$$
\begin{aligned}
Q_s =&(1.0) \exp\left[-\left(\frac{\phi - 7.5^o \sin 2\pi t/\tau}{7.5^o}\right)^2\right] \\
&- (0.5) \exp\left[-\left(\frac{\phi - 15^o \sin 2\pi t/\tau}{15^o}\right)^2\right] \\
&p_t < p < p_s
\end{aligned}
$$

where ϕ is latitude, t is time, and τ is one year. This is a time-dependent version of the stationary off-equatorial heating prescribed by Kraucunas and Hartmann (2005). In addition, we multiply Q_s by the factor $\Delta T/60\mathrm{K}$, such that the seasonal cycle scales with the meridional temperature gradient. The T_s term leads to a vigorous winter hemisphere Hadley cell, and more realistic equatorial momentum balance (not shown).

We again apply the $k = 1$ equatorial heating from the last section, generating the time-series in Fig. 4.5.2. A bifurcation is clearly visible at year 42, as the mean equatorial winds between 100-400mb abruptly increase by $20\mathrm{m/s}$ and become strongly superrotating. This occurs at the same heating rate required for the equinoctal case ($Q_0 = 0.9\mathrm{K/day}$), but the jump in velocity is about $10\mathrm{m/s}$ smaller. Interestingly, the model does not immediately transition to strong superrotation when Q_0 is set to $0.9\mathrm{K/day}$, but maintains weak westerlies for eight years before making a seemingly spontaneous jump. A 20-year extension of the simulation (not shown) in which the jet remains near $20\mathrm{m/s}$ suggests that the upper equilibrium is fully stable. Similar

extensions in other simulations with various ΔT and Q_0 suggest that most values of Q_0 have a single stable fixed point, either strongly superrotating or not. The only exceptions occur at the boundary of the two regimes, where seemingly spontaneous jumps are possible, though they only go one way (the strongly superrotating equilibrium is always stable). We attribute this apparent spontaneity to the "stochastic" influence of midlatitude eddies, which leads to variation in both the eddy momentum flux out of the tropics and the coherence of the forced equatorial wave. This provides temporary windows of opportunity for positive feedbacks to take hold and produce strong superrotation. The seasonal cycle would add a periodic component to this variability, but cannot itself account for a multi-year delay.

4.6 Summary

Superrotation in several atmospheric GCMs has coincided with significant increases in organized tropical convection with gross characteristics resembling the Madden Julian Oscillation (Caballero and Huber, 2010, Lee, 1999). Organized convection is believed to excite atmospheric Rossby waves which lead to equatorward momentum fluxes and drive the atmosphere towards a superrotating state. These increases in convective variability often occur in simulations of warmer climates, which suggests the possibility of superrotation during past warm intervals (Tziperman and Farrell, 2009) or a future dominated by anthropogenic warming (Held, 1999a, Pierrehumbert, 2000).

In this study, we mimicked the dynamical effects of organized tropical convection by applying a zonally varying equatorial heating in a GCM with simplified physics, resulting in eddy momentum fluxes from the subtropics to the equator. A comparison with analytic shallow water theory suggests that the equatorward momentum flux is produced by the tilted planetary-scale Rossby gyres of the classical Matsuno-Gill response to imposed heating. This is similar to the numerical shallow water results of Showman and Polvani (2010), as well as studies of transient

superrotation associated with the MJO (e.g., Biello et al., 2007, Moncrieff, 2004). We find that with sufficient equatorial forcing, these fluxes produce a strong westerly flow between 200mb and 400mb; in essence, a "superrotating jet".

The strength of the superrotating jet was shown to depend nonlinearly on the equatorial heating rate, Q_0, and the pole-to-equator temperature difference, ΔT. When $\Delta T = 0$, both the Hadley circulation and baroclinic wave activity are eliminated. In this simplified regime, the superrotating jet undergoes a bifurcation as Q_0 passes from 0.3K/day to 0.4K/day, abruptly transitioning from a relatively weak $(< 5\text{m/s})$ to a strong (24m/s) state. If the heating rate is reduced after the bifurcation occurs, the jet remains in the strong state. This hysteresis is moderate, however; multiple equilibria are found only for $0.25 < Q_0 < 0.35\text{K/day}$.

Distinct weak and strong states are still observed with a non-zero meridional temperature gradient, although the presence of a vigorous meridional circulation and baroclinic wave activity increases the value of Q_0 required to force a transition. For example, with $\Delta T = 40\text{K}$, the jet will jump from 10m/s to 40m/s as Q_0 passes from 0.8K/day to 0.9K/day. Hysteresis is no longer seen, likely due to the increased variability in the simulated atmosphere. The transition to superrotation in this case includes a nearly 50% reduction in the Hadley circulation strength, and an equatorward shift of the midlatitude jets, which effectively merge with the equatorial jet. Shifts in surface winds associated with the midlatitude jets may help explain sea surface temperature anomalies at midlatitude upwelling sites in the early Pliocene (Tziperman and Farrell, 2009).

Kraucunas and Hartmann (2005) suggested that the sensitivity to equatorial eddy heating in idealized models is an artifact of their lack of a seasonal cycle, especially the solstitial seasons of the Hadley circulation, which induce a strong easterly acceleration in the equatorial upper troposphere. We address this deficiency by adding an idealized seasonal forcing in the form of a zonally uniform heating tendency which migrates between hemispheres with an annual period. This produces a Hadley circulation dominated by the "winter" hemisphere, and results in much stronger equatorial easterlies, consistent with observations (Lee, 1999). Despite this change, a

bifurcation and transition to a strongly superrotating jet are still seen for $\Delta T = 40$K, although the "strong" state westerlies are weaker than in the equinoctial simulation.

The nonlinear response to heating reported here is reminiscent of behavior seen in two-layer primitive equation models (Saravanan, 1993, Suarez and Duffy, 1992), and the axisymmetric model of (Shell and Held, 2004), but the mechanism responsible for our bifurcation is a novel one, and has not previously appeared in the superrotation literature. Instead of feedbacks involving mid-latitude waves or the Hadley circulation, our bifurcation is driven by a resonance phenomenon. As the zonal wind relative to the imposed heating nears the phase speed of the $n = 1$ free equatorial Rossby wave, the heating projects onto the free wave mode and the overall Rossby wave response amplifies. The amplified wave produces additional momentum flux from the subtropics to the equator, which ultimately allows a higher equilibrium jet velocity. This resonance is directly analogous to the theoretical singularity involving free topographic Rossby waves in the presence of a westerly mean wind (c.f. Holton, 2004).

The difference in mechanism helps explain why the hysteresis in our model is so much weaker than that reported by Saravanan (1993). The superrotating state in that model was supported by transient eddies - rather than the forced stationary eddies in our simulations - which allowed the superrotation to persist for some time after heating was removed. We also find little evidence for the mid-latitude wave feedbacks found in Saravanan's simulations. This is consistent with previous studies using multi-level GCMs (e.g., Hoskins et al., 1999) and analytical work which indicates that Rossby wave breaking and its associated momentum convergence may depend on the vertical shear. Panetta et al. (1987) found that in the two-layer quasi-geostrophic framework, Rossby waves propagating into a region where $U - c$ is positive in the upper layer and negative in the lower layer will not exhibit critical layer absorption when the vertical shear exceeds a critical value. This perfect transparency does not seem to occur in the continuous case (Held, 1999a), which suggests that the dramatic positive feedback found in two-layer models may be an artifact of their vertical resolution. This feedback was invoked by Mitchell and Vallis (2010) to explain

transitions to superrotation in multi-level simulations of generic terrestrial planets, but it is unclear why the wave feedback would occur in that context but not here.

The resonance presented here joins other feedbacks (Shell and Held, 2004, Williams, 2003) which provide plausible mechanisms for abrupt, qualitative changes in the large-scale flow of three dimensional atmospheres. Simulations most similar to the modern Earth, with $\Delta T = 60\text{K}$ (not shown), indicate a much more linear response to changes in Q_0 and little evidence of abrupt transition, suggesting that a resonance-driven bifurcation may be limited to past or potential future climates in which ΔT or the seasonal cycle are reduced.

<div style="text-align: right">

5

</div>

Superrotation in the Pliocene

5.1   INTRODUCTION

THE EARLY PLIOCENE WARM PERIOD from 3 to 5.3Ma was the most recent geologic era
significantly warmer than present, and is considered a potential analogue for the next century of
anthropogenic global warming (Chandler et al., 1994, Dowsett et al., 1996, Dowsett and
Robinson, 2009a), although see Lunt et al. (2009). Pliocene atmospheric CO_2 concentrations are
estimated to have been 400 ± 50ppm (Pagani et al., 2010, Raymo et al., 1996, Seki et al., 2010),

and a combination of proxy records and modeling studies put the Pliocene global average surface temperature about 3°C warmer than present, with greater warming toward the poles (Chandler et al., 1994, Dowsett et al., 2011). The Greenland and West Antarctic ice sheets were greatly diminished and possibly absent for much of this period (Pollard and DeConto, 2009, Scherer, 1991), and global sea level was up to 25m higher than today (Dowsett and Cronin, 1990).

Some of the most interesting features of the early Pliocene are the significant warm anomalies found in ocean upwelling zones around the globe. Multiple proxies for sea surface temperature (SST) indicate anomalies of roughly $+3°C$ in the eastern equatorial Pacific, while west Pacific SSTs were similar to modern values, suggesting that mean conditions in the Pliocene equatorial Pacific resembled a modern El Niño event (Chaisson, 1995, Ravelo et al., 2006, Wara et al., 2005). In addition, all four upwelling zones associated with major eastern boundary currents - California, Humboldt, Canary and Benguela - show anomalies of $+3°C$ to $+9°C$ relative to today (Dekens et al., 2007, Herbert and Schuffert, 1998, Marlow et al., 2000). In the present era, both mid-latitude and equatorial upwelling zones are associated with high biological productivity and relatively cool temperatures, maintained by the raising of cold, nutrient-enriched deep waters by local patterns of wind stress. Upwelling sites have tremendous economic and ecological importance, supporting a large fraction of ocean biodiversity and roughly 20% of the world's fish catch (Pauly and Christensen, 1995). There is thus great interest in understanding how upwelling systems will respond to a warmer world.

Although the upwelling zone warm anomalies are supported by multiple sediment cores and proxy types, there is no consensus on a physical explanation, and they are not reproduced in Pliocene simulations by the latest generation of coupled climate models (Haywood et al., 2012). One hypothesis suggests that the global thermocline was deeper during the Pliocene. While wind-driven upwelling could still occur, the upwelled water would be drawn from a warmer source, resulting in warm anomalies at the surface. Several factors which might lead to a deeper thermocline have been identified, including an enhanced freshwater flux in high latitudes

(Fedorov et al., 2004), increased mixing in the subtropics driven by significantly enhanced hurricane activity (Fedorov et al., 2010), a reduced meridional temperature gradient (Boccaletti et al., 2004), and changes in extratropical cloud cover (Barreiro and Philander, 2008).

Another possibility is that the surface winds near upwelling zones were weaker or shifted relative to their modern positions. The warm anomalies are then explained as a reduction in upwelling intensity, rather than a change in source water temperature. Tziperman and Farrell (2009) suggested that changes in the intensity or organization of tropical convection could increase the equatorial Rossby wave source. As Rossby waves propagate out of the tropics, they would transport zonal momentum equatorward, weaken the easterlies there, and could push the tropics toward a more El Niño-like mean state.

This explanation suggests that the same waves could, upon being absorbed in the mid-latitudes, alter the surface winds around coastal upwelling zones and thereby explain the mid-latitude warm anomalies as well(Tziperman and Farrell, 2009). However, tests in which an MJO-like forcing was added to the NCAR atmospheric GCM (not shown) suggest that these wave impacts are inconsistent across the four mid-latitude sites and generally too weak to explain the warm anomalies.

Another possibility is that mid-latitude wind stress could differ due to the large-scale temperature field. The modern upwelling-favorable winds around these sites are associated with the subtropical high pressure zones that result from a combination of the subsiding branch of the zonal-mean Hadley circulation, and the seasonal land-sea temperature contrast. This results in a land-sea pressure gradient which drives the along-shore geostrophic winds responsible for upwelling. Marlow et al. (2000) proposed that changes in upwelling intensity evident in a sediment core from the Benguela Current could be associated with a gradual increase in the trade winds due to the increase in pole-to-equator temperature gradient between the Pliocene and present.

Changes in sub-surface water properties and changes in surface wind stress are not mutually

exclusive, and may both play a role in controlling the SST recorded by planktic species. In this chapter we ask what global reconstructions of Pliocene SST imply about the surface winds around midlatitude coastal sites, and by extension, the level of upwelling they support.

We use a high resolution global atmosphere model driven by two different Pliocene SST reconstructions to quantify changes in wind stress between Pliocene and modern conditions. Ocean temperatures are specified, while land temperatures are allowed to evolve according to local energy balance. We find that both SST reconstructions result in reduced upwelling-favorable winds around all four mid-latitude upwelling sites, suggesting that the significant coastal warm anomalies could be a secondary consequence of whatever sets the large-scale low-gradient SST pattern.

5.2   MODEL DESCRIPTION AND EXPERIMENTAL SETUP

We use the NCAR Community Atmosphere Model (CAM) version 5.1.1 (Neale and CoAuthors, 2010). This is the atmospheric component of the Community Earth System Model (CESM) version 1.0.4, run with prescribed sea surface temperatures and sea ice, $0.9° \times 1.25°$ horizontal resolution and 30 levels in the vertical.

We present three simulations, each based on a different SST distribution (Fig. 5.2.1). The control case uses a modern (1982-2001) SST climatology from the Hadley Centre Sea Ice and Sea Surface Temperature (HadISST) dataset (Rayner et al., 2003). The first Pliocene case employs the PRISM 3D dataset, a reconstruction of global ocean temperatures during the mid-Piacenzian (3.29Ma to 2.97Ma) developed by the USGS Pliocene Reconstruction Interpretation and Synoptic Mapping (PRISM) group (Dowsett and Robinson, 2009a). This is the latest version of an ongoing effort to provide lower boundary conditions for Pliocene modeling studies, incorporating all available proxy records (Dowsett et al., 1996, Dowsett and Poore, 1991, Dowsett and Robinson, 2009b). The PRISM 3D SST reconstruction incorporates geochemical (alkenone
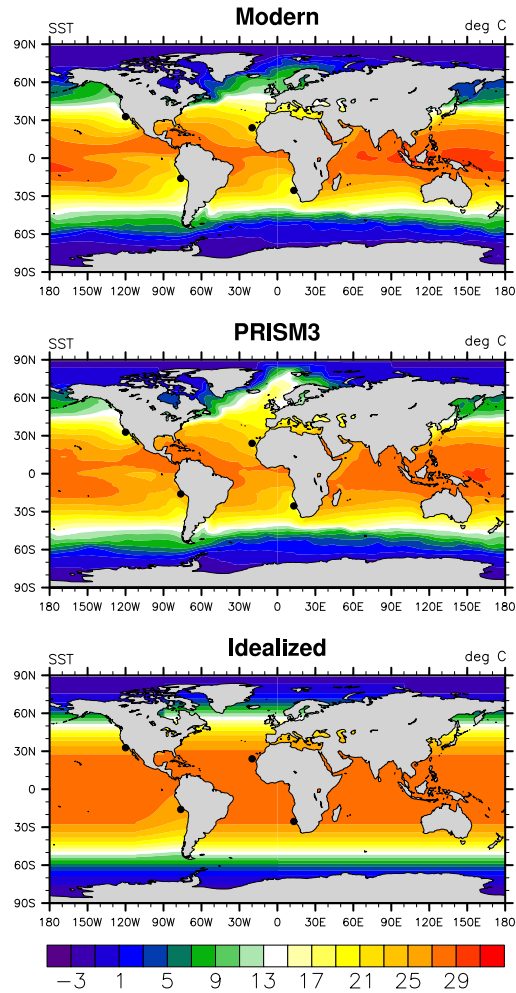
Figure 5.2.1: The annual mean sea surface temperatures used in the Modern (top), PRISM3 (mid) and Idealized (bot) simulations.

and Mg/Ca) and foraminiferal assemblage data from 86 sediment core sites.

The second Pliocene case uses an idealized SST reconstruction by Brierley et al. (2009), in which the Tropical warm pool is extended poleward and zonal gradients are nearly eliminated. This is based on geochemical proxy data from an earlier period (4-4.2Ma) than the PRISM interval, sometimes called the Pliocene Thermal Optimum. Differences from modern SSTs are larger than in the PRISM3 reconstruction, and this case may be viewed as an extreme limit of the general low-gradient conditions which seem to have prevailed throughout the Pliocene.

Sea ice in the Modern case is taken from the HadISST climatology, and in the PRISM case is taken from the PRISM 3D reconstruction. In the idealized case, sea ice fraction is specified at 90% wherever the SST drops below freezing. Though this is simplistic, we have found in separate tests that our results are relatively insensitive to the sea ice distribution. Atmospheric CO_2 concentrations were set to 355ppm in the Modern case, and 405ppm in the Pliocene simulations as recommended by the Pliocene Model Intercomparison Project (Haywood et al., 2010) and consistent with recent estimates (Pagani et al., 2010, Seki et al., 2010). Orbital parameters, methane, ozone and atmospheric aerosols are set to modern (1981-2001) climatological values in all simulations. Each simulation is run for 11 years, and the first year is discarded to allow for model equilibration. Monthly values from the remaining 10 years are used for the calculations shown here.

These core simulations use modern topography and land surface characteristics, but we also examine the sensitivity of coastal winds to Pliocene topography and land surface types. Topography can force surface winds mechanically, and land surface properties can influence surface albedo and heat and moisture fluxes, which in turn affect the land-sea temperature contrast, pressure gradient and wind field. We conduct two tests, one with Pliocene topography, and another with both Pliocene topography and surface biome and land-ice. Both tests are run with PRISM3 SST, and the Pliocene topography and surface properties are taken from the PRISM3D dataset.

5.3 The effect of Pliocene SST

We focus on surface winds around sediment core sites in the four major eastern boundary currents: Ocean Drilling Project (ODP) site 1014 in the California Current System; ODP site 958 in the Canary Current near Western Sahara; ODP site 1237 in the Humboldt Current off the Peruvian coast; and ODP site 1084 in the Benguela Current near present day Namibia. The site

locations are indicated in Figs. 5.2.1 and 2.

Wind-driven upwelling can be broken into two processes. Near the coast, wind stress parallel to the coastline drives a net transport of surface water away from the coast, which is replaced by cool water from below. From linear theory, the coastal upwelling mass flux is approximated by

$$M_{coast} = \frac{\tau_{as}}{f} \tag{5.1}$$

where τ_{as} is the alongshore component of the surface wind stress. This yields the upwelled mass for a given length of coastline, with units of $[\text{kg/s/m}]$. Away from the coast, upwelling can still occur due to wind stress curl. This is described by

$$M_{curl} = \frac{1}{f} \nabla \times \vec{\tau} \tag{5.2}$$

which has units of $[\text{kg/s/m}^2]$, essentially the upwelling rate per unit area. Integrating M_{curl} along a distance perpendicular to the coastline yields a quantity directly comparable to M_{coast}, and the relative importance of along-shore stress and offshore curl may be assessed.

Surface wind stress around upwelling sites in the CAM5 Modern case is first validated against a climatology of QuikSCAT satellite observations from 2000 to 2009, on a $0.25° \times 0.25°$ grid. The observed wind velocities are converted to surface stresses using a bulk formula. In general the agreement is quite good (Fig. 5.3.1). The model is able to reproduce the large-scale pattern and seasonality of wind stress and wind stress curl at all four locations, although the magnitude is generally overestimated. Other model deficiencies include a failure to capture the small-scale wind stress curl associated with the Canary Islands, and a wider-than-observed strip of positive curl along each coastline, likely due to the coarser model resolution.

The PRISM3 SST results in modest reductions in wind stress curl and alongshore stress within the Canary and Benguela Current regions, with somewhat smaller reductions within the
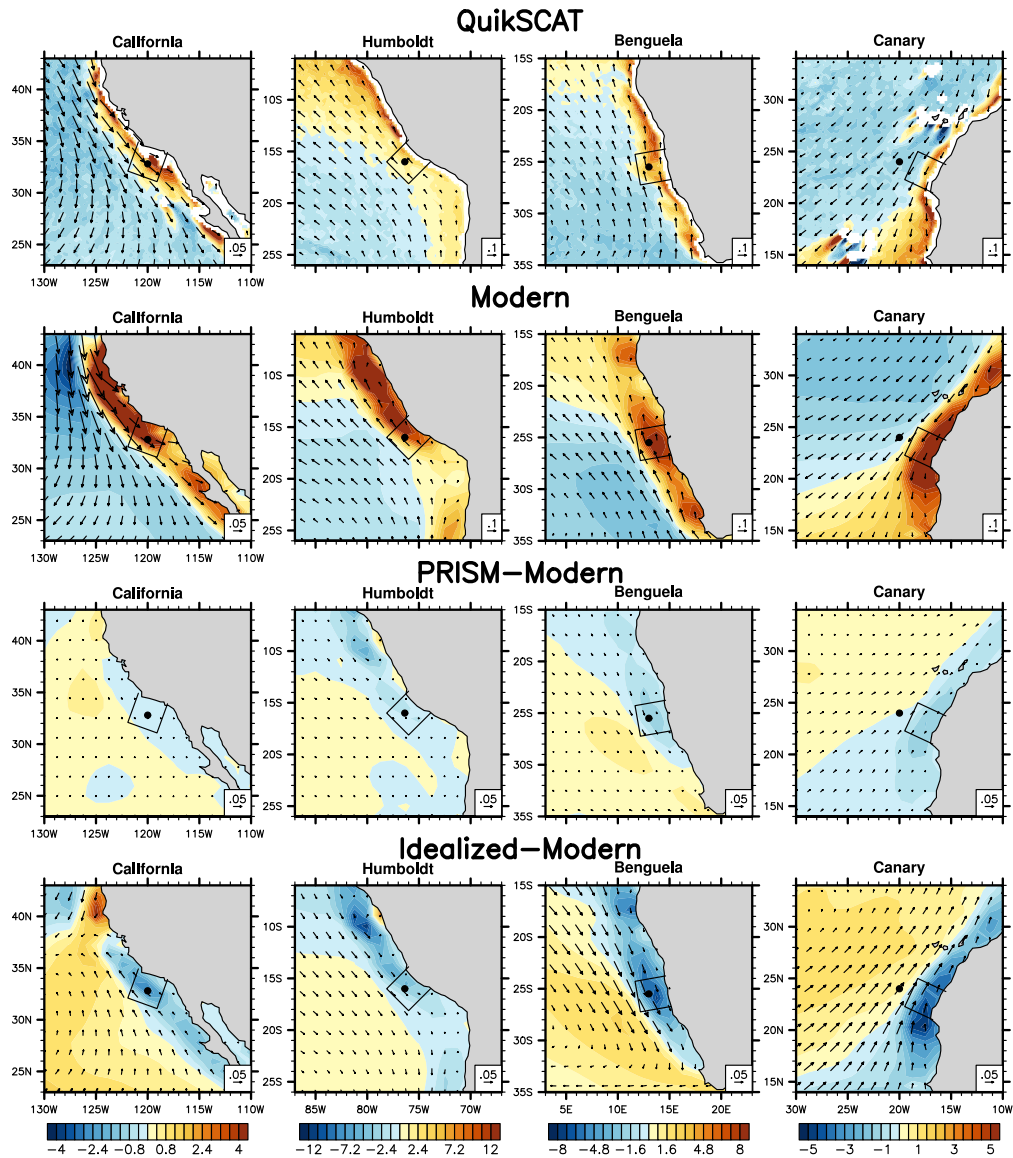
Figure 5.3.1: Annual mean surface wind stress (vectors) and upwelling due to wind stress curl (contours). Shown for QuikSCAT satellite observations (top row), the CAM5 simulation with Modern SST (upper middle), the difference between PRISM3 and Modern SST (lower middle), and the difference between Idealized and Modern SST (bottom). Upwelling units are kg/m^2/s, with a shared color scale for each site. A 0.1N/m^2 (QuikSCAT, Modern) or 0.05N/m^2 (differences) reference vector is shown in the bottom right of each panel. The model is able to reproduce the general observed patterns of wind stress curl, and simulates reductions in curl when run with estimates of Pliocene SST.

California and Humboldt Currents (Fig. 5.3.1). Figure 5.3.2 presents a local seasonal index of coastal and offshore upwelling in the area of each sediment core site. This is defined by
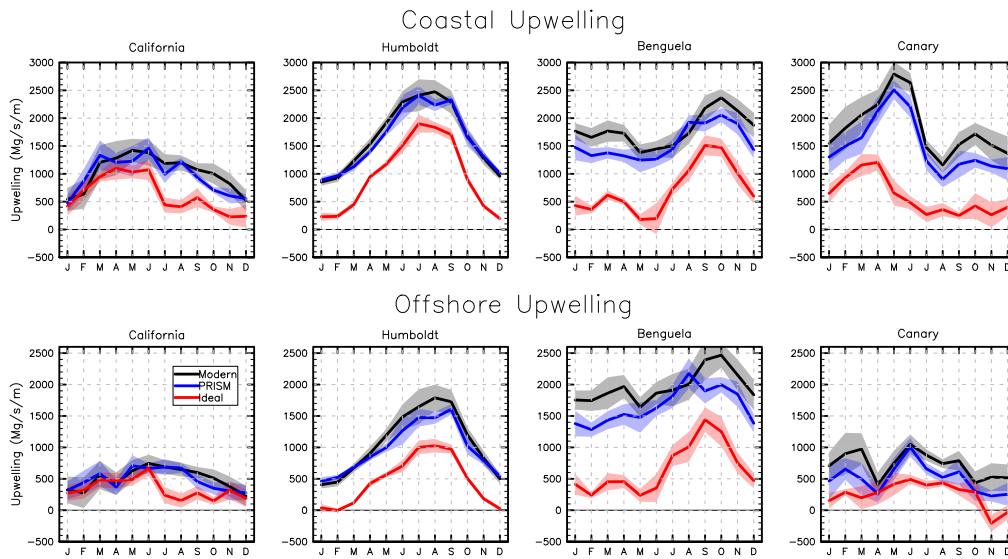
Figure 5.3.2: Monthly indices for coastal and curl-driven upwelling around each sediment core site, for the Modern (black), PRISM3 (blue) and Idealized (red) cases. Upwelling inferred from along-shore wind stress (top) and wind stress curl (bottom) is reduced when the model is run with Pliocene SST. Shaded outlines represent 95% confidence intervals based on interannual standard deviations of the monthly indices.

identifying the nearest coastal point to each sediment core site, and averaging all gridpoints within a box extending 150km in each alongshore direction, and 300km out to sea, as indicated in Fig. 5.3.1. This shows reductions in coastal upwelling of 5-20%.

The Idealized SST leads to similar changes in wind stress curl at all four sites, but with greater amplitude. This is in keeping with the idealized SST anomalies being a more extreme version of the PRISM3 reconstruction. This case also results in substantial reductions in alongshore wind stress at all four site, often 50% or greater.

These changes result from two factors, not entirely independent. First, a weakening of the Hadley circulation associated with the reduced pole-to-equator temperature gradient. This results in less subsiding air and a reduction in the strength of the subtropical highs, indicated in Figure 5.3.3. This reduces the land-sea pressure gradient and the associated along-shore winds. This weakening of the Hadley circulation has been reported in previous Pliocene modeling

studies (e.g., Brierley et al., 2009, Chandler et al., 1994), although some models simulate a broadening of the circulation rather than a decrease in strength (e.g., Haywood et al., 2000).

A second contributing factor is a decrease in the mid-latitude land-sea temperature contrast, which supports a weakened land-sea pressure gradient and weaker winds. The weaker contrast may result from the model configuration: we are prescribing sea surface temperatures, but allowing the land model to determine its own equilibrium, which depends on accurately specifying Pliocene land surface properties.

The modern land-sea contrast is reinforced by a number of positive feedbacks. For example, the combination of subsiding air and evaporation from the ocean surface produces low cloud decks over the eastern ocean regions, and the resulting high albedo contributes to relatively low surface temperatures, which in turn reinforce the subsidence regime. Since expansive low cloud decks are less prevalent over continents, a weakened Hadley circulation should reduce low cloud cover over the ocean more than over land, and the resulting radiative changes would support a reduced land-sea temperature difference. This cloud feedback is seen to a striking degree within our simulations, with subtropical ocean low cloud cover reduced by roughly 50% in the Idealized case. The corresponding radiative changes are of order +50W/m2 over oceans and -10W/m2 over land, which would strongly contribute to maintaining a weak land-sea contrast. Mid-latitude cloud changes have been previously proposed as a mechanism for explaining tropical SST changes (Barreiro and Philander, 2008), and the cloud reductions simulated here are consistent with that hypothesis.

The effects of Pliocene topography and land surface type are shown in Fig. 5.3.4. The boundary conditions include generally lower elevations in the Andes and Sierra-Nevada ranges during the Pliocene, and reduced ice-sheet elevations over Greenland and Antarctica. The Pliocene topography makes little difference around the Atlantic sites, but the California and Humboldt regions both show spatially complex changes in wind stress with magnitudes comparable to those
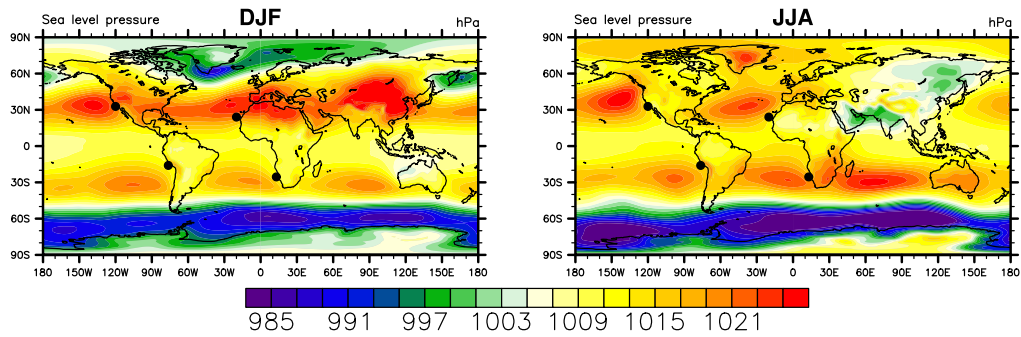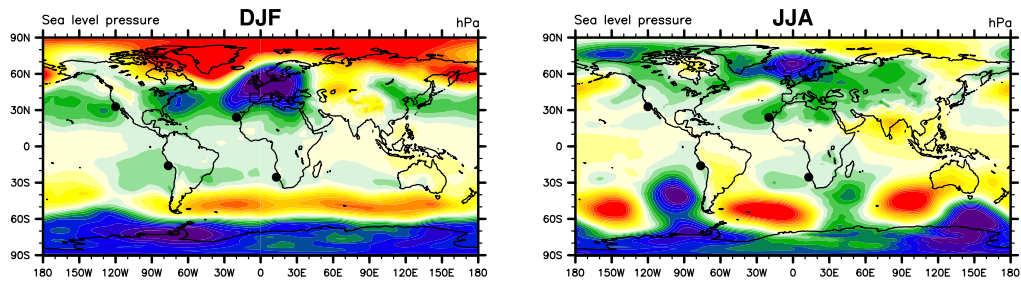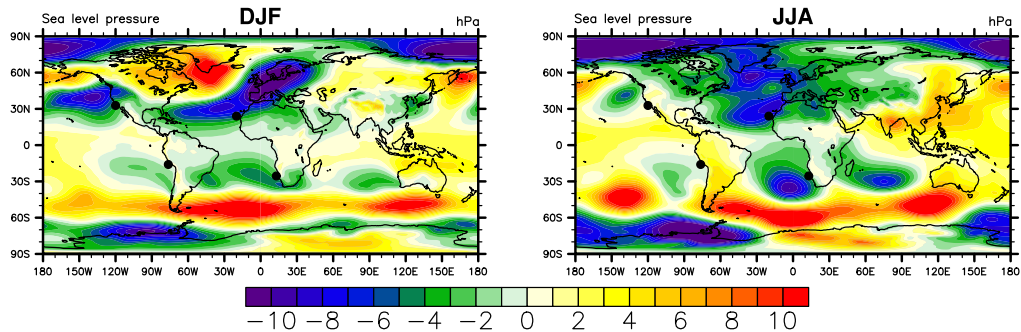
Figure 5.3.3: The annual mean sea level pressure from the Modern (top), PRISM3 (mid) and Idealized (bot) simulations. The Pliocene simulations show reductions in the strength of the subtropical highs, consistent with the weakened upwelling indices.

induced by the Idealized SST. Wind stress curl is generally reduced off California, except within roughly 100km of ODP site 1014, which sees a small increase. Changes in the Humboldt current show an alternating pattern of increases and decreases. The magnitude of these effects suggests that topography could potentially contribute to the SST anomalies at the Pacific sites, but the impacts may be local. On the other hand, use of Pliocene land types induces negligible change
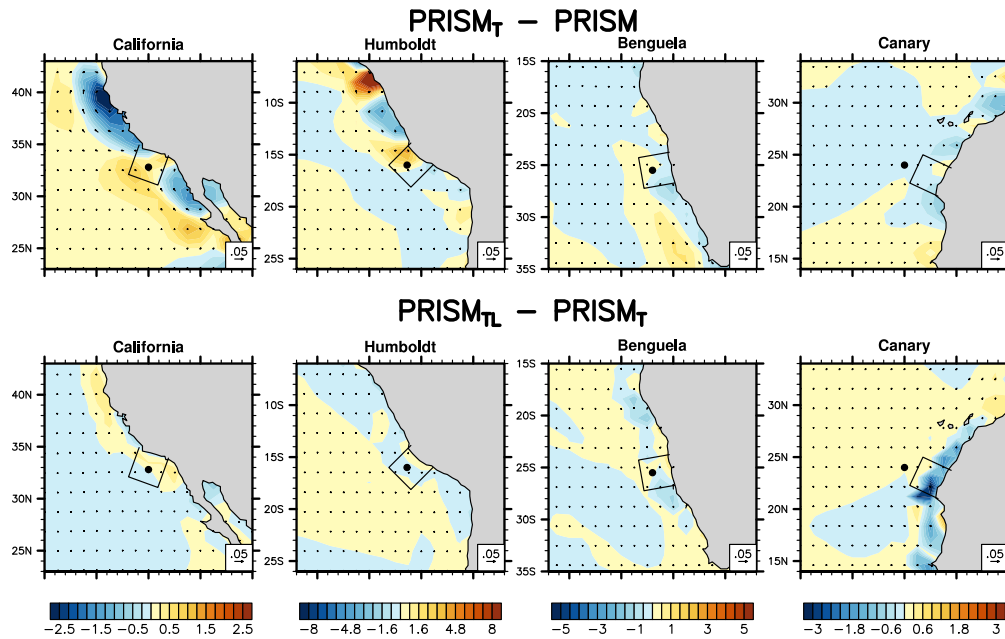
Figure 5.3.4: Changes in annual mean surface wind stress (vectors) and upwelling due to wind stress curl (contours) induced by Pliocene topography (top row), and by Pliocene land surface types (bottom). Upwelling units are kg/m^2/s, with a shared color scale for each site. A 0.05N/m^2 reference vector is shown in the bottom right of each panel. Pliocene topography has a significant effect on surface wind around the Pacific sites, while Pliocene land type affects only the Canary current.

everywhere except the Canary current, where curl is significantly decreased.

5.4 Discussion

The Pliocene is often presented as an instructive analogue for future global warming (e.g., Chandler et al., 1994, Dowsett and Robinson, 2009b, Salzmann et al., 2009), though caveats have been raised (e.g., Lunt et al., 2009). However, the analogy may be inappropriate when considering changes to coastal upwelling. The Pliocene coastal warm anomalies persisted for 2-3My (Dekens et al., 2007, Herbert and Schuffert, 1998, Marlow et al., 2000), and like the results presented here, represent a state of relative equilibrium. However, changes in upwelling over the next few decades are expected to be driven by transient effects. Bakun (1990)

hypothesized that the different rates of warming over land and ocean would lead to an increased land-sea surface pressure gradient, stronger geostrophic surface winds along the coast, and thus a transient increase in upwelling. This prediction is supported by observed trends in wind stress near all four major upwelling systems (Narayan et al., 2010), and by direct indicators of productivity and cooler temperatures off Peru (Gutiérrez et al., 2011). Interestingly, surface temperatures off California have increased slightly due to a deepening of the thermocline (Lorenzo and Al, 2005), but this seems to be a local change.

It has been argued that the Pliocene SST anomalies could not be due to changes in upwelling, based in part on the observation that proxies for SST and biological productivity are decoupled on long time-scales, and that indicators of high productivity were present during the early Pliocene (Dekens et al., 2007). However, SST and productivity are generally decoupled throughout the Pleistocene as well, after the thermocline is hypothesized to have shoaled. In fact, if productivity indicators are assumed to be linearly related to upwelling intensity, the variability seen in productivity records would imply extreme and unrealistic changes in surface wind stress. It therefore seems likely that these productivity proxies are strongly influenced by non-upwelling factors, and their long-term trends are not indicative of similar trends in upwelling. A more direct indicator of upwelling intensity, the fraction of upwelling diatoms, suggests that upwelling has increased over the last 4My in the Benguela current system (Marlow et al., 2000).

The complicated effects of topography offer a possible explanation for the apparent decoupling of SST and productivity. Topography primarily affects the offshore wind curl, which unlike coastal wind stress is generally too weak to upwell nutrient-rich bottom sediments, but can still affect SST by upwelling from shallower depths. As topography and the large-scale SST change over time, they could produce different responses in SST and productivity. To illustrate this principle, Fig. 5.4.1 shows annual-mean values of the coastal and offshore upwelling indices for the Modern run and four simulations in which PRISM3 SST, topography and land surface anomalies (relative to Modern) are scaled from 0.25 to 1. These could represent, in a crude sense,
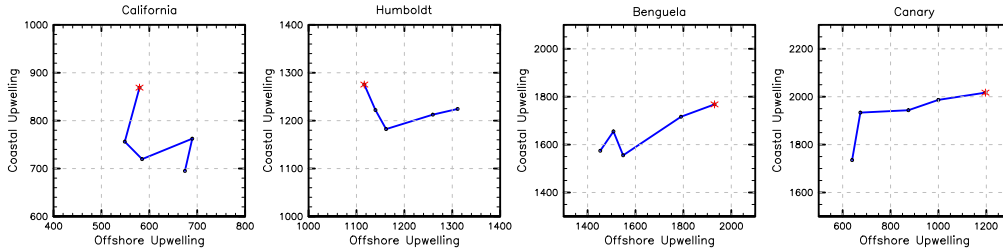
Figure 5.4.1: Annual-mean coastal and offshore upwelling indices for the Modern run (red star) and four simulations in which PRISM3 SST, topography and land surface anomalies are scaled from 0.25 to 1. This demonstrates a hypothetical evolution over time in which coastal and offshore upwelling do not covary.

the evolution of boundary conditions over the last 3Ma. The results indicate that nonlinear and independent histories of coastal and offshore upwelling can be generated even from a linear scaling of the boundary conditions.

To explain the actual upwelling histories at these sites would likely require a regional modeling approach. The model grid used here, while relatively high resolution, is not fine enough to capture the small-scale effects of local topography, which can account for a significant component of wind stress curl. For example, the protrusion of the California coastline at Point Conception is associated with enhanced wind stress curl and upwelling in the Southern California bight (Pickett, 2003). Winant and Dorman (1997) found that going from $1°$ to $0.2°$ resolution increases the observed wind stress curl off California by a factor of three. Mesoscale variations in sea surface temperature are also known to modulate the local wind speed and thereby the upwelling (Boé et al., 2011). It is possible that small scale effects could have differed significantly between the Pliocene and the present, given changes in sea level and coastal topography, though it is unclear if this would systematically increase or decrease upwelling.

Lastly, we note that the land-sea surface pressure contrast, and thus the surface wind stress, can vary with orbitally-induced changes in insolation (e.g., Diffenbaugh and Ashfaq, 2007). Although there is evidence for orbitally driven variability during the Pliocene (Lisiecki and Raymo, 2005, Willeit et al., 2013), the long persistence of the coastal warm anomalies argues against an orbital

106

explanation.

5.5 Conclusions

Simulations with the global Community Atmosphere Model (CAM5; Neale and CoAuthors, 2010) demonstrate that two different reconstructions of Pliocene sea surface temperatures imply reductions in upwelling-favorable wind around the four major eastern boundary current regions. Use of the mid-Piacenzian (3.29-2.97Ma) SST reconstruction developed by the PRISM group results in reductions of 10-20% in the Canary and Benguela current systems, and smaller reductions of 5-10% in the California and Humboldt systems. An idealized reconstruction of the earlier Pliocene warm period (4-4.2Ma) results in larger reductions of 20-50%, depending on season. In both scenarios, changes in wind stress are driven by the combination of a general weakening of the Hadley circulation and a reduction in the land-sea temperature contrast. These results suggest that at least part of the warm anomalies found at Pliocene coastal sediment core sites may be attributed to reductions in upwelling intensity. Further work, perhaps with regional ocean models, is needed to quantify the impact of wind stress changes on upwelling and local surface temperatures.

What is not surrounded by uncertainty cannot be the truth.

Richard Feynman

6

Conclusions

THIS THESIS HAS EXAMINED the possibility of superrotation - persistent westerly winds over the equator - in Earth's troposphere. Superrotation depends on up-gradient transport of angular momentum, which can only be provided by eddy motions excited around the equator. These in turn require organized convection to serve as a wave source. Numerical simulations show that superrotation will reliably develop in the presence of sufficiently strong wave forcing, but how this forcing varies with Earth's climate is an open question.

In Chapter 2 we argued that the Madden-Julian Oscillation (MJO) could become more

frequent and more intense in a warmer climate. The MJO is a strong tropical wave source, and plays a critical role in many model transitions to superrotation (Caballero and Huber, 2010, Lee, 1999), but its representation in most models is also unrealistic. To examine MJO dependence on surface temperature we used the super-parameterized version of the Community Atmosphere Model (SP-CAM), which is known to produce a realistic MJO. We ran aquaplanet simulations with prescribed zonally-uniform SST, and increased the SST in globally-uniform increments of 3K. In response, the model produced a significant increase in MJO activity. With an equatorial SST of $26°C$, convection was only weakly organized, but at $35°C$ the tropics were dominated by a strong MJO-like phenomenon. Equatorial OLR variance in the MJO wavenumber-frequency band (k=1-3,P=20-100d) nearly tripled between the low and high SST cases. Consistent with previous work (Caballero and Huber, 2010), we found that the standard deviation of equatorial 200hPa zonal wind (a proxy for eddy activity) scaled linearly with SST, and the zonal wind near the equatorial tropopause increased at roughly 1.1m/s/K. A momentum flux cospectrum confirmed the acceleration of mean zonal wind is driven by an increase in momentum convergence within the MJO band.

To identify a physical mechanism for this MJO intensification, we examined the moist static energy (MSE) budget for a composite MJO event. Consistent with previous work (e.g., Andersen and Kuang, 2012), we found that the model MJO is almost entirely supported by longwave radiative anomalies due to variation in high cloud fraction, and primarily damped by anomalous horizontal advection. In a novel result, the vertical advection was shown to damp the MJO at low SST, but became an energy source at high SST, suggesting that it plays a role in the intensification. A decomposition of the vertical advection term indicated that the change with SST is entirely associated with the intraseasonal vertical velocity acting on the mean vertical MSE profile. The mean MSE profile was then shown to steepen with SST as a result of maintaining a moist adiabatic lapse rate with minimal changes in the relative humidity profile. Since this change in MSE profile is a fundamental thermodynamic consequence of warming, it suggests that MJO

intensification may be similarly robust. The mechanism also depends on the vertical velocity profile, which can change to compensate the MSE profile. In these experiments this compensation was incomplete, but this could be a function of the aquaplanet configuration.

The conclusions from these aquaplanet simulations were then tested in a much more realistic framework in Chapter 3, where we used a fully coupled atmosphere-ocean model, the super-parameterized version of the Community Earth System Model (SP-CESM). Two simulations in near-equilibrium with pre-industrial ($1\times$) and quadrupled ($4\times$) CO_2 were run with present-day continents and topography, a seasonal cycle, and a full dynamic ocean. The MJO in the $1\times CO_2$ simulation was evaluated and found to agree very well with observations. Composites of OLR and precipitation showed the magnitude, spatial structure, eastward propagation, and seasonality of the model MJO were all similar to observed. The total variability in equatorial OLR was somewhat underestimated, but variance within the MJO band was realistically enhanced relative to the weaker background.

The $4\times CO_2$ resulted in 4.2K of tropical-mean warming, with various changes to the tropical climatology. Several metrics of MJO activity, including the absolute variance of OLR and precipitation in the MJO band and the ratio of eastward to westward intraseasonal variance, indicated an increase with warming. A counting algorithm based on the Wheeler and Hendon (2004) index was used to show that the number of distinct MJO events increased by 20-30%.

To understand the mechanism behind these changes, we again calculated a composite MSE budget, which showed a physical balance similar to the aquaplanet MJO. Two terms were found to become more destabilizing with warming: the surface latent heat flux, and vertical advection. As in the aquaplanet case, a decomposition of the vertical advection term revealed that the change with warming is due to the MJO vertical velocities acting on the climatological MSE profile, which was found to steepen with warming as expected. The surface latent heat fluxes were also decomposed into component processes, and we found that their contribution to the MJO scales roughly with the surface saturation specific humidity. Because this scaling is weaker than that of

the MJO column MSE anomalies, the relative forcing provided by surface fluxes decreases. We conclude that the MJO intensification with SST likely resulted from the steepening MSE profile, and the relatively weaker latent heat flux scaling provided a positive feedback.

In Chapter 4 we proposed a positive feedback on the equatorial zonal wind which can lead to abrupt transitions from a conventional circulation to a strongly superrotating state. The feedback is based on the resonant response of a forced equatorial Rossby wave embedded in a uniform zonal flow. If the zonal wind approaches a velocity equal and opposite to the Rossby wave phase speed, the Rossby wave pattern will become stationary relative to the prescribed forcing and amplify significantly, implying a peak in momentum convergence at the resonant velocity. For mean zonal winds below the resonant velocity, westerly perturbations will result in increased meridional momentum convergence, which leads to further increases in equatorial wind speed.

This feedback was studied in a dry, idealized GCM forced with prescribed equatorial eddy heating. We first considered a simplified case, in which the meridional gradient in prescribed Newtonian cooling was eliminated, along with the Hadley circulation and mid-latitude jets. The magnitude of eddy heating was incrementally increased until an abrupt transition was triggered, in which equatorial wind jumped from 2m/s to 24m/s. A window of multiple equilibria was also identified where jets of 2m/s or 19m/s can exist for the same eddy heating rate. The wave pattern from the GCM closely matched the analytical solutions to the shallow water equations on an equatorial beta plane, linearized around a uniform zonal wind. The amplitude of the wave and its associated momentum convergence also scaled with the mean zonal wind as predicted by theory, peaking at the Rossby wave resonance velocity. This was verified for multiple resonant velocities by varying the wavenumber and propagation speed of the prescribed eddy heating.

Abrupt transitions were also seen in a case with a non-zero meridional temperature gradient, but no multiple equilibria were identified. The presence of a strong mean circulation and mid-latitude eddy activity complicated attribution in this case, since separate positive feedbacks involving these phenomena have been previously proposed (Saravanan, 1993, Shell and Held,

2004). However, examination of the momentum flux cospectrum indicated that the abrupt transition is driven by momentum convergence at a low zonal wavenumber ($k = 1$) corresponding to the forced tropical waves, as proposed here, rather than involving the zonal-mean circulation or mid-latitude waves at higher wavenumber ($k = 4 - 7$), as proposed previously. Finally, we added a simple seasonal cycle to the Hadley circulation. Although this significantly enhanced the "winter" hemisphere Hadley cell and reduced the zonal wind velocity for a given level of forcing, a strong abrupt transition was still seen.

In Chapter 5, we considered the possibility of superrotation in the Pliocene. A reduction in the equatorial easterlies driven by enhanced MJO variability has been proposed as an explanation for the Pliocene "permanent El Niño". However, this hypothesis is complicated by similar Pliocene warm anomalies found at mid-latitude upwelling sites; a satisfying explanation for the equatorial data should also account for the mid-latitudes. To free up space for the superrotation hypothesis, we examined an independent explanation for the mid-latitude data: the possibility that coastal winds could be weakened by large-scale differences in Pliocene SST, topography and surface boundary conditions.

To test the effect of large-scale Pliocene SST, we ran CAM with two different Pliocene SST reconstructions. Both experiments showed reductions of 10-50% in upwelling winds at all four mid-latitude sites relative to a modern control run. Additional experiments showed that Pliocene topography can have significant local effects around the two Pacific upwelling sites, but the effect is highly spatially dependent and unlikely to account for the systematic warm anomalies seen in the proxy record. The effect of Pliocene land surface types was found to be negligible. We conclude that any reduction in Pliocene mid-latitude upwelling is most likely to result from the large-scale SST anomalies. Further work is required to determine if these reductions are sufficient to explain the mid-latitude upwelling site warm anomalies.

These results suggest that the tropics' dominant transient wave source, the MJO, is likely to

intensify in warm climates. The underlying cause, a steepening of the mean MSE gradient, is a very robust consequence of warming, suggesting that MJO intensification is similarly robust. However, this effect is partially offset by changes in the profile of vertical velocity, which are less well constrained. Though the compensation is small in the models used here, it is likely to depend on the specific convection parameterization, among other factors. Previous studies have shown that the spatial pattern of warming can significantly affect the MJO response by altering the gross moist stability (Maloney and Xie, 2013), which may be one manifestation of this dependence.

The scaling with SST of momentum convergence and equatorial westerlies in these models (approximately 1m/s/K) suggests that a strong westerly jet is unlikely to develop in near-modern climates, although idealized studies have now identified several positive feedback mechanisms that could amplify a small westerly anomaly. These feedbacks likely operate to some degree in the real atmosphere, but the lack of abrupt transitions in complex models suggests that the feedback signal may be drowned out by atmospheric "noise" and damping processes.

A potential problem with invoking superrotation to explain surface paleodata is that, in numerical simulations, increases in zonal wind are generally confined to the upper troposphere, and have little impact on the surface. This is likely due in part to the lack of convective momentum transport, which until recently has not been included in convection parameterizations. This could serve to more strongly couple the surface winds with those aloft.

A

Appendix A: Derivation of shallow water solutions

Phlips and Gill (1987) found analytic solutions for the equatorial response to a heating of limited spatial extent. We consider the simplified problem of a global scale sinusoidal heating of the form $Q = Q_0 \cos(kx) \exp(-y^2/4)$. It is assumed that the solutions are separable in x, y and z, and that the heating projects only onto the first baroclinic mode. This allows variables to be expressed as, for example, $Q = F(x) \sum Q_n D_n(y)$, where $D_n(y)$ is the nth parabolic cylinder function. We refer the reader to the original paper for additional details.

We non-dimensionalize the shallow water equations, using horizontal scale $\sqrt{c/2\beta}$ and temporal scale $(2\beta c)^{1/2}$.

$$\partial_t u + U\partial_x u + \epsilon u - \beta y v = -\partial_x \phi$$

$$\partial_t v + U\partial_x v + \epsilon v - \beta y u = -\partial_y \phi$$

$$\partial_t \theta + U\partial_x \theta + \epsilon \theta + w = Q$$

$$\theta = \partial_z \phi$$

$$\partial_x u + \partial_y v + \partial_z w = 0$$

Defining $q = \phi + u$ and $r = \phi - u$, it can be shown that the steady state Kelvin mode response is governed by the single equation,

$$(U\partial_x + \epsilon)q_0 + \partial_x q_0 = -Q_0 \cos(kx) \ .$$

Substituting an assumed solution of the form $q_0 = A\cos(kx) + B\sin(kx)$ leads to $A = \frac{-Q_0\gamma^2}{\epsilon(1+\gamma^2)}$, $B = \frac{-Q_0\gamma}{\epsilon(1+\gamma^2)}$, where $\gamma = \frac{\epsilon}{k(U+c_n)}$, and c_n is the wave speed for mode n.

Relating q to u and ϕ, we find,

$$u_k = \phi_k = \frac{-Q_0\gamma}{2\epsilon(1+\gamma^2)} \left[\gamma \cos\left(kx\right) + \sin\left(kx\right)\right] \exp\left(-y^2/4\right)$$

where the subscript k designates the Kelvin mode response.

The Rossby modes $n > 0$ are governed by three equations, after dropping terms which are second-order in ϵ and U,

$$(Uk + \epsilon)q_{n+1} + kq_{n+1} - v_n = -Q_{n+1}F(x)$$

$$(Uk + \epsilon)r_{n-1} - kr_{n-1} + nv_n = Q_{n-1}F(x)$$

$$2(Uk + \epsilon)v_n + (n+1)q_{n+1} - r_{n-1} = 0$$

These can be manipulated to find a single equation in q. Since our forcing Q projects only onto the $n = 1$ mode, this equation is given by

$$(1 - 3U)kq_2 - 3\epsilon q_2 = Q_0 \cos(kx)$$

Substituting a solution of the form $q_2 = A \cos\left(kx\right) + B \sin\left(kx\right)$ leads to $A = \frac{-\frac{1}{3}Q_0\gamma^2}{\epsilon(1+\gamma^2)}$, $B = \frac{-\frac{1}{3}Q_0\gamma}{\epsilon(1+\gamma^2)}$.

Finally, q_2 may be translated into u and v,

$$u = \frac{Q_0\gamma}{6\epsilon(1+\gamma^2)} \left[\gamma \cos\left(kx\right) + \sin\left(kx\right)\right]\left(3 - y^2\right) \exp\left(-y^2/4\right)$$

$$v = \left[\frac{-\frac{4}{3}Q_0\gamma}{\epsilon(1+\gamma^2)} \left[(Uk + \epsilon\gamma \cos\left(kx\right) + (\epsilon - Uk\gamma) \sin\left(kx\right)\right] + Q_0 \cos\left(kx\right)\right] y \, \exp\left(-y^2/4\right).$$

References

Adler, R., et al., 2003: The Version 2 Global Precipitation Climatology Project (GPCP) Monthly Precipitation Analysis (1979-Present). *J. Hydrometeor.*, **4**, 1147–1167.

Andersen, J. A. and Z. Kuang, 2012: Moist Static Energy Budget of MJO-like disturbances in the atmosphere of a zonally symmetric aquaplanet. *J. Climate*, **25**, 2782–2804.

Arnold, N. P., Z. Kuang, and E. Tziperman, 2013: Enhanced MJO-like Variability at High SST. *J. Climate*, **26**, 988–1001.

Arnold, N. P., E. Tziperman, and B. Farrell, 2012: Abrupt Transition to Strong Superrotation Driven by Equatorial Wave Resonance in an Idealized GCM . *J. Atmos. Sci.*, **69**, 626–640.

Bakun, A., 1990: Global climate change and intensification of coastal ocean upwelling. *Science (New York, N.Y.)*, **247 (4939)**, 198–201.

Barreiro, M. and S. G. Philander, 2008: Response of the tropical Pacific to changes in extratropical clouds. *Climate Dynamics*, **31 (6)**, 713–729.

Bellon, G. and A. Sobel, 2008: Poleward-Propagating Intraseasonal Monsoon Disturbances in an Intermediate-Complexity Axisymmetric Model. *J. Atmos. Sci.*, **65**, 470–489.

Benedict, J. J. and D. A. Randall, 2007: Observed Characteristics of the MJO Relative to Maximum Rainfall. *J. Atmos. Sci.*, **64**, 2332–2354.

Benedict, J. J. and D. A. Randall, 2009: Structure of the Madden–Julian Oscillation in the Superparameterized CAM. *J. Atmos. Sci.*, **66 (11)**, 3277–3296.

Biello, J. A., A. J. Majda, and M. W. Moncrieff, 2007: Meridional Momentum Flux and Superrotation in the Multiscale IPESD MJO Model. *J. Atmos. Sci.*, **64**, 1636–1651.

Blade, I. and D. L. Hartmann, 1993: Tropical Intraseasonal Oscillations in a Simple Nonlinear Model. *J. Atmos. Sci.*, **50 (17)**, 2922–2939.

Boccaletti, G., R. C. Pacanowski, S. G. H. Philander, and A. V. Fedorov, 2004: The Thermal Structure of the Upper Ocean. *J. Phys. Ocean.*, **34**, 888–902.

Boé, J., A. Hall, F. Colas, J. C. McWilliams, X. Qu, J. Kurian, and S. B. Kapnick, 2011: What shapes mesoscale wind anomalies in coastal upwelling zones? *Climate Dynamics*, **36** (**11-12**), 2037–2049.

Bony, S., J.-L. Dufresne, H. L. Le Treut, J.-J. Morcrette, and C. Senior, 2004: Dynamic and Thermodynamic components of cloud changesl. *Climate Dynamics*, **22**, 71–86.

Bretherton, C. S., M. E. Peters, and L. E. Back, 2004: Relationships between Water Vapor Path and Precipitation over the Tropical Oceans. *J. Climate*, **17**, 1517–1528.

Brierley, C., A. Fedorov, T. Herbert, K. T. Lawrence, and J. P. LaRiviere, 2009: Greatly expanded tropical warm pool and weakened Hadley circulation in the early Pliocene. *Science*, **323**, 1714–1718.

Caballero, R. and M. Huber, 2010: Spontaneous transition to superrotation in warm climates simulated by CAM3. *Geophys. Res. Lett.*, **37** (**11**), 1–5.

Caballero, R. and M. Huber, 2013: State-dependent climate sensitivity in past warm climates and its implications for future climate projections. *Proc. Nat. Acad. Sci.*, **110** (**35**), 14 162–14 167.

Chaisson, W., 1995: Planktonic foraminiferal assemblages and paleoceanographic change in the trans-tropical Pacific Ocean: A comparison of west (Leg 130) an east (Leg 138), latest Miocene to Pleistocene. *Proc. Ocean Drill. Program Sci. Results*, **138**, 555–597.

Chandler, M., D. Rind, and R. Thompson, 1994: Joint investigations of the middle Pliocene climate II: GISS GCM Northern Hemisphere results. *Global and Planetary Change*, **9**, 197–219.

Chou, C. and J. D. Neelin, 2004: Mechanisms of Global Warming Impacts on Regional Tropical Precipitation. *J. Climate*, **17**, 2688–2701.

Dekens, P. S., A. C. Ravelo, and M. D. McCarthy, 2007: Warm upwelling regions in the Pliocene warm period. *Paleoceanography*, **22** (**3**), 1–12.

Derbyshire, S., I. Beau, P. Bechtold, J.-Y. Grandpeix, J.-M. Piriou, J.-L. Redelsperger, and P. Soares, 2004: Sensitivity of moist convection to environmental humidity. *Quart. J. Roy. Met. Soc.*, **130** (**604**), 3055–3079.

Diffenbaugh, N. S. and M. Ashfaq, 2007: Response of California Current forcing to mid-Holocene insolation and sea surface temperatures. *Paleoceanography*, **22** (**3**), 1–7.

Dima, I. M., J. M. Wallace, and I. Kraucunas, 2005: Tropical Zonal Momentum Balance in the NCEP Reanalyses. *J. Atmos. Sci.*, **62**, 2499–2513.

Dowsett, H., J. Barron, and R. Poore, 1996: Middle Pliocene sea surface temperatures: a global reconstruction. *Marine Micropaleontology*, **27**, 13–25.

Dowsett, H. J. and T. M. Cronin, 1990: High eustatic sea level during the middle Pliocene: Evidence from the southeastern U.S. Atlantic Coastal Plain. *Geology*, **18**, 435–438.

Dowsett, H. J., A. M. Haywood, P. J. Valdes, M. M. Robinson, D. J. Lunt, D. J. Hill, D. K. Stoll, and K. M. Foley, 2011: Sea surface temperatures of the mid-Piacenzian Warm Period: A comparison of PRISM3 and HadCM3. *Paleogeography, Paleoclimatology, Paleoecology*, **309**, 83–91.

Dowsett, H. J. and R. Z. Poore, 1991: Pliocene Sea Surface Temperatures of the North Atlantic Ocean at 3.0Ma. *Quat. Sci. Rev.*, **10**, 189–204.

Dowsett, H. J. and M. M. Robinson, 2009a: Mid-Pliocene equatorial Pacific sea surface temperature reconstruction: a multi-proxy perspective. *Phil. Trans. R. Soc.*, **367**, 109–125.

Dowsett, H. J. and M. M. Robinson, 2009b: Mid-Pliocene equatorial Pacific sea surface temperature reconstruction: a multi-proxy perspective. *Phil. Trans. R. Soc. A*, **367**, 109–125.

Emanuel, K. A., 1987: An Air-Sea Interaction Model of Intraseasonal Oscillations in the Tropics. *J. Atmos. Sci.*, **44** (**16**), 2324–2340.

Fedorov, A., C. M. Brierley, and K. Emanuel, 2010: Tropical cyclones and permanent El Niño in the early Pliocene epoch. *Nature*, **463**, 1066–1070.

Fedorov, A. V., R. Pacanowski, S. G. Philander, and G. Boccaletti, 2004: The Effect of Salinity on the Wind-Driven Circulation and the Thermal Structure of the Upper Ocean. *J. Phys. Ocean.*, **34**, 1949–1966.

Frank, W. M. and P. E. Roundy, 2006: The Role of Tropical Waves in Tropical Cyclogenesis. *Mon. Weath. Rev.*, **134**, 2397–2417.

Fuchs, Z. and D. J. Raymond, 2002: Large-Scale Modes of a Nonrotating Atmosphere with Water Vapor and Cloud-Radiation Feedbacks. *J. Atmos. Sci.*, **59**, 1669–1679.

Gill, A. E., 1980: Some simple solutions for heat-induced tropical circulation. *Quart. J. Roy. Meteor. Soc*, **106** (**449**), 447–462.

Grabowski, W. W., 2001: Coupling Cloud Processes with the Large-Scale Dynamics Using the Cloud-Resolving Convection Parameterization (CRCP). *J. Atmos. Sci.*, **58**, 978–997.

Grabowski, W. W., 2003: MJO-like Coherent Structures: Sensitivity Simulations Using the Cloud-Resolving Convection Parameterization (CRCP). *J. Atmos. Sci.*, **60**, 847–864.

Grabowski, W. W., 2004: An Improved Framework for Superparameterization. *J. Atmos. Sci.*, **61** (**15**), 1940–1952.

Grodsky, S. A., A. Bentamy, J. A. Carton, and R. T. Pinker, 2009: Intraseasonal Latent Heat Flux Based on Satellite Observations. *J. Climate*, **22**, 4539–4556.

Gutiérrez, D., et al., 2011: Coastal cooling and increased productivity in the main upwelling zone off Peru since the mid-twentieth century. *Geophys. Res. Lett.*, **38** (**7**), 1–6, doi: 10.1029/2010GL046324, URL http://www.agu.org/pubs/crossref/2011/2010GL046324.shtml.

Hall, J. D., A. J. Matthews, and D. J. Karoly, 2001: The Modulation of Tropical Cyclone Activity in the Australian Region by the Madden-Julian Oscillation. *Mon. Weath. Rev.*, **129**, 2970–2982.

Hannah, W. M. and E. D. Maloney, 2011: The Role of Moisture–Convection Feedbacks in Simulating the Madden–Julian Oscillation. *J. Climate*, **24** (**11**), 2754–2770.

Hartmann, D. L. and K. Larson, 2002: An important constraint on tropical cloud - climate feedback. *Geophys. Res. Let.*, **29** (**20**), 10–13.

Hayashi, Y.-Y. and A. Sumi, 1986: The 30-40 Day Oscillations Simulated in an Aqua Planet Model. *J. Met. Soc. Japan*, **64** (**4**), 451–467.

Haywood, A. M., P. J. Valdes, and B. W. Sellwood, 2000: Global scale palaeoclimate reconstruction of the middle Pliocene climate using the UKMO GCM: initial results. *Global and Planetary Change*, **25**, 239–256.

Haywood, A. M., et al., 2010: Pliocene Model Intercomparison Project (PlioMIP): experimental design and boundary conditions (Experiment 1). *Geoscientific Model Development*, **3** (**1**), 227–242, doi: 10.5194/gmd-3-227-2010, URL http://www.geosci-model-dev.net/3/227/2010/.

Haywood, A. M., et al., 2012: Large-scale features of Pliocene climate: results from the Pliocene Model Intercomparison Project. *Clim. Past Discuss.*, **8** (**4**), 2969–3013, doi: 10.5194/cpd-8-2969-2012, URL http://www.clim-past-discuss.net/8/2969/2012/.

Held, I. M., 1999a: Equatorial Superrotation in Earth-like Atmospheric Models. Paper presented at Annual Meeting, Am. Meteor. Soc., Dallas, TX., (Available at http://www.gfdl.noaa.gov/cms-filesystem-action/user_files/ih/lectures/super.pdf).

Held, I. M., 1999b: The macroturbulence of the troposphere. *Tellus*, **51A-B**, 69–70.

Held, I. M. and B. J. Soden, 2006: Robust Responses of the Hydrological Cycle to Global Warming. *J. Climate*, **19**, 5686–5699.

Held, I. M. and M. J. Suarez, 1978: A Two-Level Primitive Equation Atmospheric Model Designed for Climatic Sensitivity Experiments. *J. Atmos. Sci.*, **35**, 206–229.

Held, I. M. and M. J. Suarez, 1994: A Proposal for the Intercomparison of the Dynamical Cores of Atmospheric General Circulation Models. *Bull. Amer. Meteor. Soc.*, **75** (**10**), 1825–1830.

Hendon, H. H., C. Zhang, and J. D. Glick, 1999: Interannual Variation of the Madden-Julian Oscillation during Austral Summer. *J. Climate*, **12**, 2538–2550.

Herbert, T. D. and J. D. Schuffert, 1998: Alkenone unsaturation estimates of late Miocene through late Pliocene sea surface temperatures at Site 958. *Proc. Ocean Drill. Program Sci. Results*, **159T**, 17–21.

Hide, R., 1969: Dynamics of the Atmospheres of the Major Planets. *J. Atmos. Sci.*, **26**, 841–852.

Holton, J. R., 2004: *An Introduction to Dynamic Meteorology, 4th ed.* Elsevier Academic Press, 511 pp.

Hoskins, B. J. and D. J. Karoly, 1981: The Steady Linear Response of a Spherical Atmosphere to Thermal and Orographic Forcing. *J. Atmos. Sci.*, **38**, 1179–1196.

Hoskins, B. J., R. B. Neale, M. Rodwell, and Y. Gui-Ying, 1999: Aspects of the large-scale tropical atmospheric circulation. *Tellus*, **51**, 33–44.

Huang, H.-P., P. Sardeshmukh, and K. Weickmann, 1999: The balance of global angular momentum in a long-term atmospheric data set. *J. Geophys. Res.*, **104**, 2031–2040.

Huang, H.-P. and K. M. Weickmann, 2001: Trend in Atmospheric Angular Momentum in a Transient Climate Change Simulation with Greenhouse Gas and Aerosol Forcing. *J. Climate*, **14**, 1525–1534.

Inness, P. M. and J. M. Slingo, 2003: Simulation of the Madden–Julian Oscillation in a Coupled General Circulation Model. Part I: Comparison with Observations and an Atmosphere-Only GCM. *J. Climate*, **16** (3), 345–364.

Jones, C. and L. M. Carvalho, 2006: Changes in the Activity of the Madden-Julian Oscillation during 1958-2004. *J. Climate*, **19**, 6353–6370.

Jones, C. and L. M. V. Carvalho, 2011: Will global warming modify the activity of the Madden-Julian Oscillation? *Quart. J. R. Met. Soc.*, **137**, 544–552.

Jones, C., D. E. Waliser, K. M. Lau, and W. Stern, 2004: Global Occurrences of Extreme Precipitation and the Madden–Julian Oscillation: Observations and Predictability. *J. Climate*, **17**, 4575–4589.

Kalnay, E. and Coauthors, 1996: The NCEP/NCAR 40-Year Reanalysis Project. *Bull. Amer. Meteor. Soc.*, **77**, 437–471.

Kemball-Cook, S., B. Wang, and X. Fu, 2002: Simulation of the Intraseasonal Oscillation in the ECHAM-4 Model: The Impact of Coupling with an Ocean Model. *J. Atmos. Sci.*, **59** (9), 1433–1453.

Khairoutdinov, M., D. Randall, and C. DeMott, 2005: Simulations of the Atmospheric General Circulation Using a Cloud-Resolving Model as a Superparameterization of Physical Processes. *J. Atmos. Sci.*, 2136–2154.

Khairoutdinov, M. F. and D. A. Randall, 2001: A Cloud Resolving Model as a Cloud Parameterization in the NCAR Community Climate System Model: Preliminary Results. *Geophys. Res. Let.*, **28** (**18**), 3617–3620.

Khairoutdinov, M. F. and D. A. Randall, 2003: Cloud Resolving Modeling of the ARM Summer 1997 IOP: Model Formulation, Results, Uncertainties, and Sensitivities. *J. Atmos. Sci.*, **60** (**4**), 607–625.

Kiladis, G. N., K. H. Straub, and P. T. Haertel, 2005: Zonal and Vertical Structure of the Madden-Julian Oscillation. *J. Atmos. Sci.*, **62**, 2790–2809.

Kiladis, G. N., M. C. Wheeler, P. T. Haertel, K. H. Straub, and P. E. Roundy, 2009: Convectively Coupled Equatorial Waves. *Rev. Geophys.*, **47**, 42.

Kim, D., A. H. Sobel, and I.-S. Kang, 2011: A mechanism denial study on the Madden-Julian Oscillation. *J. Adv. Model. Earth Syst.*, **3**.

Kim, D., et al., 2009: Application of MJO Simulation Diagnostics to Climate Models. *J. Climate*, **22** (**23**), 6413–6436.

Kiranmayi, L. and E. Maloney, 2011: The Intraseasonal Moist Static Energy Budget in Reanalysis Data. *J. Geophys. Res.*, **116** (**November**), 1–12.

Kraucunas, I. and D. L. Hartmann, 2005: Equatorial Superrotation and the Factors Controlling the Zonal-Mean Zonal Winds in the Tropical Upper Troposphere. *J. Atmos. Sci.*, **62**, 371–389.

Kuang, Z., 2008: A Moisture-Stratiform Instability for Convectively Coupled Waves. *J. Atmos. Sci.*, **65**, 834–854.

Kuang, Z., 2011: The Wavelength Dependence of the Gross Moist Stability and the Scale Selection in the Instability of Column-Integrated Moist Static Energy. *J. Atmos. Sci.*, **68**, 61–74.

Lavender, S. L. and A. J. Matthews, 2009: Response of the West African Monsoon to the Madden-Julian Oscillation. *J. Climate*, **22**, 4097–4116.

Lee, M.-I., I.-S. Kang, and B. E. Mapes, 2003: Impacts of Cumulus Convection Parameterization on Aqua-planet AGCM Simulations of Tropical Intraseasonal Variability. *J. Met. Soc. Japan*, **81** (**5**), 963–992.

Lee, S., 1999: Why Are the Climatological Zonal Winds Easterly in the Equatorial Upper Troposphere? *J. Atmos. Sci.*, **56**, 1353–1363.

Lee, S., S. Feldstein, D. Pollard, and T. White, 2011: Do planetary wave dynamics contribute to equable climate? *J. Climate*, **24**, 2391–2404.

Liebmann, B. and C. Smith, 1996: Description of a complete (interpolated) outgoing longwave radiation dataset. *Bull. Amer. Met. Soc.*, **77**, 1275–1277.

Lin, J.-L., G. N. Kiladis, B. E. Mapes, K. M. Weickmann, K. R. Sperber, W. Lin, M. C. Wheeler, and S. D. Schubert, 2006: Tropical Intraseasonal Variability in 14 IPCC AR4 Climate Models. Part I: Convective Signals. *J. Climate*, **19**, 2665–2690.

Lin, J.-L., B. Mapes, M. Zhang, and M. Newman, 2004: Stratiform Precipitation, Vertical Heating Profiles, and the Madden–Julian Oscillation. *J. Atmos. Sci.*, **61** (**3**), 296–309.

Lin, J.-L., M. Zhang, and B. Mapes, 2005: Zonal Momentum Budget of the Madden-Julian Oscillation: The Source and Strength of Equivalent Linear Damping. *J. Atmos. Sci.*, **62**, 2172–2188.

Lindzen, R. S. and A. Y. Hou, 1988: Hadley Circulations for Zonally Averaged Heating Centered off the Equator. *J. Atmos. Sci.*, **45** (**17**), 2416–2427.

Lisiecki, L. E. and M. E. Raymo, 2005: A Pliocene-Pleistocene stack of 57 globally distributed benthic δ^{18}O records. *Paleoceanography*, **20**.

Liu, P., T. Li, B. Wang, M. Zhang, J.-j. Luo, Y. Masumoto, X. Wang, and E. Roeckner, 2012: MJO change with A1B global warming estimated by the 40-km ECHAM5. *Clim. Dyn.*

Lorenz, E. N., 1968: Climatic Determinism. *Meteor. Mono.*, **8** (**30**), 1–3.

Lorenzo, D. I. and E. T. Al, 2005: The Warming of the California Current System : Dynamics and Ecosystem Implications. *Current*, 336–362.

Lunt, D. J., A. M. Haywood, G. L. Foster, and E. J. Stone, 2009: The Arctic cryosphere in the Mid-Pliocene and the future. *Phil. Trans. R. Soc. A*, **367**, 49–67.

Madden, R. A. and P. R. Julian, 1971: Detection of a 40-50 day oscillation in the zonal wind in the tropical Pacific. *J. Atmos. Sci.*, **28**, 702–708.

Majda, A. J. and J. A. Biello, 2004: A multiscale model for tropical intraseasonal oscillations. *Proc. Natl. Acad. Sci. USA*, **101** (**14**), 4736–4741.

Majda, A. J. and S. N. Stechmann, 2009: The skeleton of tropical intraseasonal oscillations. *Proc. Natl. Acad. Sci. USA*, **106** (**21**), 8417–8422.

Maloney, E. D., 2002: An Intraseasonal Oscillation Composite Life Cycle in the NCAR CCM3.6 with Modified Convection. *J. Climate*, **15**, 964–982.

Maloney, E. D., 2009: The Moist Static Energy Budget of a Composite Tropical Intraseasonal Oscillation in a Climate Model. *J. Climate*, **22** (**3**), 711–729.

Maloney, E. D. and D. L. Hartmann, 2000: Modulation of Eastern North Pacific Hurricanes by the Madden–Julian Oscillation. *J. Climate*, **13**, 1451–1460.

Maloney, E. D. and A. H. Sobel, 2004: Surface Fluxes and Ocean Coupling the Tropical Intraseasonal Oscillation. *J. Climate*, **17**, 4368–4386.

Maloney, E. D., A. H. Sobel, and W. M. Hannah, 2010: Intraseasonal Variability in an Aquaplanet General Circulation Model. *J. Adv. Model. Earth Syst.*, **2** (**5**), 1–24.

Maloney, E. D. and S.-P. Xie, 2013: Sensitivity of tropical intraseasonal variability to the pattern of climate warming. *J. Adv. Model. Earth Syst.*, **5**, 1–16.

Mapes, B., 2000: Convective inhibition, subgridscale triggering, and stratiform instability in a toy tropical wave model. *J. Atmos. Sci.*, **57**, 1515–1535.

Marlow, J. R., C. B. Lange, G. Wefer, and A. Rosell-Mele, 2000: Upwelling Intensification as Part of the Pliocene-Pleistocene Climate Transition. *Science*, **290**, 2288–2291.

Matsuno, T., 1966: Quasi-Geostrophic Motions in the Equatorial Area. *Journal of the Meteorological Society of Japan*, **44** (**1**), 25–42.

Matthews, A. J., B. J. Hoskins, and M. Masutani, 2004: The Global Response to Tropical Heating in the Madden-Julian Oscillation during Northern Winter. *Q. J. R. Meteorol. Soc.*, **130**, 1–20.

McPhaden, M. J., 1999: Genesis and Evolution of the 1997-98 El Niño. *Science*, **382**, 950–954.

Meehl, G., et al., 2007: *Global Climate Projections. In: Climate Change 2007: The Physical Science Basis. Contribution of Working Group I to the Fourth Assessment Report of the Intergovernmental Panel on Climate Change [Solomon, S., D. Qin, M. Manning, Z. Chen, M. Marquis, K.B. Averyt, M. Tignor and H.L. Miller (eds.)].* Cambridge University Press, Cambridge, United Kingdom and New York, NY, USA.

Mitchell, J. L. and G. K. Vallis, 2010: The Transition to Superrotation in Terrestrial Atmospheres. *J. Geophys. Res.*, **115**, 1–18.

Moncrieff, M. W., 2004: Analytic Representation of the Large-Scale Organization of Tropical Convection. *J. Atmos. Sci.*, **61**, 1521–1538.

Muller, C., P. O'Gorman, and L. Back, 2011: Intensification of Precipitation Extremes with Warming in a Cloud Resolving Model. *J. Climate*, **24**.

Narayan, N., A. Paul, S. Mulitza, and M. Schulz, 2010: Trends in coastal upwelling intensity during the late 20th century. *Environmental Sciences*.

Neale, R. B. and CoAuthors, 2010: Description of the NCAR Community Atmosphere Model (CAM5.0). Tech. rep., 268pp pp.

Neale, R. B., J. H. Richter, and M. Jochum, 2008: The Impact of Convection on ENSO: From a Delayed Oscillator to a Series of Events. *J. Climate*, **21**, 5904–5924.

Neelin, D. J. and I. M. Held, 1987: Modeling Tropical Convergence Based on the Moist Static Energy Budget. *Mon. Weath. Rev.*, **115**.

Numaguti, A. and Y.-Y. Hayashi, 1991: Behavior of Cumulus Activity and the Structures of Circulations in an Aqua Planet Model, Part II: Eastward-Moving Planetary Scale Structure and the Intertropical Convergence Zone. *J. Met. Soc. Japan*, **69** (**5**), 563–579.

Oliver, E. C. and K. R. Thompson, 2012: A reconstruction of Madden-Julian Oscillation Variability from 1905 to 2008. *J. Climate*, **25**, 1996–2019.

Pagani, M., Z. Liu, J. LaRiviere, and A. C. Ravelo, 2010: High Earth-system climate sensitivity determined from Pliocene carbon dioxide concentrations. *Nature Geoscience*, **3** (**1**), 27–30, doi: 10.1038/ngeo724, URL http://www.nature.com/doifinder/10.1038/ngeo724.

Pagani, M., J. C. Zachos, K. H. Freeman, B. Tipple, and S. Bohaty, 2005: Marked Decline in Atmospheric Carbon Dioxide Concentrations During the Paleogene. *Science*, **309** (**5734**), 600–603.

Pai, D. S., J. Bhate, O. P. Sreejith, and H. R. Hatwar, 2011: Impact of MJO on the intraseasonal variation of summer monsoon rainfall over India. *Clim. Dyn.*, **36**, 41–55.

Panetta, R. L., I. Held, and R. Pierrehumbert, 1987: External Rossby Waves in the Two-Layer Model. *J. Atmos. Sci.*, **44** (**20**), 2924–2933.

Pauly, D. and V. Christensen, 1995: Primary production required to sustain global fisheries. *Nature*, **374** (**March**), 255–257.

Pearson, P. N. and M. R. Palmer, 2000: Atmospheric carbon dioxide concentrations over the past 60 million years. *Nature*, **406**, 695–699.

Pearson, P. N., B. E. van Dongen, C. J. Nicholas, and R. D. Pancost, 2007: Stable warm tropical climate through the Eocene Epoch. *Geology*, **35** (**3**), 211–214.

Phlips, P. and A. Gill, 1987: An analytic model of the heat-induced tropical circulation in the presence of a mean wind. *Quart. J. Roy. Meteor. Soc*, **113** (**475**), 213–236.

Pickett, M. H., 2003: Ekman transport and pumping in the California Current based on the U.S. Navy's high-resolution atmospheric model (COAMPS). *J. Geophys. Res.*, **108** (**C10**), 1–10, doi: 10.1029/2003JC001902, URL http://www.agu.org/pubs/crossref/2003/2003JC001902.shtml.

Pierrehumbert, R., 2000: Climate change and the tropical Pacific: The sleeping dragon wakes. *Proc. Natl. Acad. Sci. U.S.A.*, **97** (**4**), 1355–1358.

Pollard, D. and R. M. DeConto, 2009: Modelling West Antarctic ice sheet growth and collapse through the past five million years. *Nature*, **458** (**7236**), 329–32, doi: 10.1038/nature07809, URL http://www.ncbi.nlm.nih.gov/pubmed/19295608.

Pritchard, M. and C. Bretherton, 2013: Causal evidence that rotational moisture advection is critical to the superparameterized Madden-Julian Oscillation. *J. Atmos. Sci.*, **in press.**, doi: 10.1175/JAS-D-13-0119.1.

Pritchard, M. and R. Somerville, 2009: Assessing the diurnal cycle of precipitation in a multi-scale climate model. *J. Adv. Mod. Earth Sys.*, **1** (16).

Randall, D., M. Khairoutdinov, A. Arakawa, and W. Grabowski, 2003: Breaking the Cloud Parameterization Deadlock. *Bull. Amer. Meteor. Soc.*, 1547–1564.

Randel, W. J. and I. M. Held, 1991: Phase Speed Spectra of Transient Eddy Fluxes and Critical Layer Absorption. *J. Atmos. Sci.*, **48** (5), 688–698.

Ravelo, A. C., P. S. Dekens, and M. McCarthy, 2006: Evidence for El Nino-like conditions during the Pliocene. *GSA Today*, **16** (3), 4–11.

Raymo, M., B. Grant, M. Horowitz, and G. Rau, 1996: Mid-Pliocene warmth: stronger greenhouse and stronger conveyor. *Marine Micropaleontology*, **27**, 313–326.

Raymond, D. J., 2001: A New Model of the Madden-Julian Oscillation. *J. Atmos. Sci.*, **58**, 2807–2819.

Raymond, D. J. and v. Fuchs, 2009: Moisture Modes and the Madden-Julian Oscillation. *J. Climate*, **22** (11), 3031–3046.

Raymond, David J. and Sessions, Sharon L. and Sobel, Adam H. and Fuchs, Zeljka, 2009: The Mechanics of Gross Moist Stability. *J. Adv. Model. Earth Syst.*, **1**.

Rayner, N., D. Parker, E. Horton, C. Folland, L. Alexander, D. Rowell, E. Kent, and A. Kaplan, 2003: Global analyses of sea surface temperature, sea ice, and night marine air temperature since the late nineteenth century. *J. Geophys. Res.*, **108** (D14).

Reynolds, R., N. Rayner, T. Smith, D. Stokes, and W. Wang, 2002: An Improved In Situ and Satellite SST Analysis for Climate. *J. Climate*, **14**, 1609–1625.

Roundy, P. E., 2012: Observed Structure of Convectively Coupled Waves as a Function of Equivalent Depth: Kelvin Waves and the Madden Julian Oscillation. *J. Atmos. Sci.*

Roundy, P. E. and W. M. Frank, 2004: A Climatology of Waves in the Equatorial Region. *J. Atmos. Sci.*, **61** (17), 2105–2132.

Salby, M. L. and R. R. Garcia, 1987: Transient Response to Localized Episodic Heating in the Tropics. Part I: Excitation and Short-Time Near-Field Behavior. *J. Atmos. Sci.*, **44** (2), 458–498.

Salzmann, U., A. Haywood, and D. Lunt, 2009: The past is a guide to the future? Comparing Middle Pliocene vegetation with predicted biome distributions for the twenty-first century. *Phil. Trans. R. Soc. A*, **367**, 189–204.

Saravanan, R., 1993: Equatorial superrotation and maintenance of the general circulation in two-level models. *J. Atmos. Sci*, **50**, 1211–1227.

Sardeshmukh, P. D. and B. J. Hoskins, 1988: The Generation of Global Rotational Flow by Steady Idealized Tropical Divergence. *J. Atmos. Sci*, **45** (**7**), 1228–1251.

Scherer, R. P., 1991: Quaternary and Tertiary microfossils from beneath Ice Stream B: Evidence for a dynamic West Antarctic Ice Sheet history. *Paleogeography, Paleoclimatology, Paleoecology*, **90**, 395–412.

Schumacher, C., R. Houze Jr., and I. Kraucunas, 2004: The tropical dynamical response to latent heating estimates derived from the TRMM precipitation radar. *J. Atmos. Sci.*, **61**, 1341–1358.

Seki, O., G. L. Foster, D. N. Schmidt, A. Mackensen, K. Kawamura, and R. D. Pancost, 2010: Alkenone and boron-based Pliocene pCO2 records. *Earth and Planetary Science Letters*, **292** (**1-2**), 201–211, doi: 10.1016/j.epsl.2010.01.037, URL http://linkinghub.elsevier.com/retrieve/pii/S0012821X10000816.

Seo, K.-H. and S.-W. Son, 2012: The Global Atmospheric Circulation Response to Tropical Diabatic Heating Associated with the Madden-Julian Oscillation during Northern Winter. *J. Atmos. Sci.*, **69**, 79–96.

Shell, K. M. and I. M. Held, 2004: Abrupt Transition to Strong Superrotation in an Axisymmetric Model of the Upper Troposphere. *J. Atmos. Sci.*, **61**, 2928–2936.

Showman, A. P. and L. M. Polvani, 2010: The Matsuno-Gill Model and Equatorial Superrotation. *Geophys. Res. Lett.*, **37**, 1–17.

Slingo, J. M., D. P. Rowell, K. R. Sperber, and F. Nortley, 1999: On the predictability of the interannual behaviour of the Madden-Julian Oscillation and its relationship with El Niño. *Q. J. R. Meteorol. Soc.*, **125**, 583–609.

Sobel, A. and E. Maloney, 2012: An Idealized Semi-Empirical Framework for Modeling the Madden-Julian Oscillation. *J. Atmos. Sci.*, **69**, 1691–1705.

Sobel, A. H., E. D. Maloney, G. Bellon, and D. M. Frierson, 2008a: Surface Fluxes and Tropical Intraseasonal Variability a Reassessment. *J. Adv. Model. Earth Syst.*, **2**.

Sobel, A. H., E. D. Maloney, G. Bellon, and D. M. Frierson, 2008b: The role of surface heat fluxes in tropical intraseasonal oscillations. *Nature Geoscience*, **1**, 653–657.

Sobel, A. H., J. Nilsson, and L. Polvani, 2001: The weak temperature gradient approximation and balanced tropical moisture waves. *J. Atmos. Sci.*, **58**, 3650–3665.

Stevens, B. and S. Bony, 2013: What Are Climate Models Missing? *Science*, **340**, 1053–1054.

Suarez, M. J. and D. G. Duffy, 1992: Terrestrial Superrotation: A Bifurcation of the General Circulation. *J. Atmos. Sci.*, **49** (**16**), 1541–1554.

Swinbank, R., T. Palmer, and M. Davey, 1988: Numerical Simulations of the Madden and Julian Oscillation. *J. Atmos. Sci.*, **45** (**5**).

Takahashi, C., N. Sato, A. Seiki, K. Yoneyama, and R. Shirooka, 2011: Projected Future Change of MJO and its Extratropical Teleconnection in East Asia during the Northern Winter Simulated in IPCC AR4 Models. *SOLA*, **7**, 201–204.

Thayer-Calder, K. and D. A. Randall, 2009: The Role of Convective Moistening in the Madden–Julian Oscillation. *J. Atmos. Sci.*, **66** (**11**), 3297–3312.

Tziperman, E. and B. Farrell, 2009: Pliocene equatorial temperature: Lessons from atmospheric superrotation. *Paleoceanography*, **24** (**1**), 1–6.

Wara, M. W., A. C. Ravelo, and M. L. Delaney, 2005: Permanent El Nino-Like Conditions During the Pliocene Warm Period. *Science*, **309**, 758–761.

Wheeler, M. and G. N. Kiladis, 1999: Convectively Coupled Equatorial Waves: Analysis of Clouds and Temperature in the Wavenumber–Frequency Domain. *J. Atmos. Sci.*, **56** (**3**), 374–399.

Wheeler, M. C. and H. H. Hendon, 2004: An All-Season Real-Time Multivariate MJO Index: Development of an Index for Monitoring and Prediction. *Mon. Wea. Rev.*, **132**, 1917–1932.

Willeit, M., A. Ganopolski, and G. Feulner, 2013: On the eÔ¨Äect of orbital forcing on mid-Pliocene climate, vegetation and ice sheets. *Clim. Past Discuss.*, **9**, 1703–1734.

Williams, G. P., 2003: Barotropic Instability and Equatorial Superrotation. *J. Atmos. Sci.*, **60**, 2136–2152.

Williams, G. P., 2006: Equatorial Superrotation and Barotropic Instability: Static Stability Variants. *J. Atmos. Sci.*, **63**, 1548–1557.

Winant, C. D. and C. E. Dorman, 1997: Seasonal patterns of surface wind stress and heat flux over the Southern California Bight. *J. Geophys. Res.*, **102** (**C3**), 5641–5653.

Wu, C.-H. and H.-H. Hsu, 2009: Topographic Influence on the MJO in the Maritime Continent. *J. Climate*, **22**, 5433–5448.

Yamaguchi, K. and A. Noda, 2006: Global Warming Patterns over the North Pacific: ENSO vs AO. *J. Met. Soc. Japan*, **84** (**1**), 221–241.

Yu, J.-Y., C. Chou, and J. D. Neelin, 1998: Estimating the Gross Moist Stability of the Tropical Atmosphere. *J. Atmos. Sci.*, **55**, 1354–1372.

Zhang, C., 2005: Madden-Julian Oscillation. *Rev. Geophys.*, **41** (**2004**), 1–36.

Zhang, C. and M. Dong, 2004: Seasonality in the Madden-Julian Oscillation. *J. Climate*, **17**, 3169–3180.

Zhang, C., M. Dong, S. Gualdi, H. H. Hendon, E. D. Maloney, A. Marshall, K. R. Sperber, and W. Wang, 2006: Simulations of the Madden–Julian oscillation in four pairs of coupled and uncoupled global models. *Clim. Dyn.*, **27**, 573–592.